Relative Impact of Surface and Aerosol Heterogeneities on Deep Convection

Zur Erlangung des akademischen Grades eines
DOKTORS DER NATURWISSENSCHAFTEN
von der Fakultät für Physik des
Karlsruher Instituts für Technologie (KIT)

genehmigte

DISSERTATION

von

M.Sc. Linda Schneider
aus Köln

Tag der mündlichen Prüfung: 7. Dezember 2018

Referent: Prof. Dr. Corinna Hoose

Korreferent: Prof. Dr. Christoph Kottmeier

Abstract

The evolution of deep moist convection and subsequent precipitation is strongly linked to the heterogeneity of the underlying surface. Orography has a strong influence on the wind field by blocking, flow deviation and/or lifting of air masses but also thermally induced secondary circulations are important for convection. The soil moisture content, on the other hand, primarily influences the surface energy budget and leads to a partitioning of the available energy into sensible and latent heat. Aerosols affect convective precipitation as they change microphysical pathways and modify thermodynamics. All three contributors have dynamic and thermal compounds, which interplay with each other and make it difficult to properly represent precipitation in numerical weather models due to insufficient understanding and description of physical processes. It is very challenging to deduce the relative effects of these contributors, as their importance may vary depending on the large-scale situation, the region studied and the environmental conditions.

Within this study the effect of terrain structure, soil moisture, and aerosols on deep moist convection over Germany is investigated. This study is unique as it is the first one to investigate the contributions of surface and aerosol heterogeneities for the same days. Numerical simulations are performed with the COSMO model at high spatial resolution (horizontal grid length of 500 m). Undisturbed simulations serve as reference and then the three convection-influencing parameters are varied by introducing realistic and idealized patterns in the following ways: (i) the terrain is incrementally smoothed and flattened, (ii) the magnitude of the soil moisture field is changed and soil moisture is redistributed into chess board and random structures using two discrete values and (iii) four different homogeneous aerosol concentrations are used and chess board patterns with spatially variable concentrations are implemented. All sensitivity runs are conducted for three days with weak and strong forcing conditions, respectively. The results of this study help to gain a deeper process understanding. Furthermore, they also allow to derive the suitability of different perturbations for numerical weather prediction ensembles, which provide a valuable tool for quantitative precipitation forecast.

The numerical results show that the role of individual mountains is complex and its effect on precipitation varies. Despite different feedback signs, all simulations with altered terrain show that the low-level wind convergence strongly influences the initiation of deep convection. Simulations with flattened mountain ranges show a local effect on precipitation in two aspects. First, the timing of precipitation is delayed by two hours due to weaker triggering. Second, the precipitation amount over the modified regions varies between -21 and up to +7% compared to the unperturbed reference simulation, as the missing triggering effect in the absence of mountains is compensated on one day by an increase in the

low-level wind convergence due to thermal heating, cold-pool outflow or boundary layer rolls. Averaged over the full domain, the simulations with locally flattened orography only lead to a precipitation change of -11 to +8% compared to the reference simulation. When smoothing the terrain height throughout the whole domain, the effect of individual valleys on the daily accumulated precipitation is between +/-2% on five days and in the order of artificially created noise by temperature perturbations. Nevertheless, the low-level wind convergence systematically decreases with smoother surface parameters on all days. Simulations with increased/decreased soil moisture content by 25% show both a positive and a negative soil moisture–precipitation (SMP) feedback, depending on the initial soil moisture content. In regimes where evapotranspiration is limited by the available soil moisture, the SMP feedback is positive (-15 to +17%), while saturated regimes lead to a smaller (-5 to +6%) and negative SMP feedback. Simulations with artificially introduced soil- moisture fields (e. g. chess boards and random structures) show a more systematic dependency, as differential heating leads to secondary circulations and affects precipitation amounts and vertical cloud structures locally. Converging motions can be found over the dry and diverging motions over the wet patch, resulting in clouds with higher cloud base but more condensate over the dry patch and subsequently more precipitation. Different aerosol assumptions lead to an almost systematic response within each day, but can show opposite behaviors on other days. Varying from clean to polluted conditions, three days with weak convection show a decrease in precipitation up to -11% compared to the reference. Here, the suppression of warm rain reduces precipitation with increasing cloud condensation nuclei concentrations. On the other three days, high instability and stronger updrafts lead to increased importance of mixed-phase processes, which result in up to 3% higher precipitation amounts with increasing cloud condensation nuclei. The runs with heterogeneous aerosol assumptions show similar trends locally, however the change in precipitation within the whole domain is, for four days, below 1.1% and thus relatively small.

The findings from this study demonstrate the complexity of multiple processes on different spatial scales for the initiation of deep convection due to surface inhomogeneities. While the timing is, if at all, only affected locally in the runs with altered orography, the precipitation amounts vary. In general, soil moisture, and especially those runs with increased or decreased soil moisture, shows the largest spread in precipitation. This is of special interest and importance, as these simulations are among the most realistic ones in this study. Soil moisture perturbations should therefore be part of an ensemble used for numerical weather prediction. Aerosols affect the precipitation efficiency and the distribution in precipitation mostly under strong synoptic conditions, whereas weak forcing days show a higher impact by orography than by aerosol perturbations. The location of precipitation is determined by the presence of low-level wind convergence zones, which result from the terrain itself or because of thermal gradients that induce near-surface winds. Therefore, the orography simulations and the soil moisture simulations show a higher effect on the spatial distribution of precipitation than the aerosol simulations.

Contents

1. Motivation

Have you checked the weather forecast today?
Precipitation forecast is a critical component of our lives: For an individual person leaving the house up to institutions taking actions in case of extreme precipitation events. Especially over mountainous regions, a reliable precipitation forecast is particularly important (Behrendt et al., 2011). In these regions, the location of precipitation determines in which river catchment the water flows, entailing the risk of flash flood even for regions further away (Spreafico, 2006). In addition, mountains are a hot-spot for summer thunderstorms (Piper and Kunz, 2017), which is often accompanied by large precipitation amounts, thereby enhancing the risk of extreme weather events. These events can then affect a wide range of sectors, like agriculture, traffic, energy or tourism, causing socio- and economical losses (Jahn, 2015). Therefore, it is desired to accurately predict location, amount and timing of precipitation.

Precipitation is a frequently occurring phenomenon and people have studied it for many years. Still, the accurate prediction of precipitation is a challenge for today's numerical weather forecast (e. g. Kühnlein et al., 2014; Carbone et al., 2002; Fritsch and Carbone, 2004; Schwitalla et al., 2008). One reason is that precipitation is a result of a complex chain of physical processes. Starting with energy exchange processes at the surface, which induce vertical motion of air, followed by condensation, formation of precipitation through microphysical processes, the sedimentation and possible transport of precipitating particles downstream by horizontal advection. Within this line there are different processes that remain poorly understood.

In this study, three aspects of this chain are investigated to gain a deeper process understanding: The effect of orography and soil moisture on convection triggering and/or enhancement of precipitation as well as the contribution of cloud condensation nuclei to microphysical processes in clouds. The aim is to gain a better understanding as to which of these three aspects is most relevant under various meteorological conditions, and how they influence location, amount and timing of precipitation. This will be answered with a special focus on mountainous regions. Chapter 2 summarizes the current findings regarding challenges that come with forecasting precipitation and the uncertainties in orography, soil moisture and microphysics, along with the research questions. The model setup is presented in Chapter 3. Results are given individually for all three aspects in Chapter 4. The findings of this study will be summarized in Chapter 5 and will help to recommend where future model development can start to address current weaknesses and uncertainties in precipitation forecasting.

2. Current Understanding

Despite improvements in numerical weather prediction models in the last decade, quantitative precipitation forecasting remains a challenge (Clark et al., 2016). The forecast of deep moist convection, which will be referred to to as deep convection, is often not adequate for many applications (e. g. Kühnlein et al., 2014; Mittermaier, 2014). Difficulties in the prediction are due to an insufficient understanding of physical processes, inadequate representation of physical processes, numerical uncertainties and uncertainties in the initial and boundary conditions. One challenge that the forecasting brings with it is the distinct spatial and temporal variability of precipitation. Several studies have examined the poor forecast of convection both in space and time (e. g. Carbone et al., 2002; Fritsch and Carbone, 2004; Schwitalla et al., 2008). According to Keil and Craig (2011), the forecast uncertainty of convective precipitation is influenced by all scales, however its prediction is linked to the synoptic conditions (Wapler et al., 2015). In situations when precipitation is driven by the synoptic scale (strong forcing, e. g. frontal zones), the prediction of precipitation is often reliable (Baldauf et al., 2011). In cases when convection is governed by local processes (weak forcing), mesoscale surface heterogeneities, e.g. soil moisture gradients, land use change or variations in terrain height and the development of convergence zones within the planetary boundary layer often control the initiation of deep convection (e. g. Bennett et al., 2006; Groenemeijer et al., 2009; Barthlott et al., 2011b, 2016). Because of their small-scale characteristics, those features are usually less well represented and make precipitation forecasting challenging (e. g. Zhang et al., 2006; Trentmann et al., 2009). Not only that different characteristics influence the initiation of convection, the susceptibility of convection to different synoptic conditions makes it even more difficult to accurately predict precipitation, as the individual mechanisms leading to convection initiation may vary significantly.

2.1. General background: adiabatic parcel theory

One of the prerequisites for deep convection is atmospheric instability. Atmospheric instability describes a state in which a hypothetical parcel of air accelerates away from its initial position when displaced vertically. Instead of using densities, usually temperatures are used to deduce the stability, as density and temperature are inversely proportional. The temperature of an adiabatically lifted parcel (T_p) is compared to the temperature of the undisturbed environment (T_e) at the same pressure (e. g. Saucier, 1955). The lapse rate of the parcel between two layers is defined by $\Gamma = -\delta T_p/\delta z$, and the lapse rate of the environment as $\gamma = -\delta T_e/\delta z$. The state when $\Gamma < \gamma$ is called statically unstable, because lifted air parcels

become positively buoyant and accelerate upward. $\Gamma > \gamma$ describes the statically stable state, in which lifted air parcels become negatively buoyant and hence accelerate downward and $\Gamma = \gamma$ is called statically neutral, when no vertical displacement takes place. When unsaturated parcels are displaced upwards, they cool with the dry adiabatic lapse rate $\Gamma_d \approx g/c_p$, with the gravity constant g ($\Gamma_d \approx 9.8\,\mathrm{K\,km^{-1}}$) and the specific heat of dry air at constant pressure c_p. In saturated parcels, on the other hand, condensation takes place and latent heat is released. Therefore, the moist adiabatic lapse rate Γ_s is smaller than the dry adiabatic lapse rate. Differentiating between moist and dry parcels, the following stability states can be defined in particle sense (Bryan and Fritsch, 2000): (a) $\gamma < \Gamma_s$: absolutely stable, (b) $\gamma_s = \Gamma_s$ saturated neutral, (c) $\Gamma_s < \gamma < \Gamma_d$: conditionally unstable, (d) $\gamma_s > \Gamma_s$: saturated absolutely unstable, (e) $\gamma = \Gamma_d$: dry neutral, (f) $\gamma > \Gamma_d$: dry absolutely unstable. γ and γ_s are the lapse rates of the unsaturated and saturated environment, respectively.

For the purpose of deep moist convection one of the cases (c), (d) or (f) is needed. In the case of absolutely unstable conditions, an air parcel would ascent freely. When conditions are conditionally unstable, sufficient moisture and/or a trigger mechanism are also needed to reach instability. To understand the requirements for conditional instability, the analysis of temperature profiles in a skewT-log p diagram can be used. According to Figure 2.1, a parcel lifted from the ground ascends dry adiabatically with the lapse rate of Γ_d up to the lifting condensation level (LCL). From here onwards, the parcel is lifted moist adiabatically and will become warmer than the surrounding air. This occurs at the level of free convection (LFC) from where onward positive buoyancy leads to rising of the parcel up until the equilibrium level (EL). The convective available potential energy (CAPE) is the integrated positive buoyancy (B, derived from the virtual potential temperature T_v from the parcel and environment) between the LFC and the EL:

$$CAPE = g\int_{LFC}^{EL} B dz = g\int_{LFC}^{EL} \frac{T_{v,parcel} - T_{v,env}}{T_{v,env}} dz \qquad [2.1]$$

The energy to get the parcel from an altitude z to the LFC, thus the amount of negative buoyancy is called convective inhibition (CIN).

$$CIN = g\int_{z}^{LFC} B dz = g\int_{z}^{LFC} \frac{T_{v,parcel} - T_{v,env}}{T_{v,env}} dz \qquad [2.2]$$

Thus the conclusion is that deep moist convection requires to overcome CIN and sufficient CAPE for further lifting. Trigger mechanisms, like orography or circulations induced by soil moisture gradients can thus help to overcome CIN and their individual impacts will be discussed in the following sections.

2.2. Uncertainties in physical processes: orography

Mountains can trigger deep convection by modifying the wind flow in two dominant ways: mechanically and thermally. The flow experiences mechanical forcing by ascending or moving around a mountain. The non-dimensionless Froude number, $Fr = U/(Nh_m)$ where U is the cross-barrier wind speed, N the Brunt-Väisälä frequency, and h_m the mountain height is a measure of which pathway is most likely. For

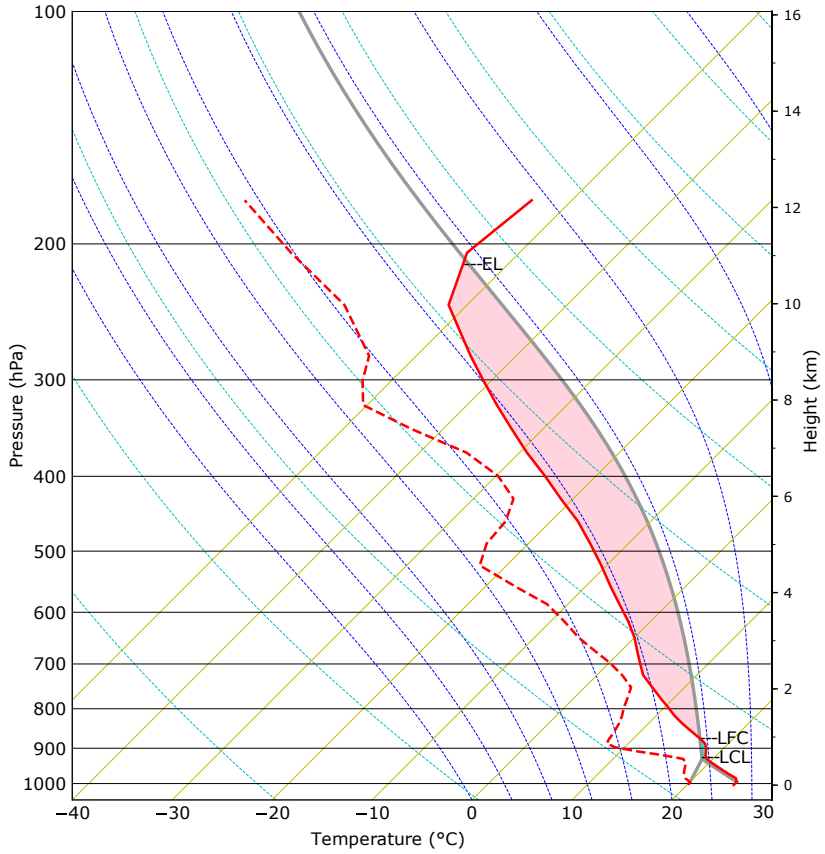

Fig. 2.1.: Skew-T/log-p diagram showing a conditionally unstable situation, with the temperature (red), dew point temperature (red dashed), moist (dark blue) and dry (light blue) adiabats and dew point temperatures for different isotherms (yellow). The grey line is the path of an adiabatically lifted surface-based parcel. LCL is the lifting condensation level, LFC is the level of free convection, and EL the equilibrium level.

$Fr \gg 1$, the flow ascends over the obstacle, whereas for $Fr \ll 1$, the flow will detour around it. In case of thermal forcing, differential heating will occur at the elevated surfaces inducing thermal gradients. Recently, Kirshbaum et al. (2018) have reviewed the most dominant pathways of which the direct orographic ascent is the simplest and most frequent mechanism. Convection is initiated at the point where the flow reaches the LFC and precipitation falls at the windward side or at the mountain crest (Figure 2.2(a)). By blocking at the mountain crest, and hence horizontal deceleration, convection can be initiated at the foot of the mountain (Figure 2.2(b)). In case that the flow splits and flows around the mountain, convergence zones can establish at the downwind side behind the barrier (Figure 2.2(c)). During daytime, when temperatures are warmer in the valleys than on the mountains, upslope flows can lead to the formation of convergence zones on top of the mountain (Figure 2.2(d)). This mechanism is very prominent in initiating severe summer thunderstorms (Weckwerth et al., 2011). During nighttime, the situation is reversed and katabatic downslope winds can establish. When these winds merge with the ambient flow, convergence zones can form at the foothills (Figure 2.2(e)). When thermally driven upslope winds interact with the overlying unblocked flow (i.e. gravity waves), cloud formation may be provoked

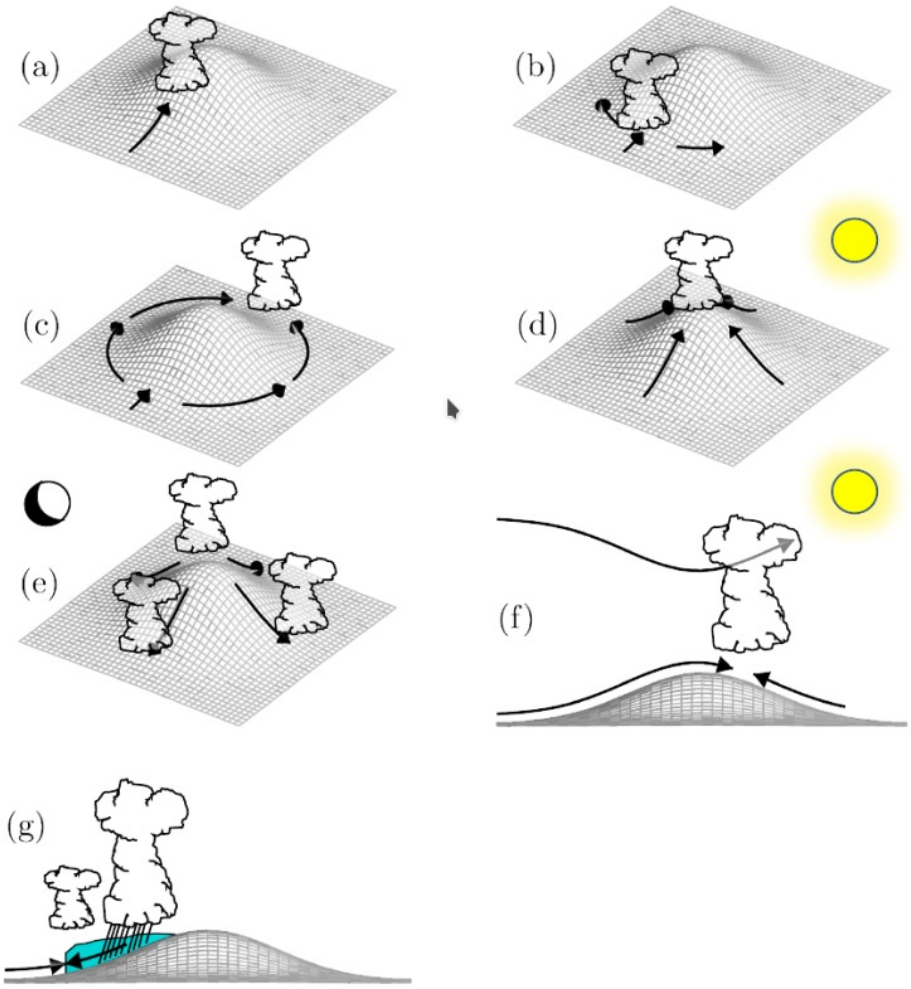

Fig. 2.2.: Conceptual pathways of convection initiation over a mountain: (a) direct orographic ascent, (b) upstream blocking, (c) downstream convergence, (d) thermally forced upslope flow, (e) katabatic flow, (f) gravity waves and thermally induced upslope flow, (g) cold pool outflow. This figure is taken from Kirshbaum et al. (2018) and originally published under the Creative Common Licence CC BY 4.0 (http://creativecommons.org/licenses/by/4.0/)

in the region of alignment (Figure 2.2(f)), potentially enhancing the strength of convection. Whereas all of these mechanisms are direct feedbacks from the terrain, there might also be indirect effects. Once precipitation starts, evaporative cooling may induce subcloud cold pools. Their outflow can then lead to the formation of convergence zones, triggering new convection. Of course, orographic convection is highly complex and the described mechanisms often interact, depending on the geometry of the mountain (ranges) and the large-scale synoptic forcing. Therefore, there is no generalization as on how orography influences precipitation in a particular event, making it challenging to predict precipitation.

Several studies have shown that severe weather events often result from the interplay between the large-scale forcing and orographic lifting of air. Rotunno and Ferretti (2001) showed that orographically

modified flow was decisive for huge amounts of rainfall. In a model study, they simulated the 1994 Piedmont flood with idealized and modified (height and form) orography. Next to complex orographic responses for different flow regimes, they found that maximum rain rates are linked to maximum vertical wind velocities induced by orographic uplift. Similarly, Buzzi et al. (1998) deduced from a model study that for a flood event in the Alps, the presence of orography enhances precipitation because of more vigorous updrafts and a modification of the pressure field. Langhans et al. (2011) also simulated a flood event in the Alpine region and found that orography influences the intensity of precipitation, but that the initiation is linked to the establishment of synoptically triggered convergence zones. Schumacher et al. (2015) investigated the formation of snow bands over the Rocky Mountains and found the synoptic forcing being decisive for the formation of a major precipitation band. Minor bands formed in regions where the terrain was smoothed because of atmospheric instability. However, the presence of mountains was again necessary for the development of these small bands. Kirshbaum et al. (2007) found that lee waves act as trigger mechanisms for simulated rain bands in the US. Results from the Mesoscale Alpine Programme show that the prediction of intensity, location, and duration of precipitation requires insight into the orographically modified flow (e. g. Rotunno and Houze, 2007).

During fair weather conditions, thermally induced circulations and low-level convergence zones become more relevant because their presence leads to the formation of cumulus clouds over mountain crests (Raymond and Marvin, 1980). Several studies have looked at the formation of convergence zones by slope and valley winds in the Black Forest region in south-west Germany (e. g. Meißner et al., 2007; Kalthoff et al., 2009) and the subsequent initiation of convection (Kottmeier et al., 2008). Smith et al. (2015) found that orography acts as a trigger mechanism as warm and moist air is lifted. From a model intercomparison, Barthlott et al. (2011a) deduce that the proper representation of boundary-layer convergence lines is critical for the simulation of precipitation. Kühnlein et al. (2014) state for a region spanning the Black Forest and surrounding areas, that the forecast skill for precipitation is higher over complex than over flat terrain. The errors introduced by small-scale disturbances (i.e. a bad representation of the initial temperature field) can propagate upwards in height and impact the geostrophically balanced flow (Selz and Craig, 2015). Consequently, and especially under weak synoptic conditions, detailed knowledge about the convection-initiating mechanisms are essential for precipitation forecasting.

Because of the complex influence that orography has on precipitation, both under weak and strong synoptic conditions, and the need to further understand convection-initiating mechanisms to improve quantitative precipitation forecasting, high-resolution numerical simulations (500-m grid spacing) are performed for several days with different synoptic controls (i. e. weak and strong synoptic forcing). So far, most studies have only investigated single case events (e. g. Bennett et al., 2011; Burton et al., 2013). The area of investigation is south-west Germany and eastern France. Here, the low-mountain ranges of the Black Forest and the Vosges are situated. The effect that the terrain elevation and the resolution of the topographic data set has on the initiation of convection is investigated. The impact that different resolutions of external data have on precipitation is from importance because computer power

has increased in the recent years and models can now operate with finer resolutions (Heinze et al., 2017), which does not necessarily imply that the resolution of external data is likewise adjusted. However, it is still unclear how well terrain features need to be resolved for quantitative precipitation forecasting. In particular the following research questions will be addressed:

1. What is the effect of orography on the initiation of deep convection over the Black Forest and the Vosges?
2. How do these two neighbouring low mountain ranges influence each other?
3. How important is the resolution of the topography, i. e. what effect do individual valleys have in this context?
4. Do the sensitivities depend on the degree of synoptic forcing, e. g. are orographic effects more important when large-scale forcing is weaker?

2.3. Uncertainties in initial conditions: soil moisture

Soil moisture plays a key role in the water and land energy balance. The amount of water in the soil is determined by the amount of precipitation P, the loss by evapotranspiration E and sub- and above ground flow R_d, i.e. drainage and runoff. The surface energy balance includes the long- and shortwave

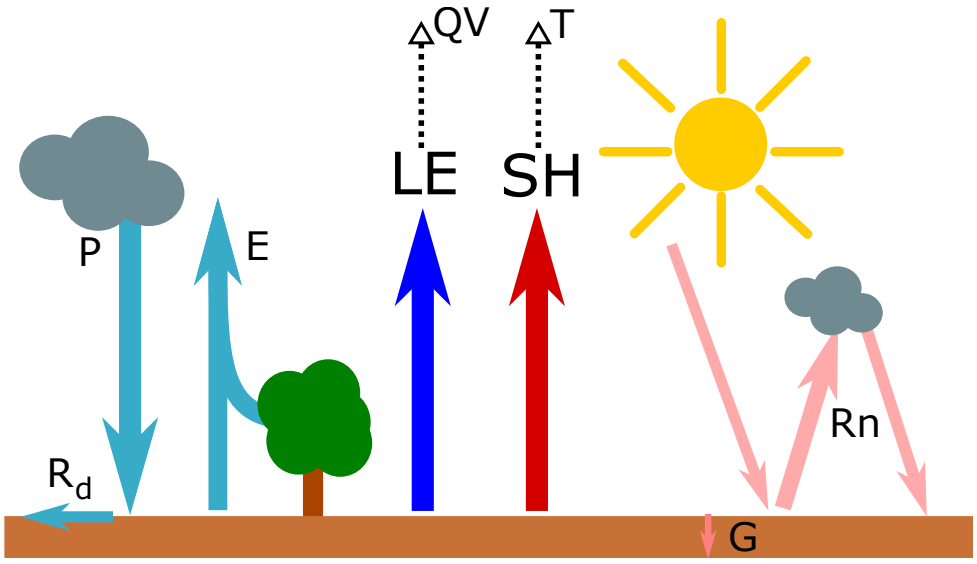

Fig. 2.3.: Schematic view of the water and land energy balance. P is precipitation, E evapotranspiration, R_d sub- and above ground flow, Rn long- and shortwave radiation, G ground heat flux, SH the sensible heat flux associated with a change in temperature T, LE the latent heat flux which impacts the specific humidity QV.

net radiation Rn, the ground heat flux G, as well as the sensible heat flux SH and latent heat flux LE. The latent heat flux describes the heat exchange from the surface to the atmosphere, associated with

evaporation and transpiration. It is the product of the latent heat for vaporization l_v ($2260\,\mathrm{Jkg^{-1}}$) , the density of air ρ, and the kinematic moisture flux $\overline{w'q'}$:

$$LE = \rho l_v \overline{w'q'} \qquad [2.3]$$

The sensible heat flux characterizes heat exchange due to temperature differences between surface and atmosphere, a predominantly convective process. It consists of the specific heat for air c_p ($1004\,\mathrm{Jkg^{-1}K^{-1}}$), the density of air ρ and the kinematic heat flux $\overline{w'\theta'}$:

$$SH = \rho c_p \overline{w'\theta'} \qquad [2.4]$$

In the model, these fluxes are calculated within the surface layer parametrization, using a gradient in q or θ between the surface and the first model level. The ratio between the latent and the sensible heat fluxes is called Bowen ratio β (Seneviratne et al., 2006). With its effect on the surface energy balance, soil moisture influences the development of the atmospheric boundary layer. While latent heat affects the specific humidity (QV) within the boundary layer, an increase in sensible heat leads to warmer temperatures (T) and induces turbulence, which promotes boundary layer growth. With sufficient humidity in the air, this can trigger cloud formation. Conditions where $\beta > 1$ result in a more humid and shallow boundary layer, while $\beta < 1$ leads to a deep and well-mixed boundary layer.

One major uncertainty within these exchange processes is the accuracy of initial conditions. Measuring soil moisture is still a challenge due to its substantial spatial variability, from a few centimeters to hundreds of kilometers, and temporally, from a few minutes to months (Vereecken et al., 2014; Santanello et al., 2018). In recent years, non-local measurement techniques, like remote sensing, have received more attention as they allow for a high spatial and temporal data coverage (Vereecken et al., 2008). Several studies have tried to evaluate non-local measurements against ground-based measurements (e. g. Brocca et al., 2011). Usually, in-situ measurements and remote measurements show a strong relationship for the top layer (Brocca et al., 2011). However, a proper evaluation is challenging due to the uncertainty in accuracy of remote sensing measurements as well as in station-based observations (Dorigo et al., 2015). In terms of precipitation forecasting, models rely on simple assumptions about the initial conditions (Western et al., 2002), which then often produces large forecast errors (Van Weverberg et al., 2010). This can have a considerable impact on the results obtained by model studies (Sheffield et al., 2012). For a region in south-west Germany simulated soil-moisture and observations show strong differences (Krauss et al., 2010), with the mean bias for most of the stations and measurement depths around 20-30% (Hauck et al., 2011), which highlights the need for accurate data assimilation and a corresponding dense network of measurements.

Many numerical studies have investigated the soil-moisture–precipitation (SMP) feedback, i.e. whether drier soils lead to less (positive feedback) or more (negative) precipitation and vice versa for wetter soils. It is found that soil-moisture influences a number of processes concerning land-atmosphere interactions on different spatial and temporal scales with respect to the initiation of convection and the subsequent

possibility of convective precipitation (e. g. Seneviratne et al., 2006; Taylor and Ellis, 2006; Taylor et al., 2007). The sign of the SMP feedback may vary spatially and temporally (e. g. Pan et al., 1996). For the Alpine region, Hohenegger et al. (2009) conducted real-case simulations with resolved and parameterized convection. They found that both the feedback and the strength of the SMP feedback differ. The different feedback signs were found to be related to the presence of a stable layer on top of the planetary boundary layer, because in the case of fully resolved convection, more vigorous thermals established in the simulations with dry bias, leading to a negative SMP feedback. For real case simulations over mountainous regions in south-west Germany and eastern France, Barthlott et al. (2011a) show that changing the initial soil moisture content can lead to various responses. They found that during wet conditions, evapotranspiration is determined by the net radiation, resulting in a non-systematic and weak precipitation response. On the other hand, when the soil is drier, evapotranspiration is governed by the amount of soil moisture leading to a positive feedback.

Additionally, horizontal land-surface wetness gradients strongly influence mesoscale circulation patterns. The main cause is a spatial gradient in the sensible heat flux, which results from variations in surface evaporation, i.e. due to different soil types, solar irradiance reflection/absorption, and thermal energy storage in the soil (Cheng and Cotton, 2004). Using measurement data, Taylor et al. (2007) studied these soil moisture induced circulations over the arid Sahel region and found that low-level convergence (divergence) zones form over dry (wet) soil, leading to enhanced precipitation close to the boundaries of dry and wet regions (Taylor et al., 2011). Kang and Bryan (2011) confirmed similar results in a numerical study. However, results are less consistent in the mid-latitudes (e. g. Findell and Eltahir, 2003; Tuttle and Salvucci, 2016). Froidevaux et al. (2014) propose that inconsistencies between positive and negative feedbacks could be linked back to differences in the background wind. They confirm in an idealized numerical study over flat terrain that with no background wind storms are initiated and precipitation occurs over the dry patches due to the establishment of convergence zones. In contrast, when there is a stronger background wind, the developing cells get advected downstream and precipitate over the wet areas where CAPE is high. Similar results have been reported in an observational study by Guillod et al. (2014). In an idealized study, Rieck et al. (2014) show that over the dry patches, the transition from shallow to deep convection occurs at an earlier time due to more vigorous updrafts. According to Cioni and Hohenegger (2017), an earlier triggering of convection will enhance precipitation duration, while the intensity is determined by the amount of latent heat flux at the surface.

Until now most studies focused on the role of soil moisture over flat terrain, and if over complex terrain than mostly by introducing uniform changes of the background soil moisture. The simultaneous effect of soil moisture and terrain heterogoeneities on boundary layer development (Rihani et al., 2015), adds another level of complexity to convective activity over mountainous regions (Hauck et al., 2011). Just recently, an idealized study was presented by Imamovic et al. (2017) investigating both the individual and the combined effects of soil moisture and orography for weak forcing conditions. Whereas introducing soil moisture biases always yield a positive soil moisture – precipitation response, local disturbances in

soil moisture have different effects depending on the orography: The higher the mountain, the smaller the importance of soil moisture disturbances on precipitation.

In this study, real-case simulations are performed with introduced soil moisture biases and spatial gradients. The aim is to investigate the soil moisture–precipitation feedback both for complex (same region as for the orography study) and flat terrain and consider different synoptic conditions. The following research questions will be addressed:

5. What is the effect of (homogeneous and heterogeneous) soil moisture patterns on the initiation of deep convection?

6. How does the soil-moisture–precipitation feedback behave in simulations with artificially introduced soil-moisture gradients?

7. How do the results change depending on the synoptic conditions (i.e. weak or strong synoptic forcing)?

2.4. Microphysical impacts on clouds

Aerosols are crucial for cloud formation, as they can serve as cloud condensation (CCN) or ice nuclei (IN). In general, clouds form when supersaturation with respect to water or ice is present. In an entirely pristine environment, water vapor would not condense until values of relative humidity up to 400% are reached, a process called homogeneous nucleation. With the presence of aerosols, serving as a surface where water can condense/freeze upon, cloud formation already occurs at relative humidities near 100%, thereby being essential for clouds to form (Fletcher, 1962).

Aerosols in the atmosphere have a variety of shapes and chemical compositions. They can be directly emitted from various sources or be formed in the atmosphere by chemical reaction. They are characterized by the particle diameter, which can range from a few nanometers to around 100 μm (Friedlander, 2000). Whether or not an aerosol gets activated as CCN depends on the mass and composition of the water-soluble component. The Köhler curve (Köhler, 1936) describes the relationship between drop size and equilibrium supersaturation (s_s) at the surface of the drop according to

$$s_s = \frac{A}{d_D} - \frac{B}{d_D^3} \qquad [2.5]$$

with

$$A = \frac{4 M_W \sigma_W}{R T \rho_W} \qquad [2.6]$$

and

$$B = \frac{6 n_{sol} M_W}{\pi \rho_W} \qquad [2.7]$$

where d_D is the diameter of the droplet, M_w the molecular mass of water, σ_W the water surface tension, ρ_w the density of water, R the universal gas constant, T the temperature and n_{sol} the amount of substance

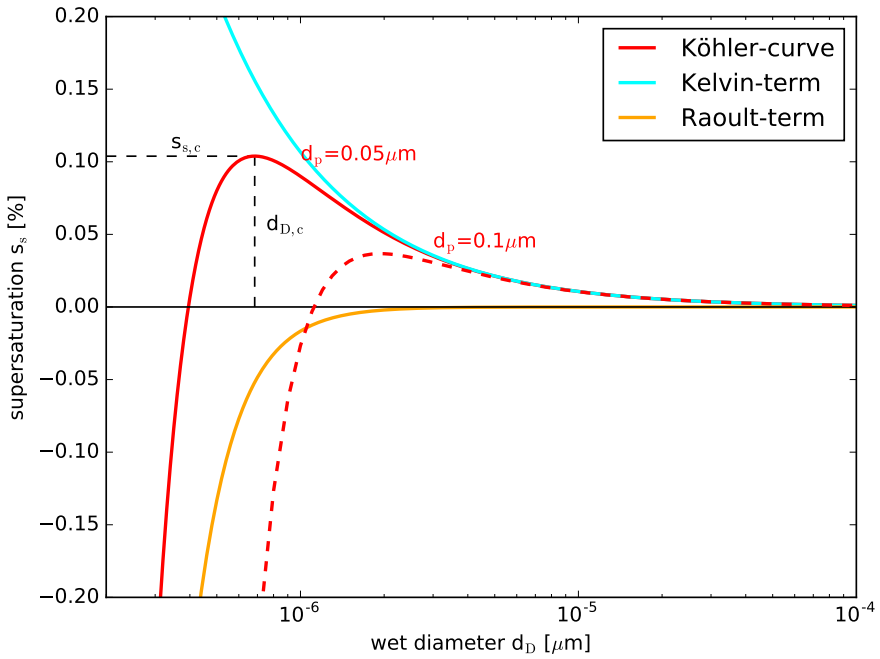

Fig. 2.4.: Köhler curve (red) describes the equilibrium supersaturation (s_s) for two different dry diameters d_p as a function of the wet diameter d_D for temperature of 293 K. Both, the Raoult-effect (orange) and Kelvin-Effect (blue) contribute to the Köhler curve. The critical diameter $d_{D,c}$ corresponds to a critical supersaturation $s_{s,c}$.

of solute in mol. The Köhler curve (Figure 2.4), shown in red for a sodium particle with dry diameter d_p of 0.05μm and 0.1μm, combines two opposing effects: The Raoult (orange) and the Kelvin-Effect (blue). First, with increasing dissolved matter (i.e. salt), the equilibrium saturation becomes lower (Raoult-Effect, first term in Equation 2.5). Second, the smaller the droplet, the higher the curvature and hence the higher the equilibrium saturation (Kelvin-Effect, second term in Equation 2.5). With increasing droplet diameters both curves converge. Towards smaller droplet diameters, the Raoult-effect (~$1/d_D^3$) shows a higher sensitivity than the Kelvin-effect (~$1/d_D$). Once the wet diameter of the droplet exceeds the critical threshold $d_{D,c}$, droplets are activated and start growing as they require less and less supersaturation, whereas droplets below $d_{D,c}$ are stable and will return to their equilibrium state as a response to small changes in their diameter.

In warm rain clouds (liquid phase), activated CCN will grow towards larger droplets and are consequently crucial for rain formation in these clouds. The droplets grow by collision and subsequent coalescence with other droplets (Tao et al., 2012). According to Seifert and Beheng (2006), the collision-coalescence process is categorized into three different size regimes: autoconversion (cloud droplets collide to form raindrops), accretion (growth of raindrops by collecting cloud droplets), and self-collection (cloud droplets collide and remain cloud droplets). In mixed-phase clouds (liquid and ice phase), the formation of primary ice crystals can occur via homogeneous nucleation, i.e. freezing of cloud droplets in

Tab. 2.1.: Aerosol indirect effects on radiation at the surface (R_{SRF}) and precipitation (adapted from Lohmann and Feichter (2005))

Name	Description	R_{SRF}	Precipitation
Cloud albedo effect (Twomey effect)	More but smaller cloud droplets reflect more solar radiation	negative	n/a
Cloud lifetime effect (Albrecht effect)	Smaller cloud particles reduce precipitation efficiency and extend cloud life time	negative	decrease
Surface energy balance	Enhanced aerosol and cloud optical thickness decrease surface raditation	negative	decrease
Semi-direct effect	Absorption of solar radiation by black carbon enhances evaporation	negative	decrease
Glaciation effect	More ice nuclei increase precipitation efficiency	?	increase
Thermodynamic effect	Smaller droplets delay onset of freezing	?	in- or decrease

the absence of nuclei (below -35°C) or heteorogeneous ice nucleation for which an IN is required, which has been studied in various laboratory experiments (Hoose and Möhler, 2012). The latter occurs via: Depositional nucleation (vapor deposits onto ice nuclei), contact freezing (a supercooled droplet freezes by collision with an ice nuclei), immersion or condensational freezing (freezing of a droplet initiated by an IN suspended in it (Lamb and Verlinde, 2011)). Once ice particles have formed, they mainly grow by depositional growth or by aggregation. Since the supersaturation with respect to ice is lower than with respect to water, ice crystals will grow by deposition of vapor and hence depositional growth is very efficient in mixed-phase clouds (Wegener-Bergeron-Findeisen process (Lamb and Verlinde, 2011)). In collision processes, two ice crystals (aggregation) or a droplet and ice crystal can collide (riming) and depending on the resulting size they are called hail, graupel, rimed ice or snow. Of course these particles can then likewise undergo riming and aggregation.

Aerosols impose a main effect on clouds as they change the radiative properties, which assigns them a highly important role in the discussion about climate change (IPCC, 2013). Figure 2.5 shows the effects, which will be explained in the following. The direct effect that aerosols have, comprises the scattering and absorption of solar and infrared radiation. In essence, the aerosol composition and size distribution determines the scattering and absorption behaviour (Haywood and Boucher, 2000). Next to the direct effects, aerosols modify radiative properties indirectly and impact precipitation. Table 2.1 lists these

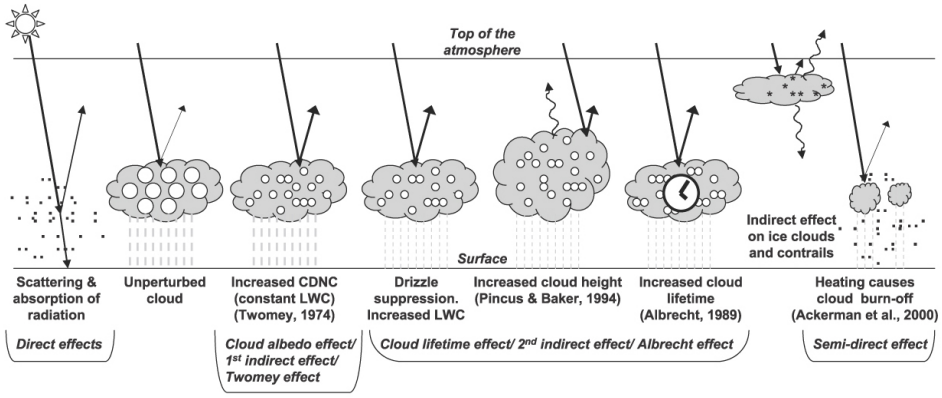

Fig. 2.5.: Schematic diagram showing the various radiative mechanisms associated with cloud effects that have been identified as significant in relation to aerosols (modified from Haywood and Boucher (2000)). The small black dots represent aerosol particles; the larger open circles cloud droplets. Straight lines represent the incident and reflected solar radiation, and wavy lines represent terrestrial radiation. The filled white circles indicate cloud droplet number concentration (CDNC). The unperturbed cloud contains larger cloud drops as only natural aerosols are available as cloud condensation nuclei, while the perturbed cloud contains a greater number of smaller cloud drops as both natural and anthropogenic aerosols are available as cloud condensation nuclei (CCN). The vertical grey dashes represent rainfall, and LWC refers to the liquid water content. Figure taken from IPCC, 2007 (Figure 2-10).

effects: By enhancing CCN, more numerous but smaller droplets prolong the cloud life time (Albrecht, 1989), which would result in a reduced precipitation efficiency and in increased cloud height. Smaller cloud droplets lead to brighter clouds which are more reflective to sunlight (Twomey, 1977), enhancing the albedo of clouds. These first two effects have been detected in observations of perturbed marine stratus clouds by ship tracks (Feingold et al., 2003; Penner et al., 2004), and reduce surface and global mean radiation (IPCC, 2013). In polluted conditions, cloud optical thickness is increased and therefore net surface radiation is reduced as well, which has been deduced from observational studies for industrial regions in the northern hemisphere (e. g. Gilgen et al., 1998). Aerosols impose a semi-direct effect onto clouds as absorption of solar radiation by black carbon heats the air, leading to more evaporation of cloud droplets (Hansen et al., 1997), thereby reducing precipitation. At the same time, absorption in the atmosphere reduces radiation at the surface. Enhanced concentrations of IN lead to a more efficient glaciation, as a consequence of the Wegener-Bergeron-Findeisen process. This reduces cloud lifetime due to enhanced precipitation via the ice-phase (Rogers and Yau, 1989). As a result, cloud cover and cloud optical depth of mid-level clouds reduces, thereby enhancing absorption of solar radiation in the atmosphere (Lohmann and Feichter, 2005). In mixed-phase clouds, smaller cloud droplets as a result of more CCN would delay the onset of freezing, thereby imposing a thermodynamic effect (Tao et al., 2012). The strength and magnitude is still uncertain. Despite that IN are very relevant for nucleation in

mixed-phase clouds, this indicates that changes in droplet concentrations (induced by CCN variations) also affect mixed-phase clouds.

Even though the precipitation response to variations in aerosols is known for most of these indirect effects individually, the interplay of various mechanisms makes it extremely difficult to quantify this response. Because this is a subject of several studies, the recent findings will be reviewed along with the uncertainties in thermodynamic effects on precipitation in deep convective clouds, within the next section.

2.5. Uncertainties in CCN: impact on precipitation

The mechanisms by which CCN impact precipitation is still an open issue and seems to vary between cloud type (Fan et al., 2016), aerosol regime and the environmental conditions (e. g. Seifert and Beheng, 2006; Khain et al., 2008; van den Heever et al., 2011). The lack of understanding is due to missing observational evidence and the complex interaction on various scales. Especially in deep convective clouds (mixed-phase clouds), where dynamics, thermodynamics and microphysics interact, the impact of CCN is more complex than in shallow clouds (Fan et al., 2016).

For deep convective clouds, it has been hypothesized that higher amount of CCN may suppress the warm rain process as the chance of smaller droples to grow via collision-coalescence is reduced. This results in a higher water load at freezing level. When the larger amount of cloud water freezes, more latent heat is released, leading to an invigoration of convection and consequently increased cloud-top height, cloud cover, and additional rainfall (Rosenfeld et al., 2008). However, this theory is questioned in many studies, especially for clouds with strong wind shear, cold cloud base, or in dry conditions (e. g. Fan et al., 2013; Tao et al., 2007; Khain et al., 2008; Altaratz et al., 2014). Fan et al. (2013) propose instead that increasing CCN leads to smaller, but longer-lasting ice particles, thereby influencing deep convective clouds, which increases cloud cover, cloud top height, and cloud thickness.

Noppel et al. (2010) suggest that in simulations of a hailstorm, the environmental condition and case setup determines whether an increase or decrease of precipitation is simulated. Even if increasing CCN could lead to an invigoration, the condensate loss in cases with high CCN could be larger than in conditions with low CCN if precipitating droplets sediment through dry layers (Khain and Pokrovsky, 2004; Khain et al., 2008). Storer and van den Heever (2013) argue that even if invigoration increases cloud condensate, it would be outweighed by the reduction in collision-coalescence. Altaratz et al. (2014) state that the turning point between cloud invigoration and cloud suppression depends on the cloud size and environmental conditions. In small and warm clouds, a decrease in precipitation results from collision-coalescence, whereas stronger updrafts occuring in deeper clouds result in enhanced precipitation (van den Heever et al., 2011).

The limited knowledge in aerosol-cloud interactions has governed the development of different cloud physics paramterizations. The choice of the microphysics scheme can have a greater contribution on the

model result than the aerosol effect itself (White et al., 2017). Consequently, meaningful dependencies between aerosols, clouds, and precipitation are difficult to postulate, as microphysical and dynamical effects may buffer the reaction of changed aerosol conditions (Stevens and Feingold, 2009). Seifert et al. (2012) find for real-case summertime simulations over Germany that whereas increasing aerosols strongly impact cloud properties, their effect on surface precipitation is rather small. Barthlott et al. (2017) find a similar pronounced response on cloud properties but little response on precipitation while changing CCN conditions for a simulated storm over Germany. They argue that evaporation of raindrops at lower levels is the responsible process for this result.

The impact that CCN have on convective precipitation over complex terrain is highly uncertain, because of the interference of microphysical and dynamical processes. Up to now, only a very limited amount of studies has evaluated CCN responses over mountains. Muhlbauer and Lohmann (2008) show in an idealized study that high CCN conditions lead to a enhanced downslope precipitation, but that the magnitude critically depends on the shape of the mountain. Seifert et al. (2012) deduce from a numerical study that low CCN enhance precipitation upstream of the mountain because of the lifting at the flanks in addition to an enhanced warm rain process. Recently, Shrestha et al. (2017) found that most precipitation occurs over the windward side of the mountains for real-case simulations over the Himalayan mountains, due to orographic lifting, rather independent of the CCN perturbations.

Previous studies of aerosol impacts on deep convection usually prescribe CCN conditions from low to high values to distinguish between clean and polluted cases, but do not consider spatial heterogeneities. However, CCN conditions can vary significantly. For example, CCN has been measured to vary during aircraft measurements over Florida up to one order of magnitude within 1000 km (Van Reken et al., 2003). In a model study for southern Germany, Bangert et al. (2011) simulated average boundary layer CCN conditions to vary by about a factor of two within 300 km. For a marine boundary layer, Planche et al. (2017) simulated in a convection-permitting setup CCN variations up to a factor of eight in situations with high wind speeds and still up to a factor of three with moderate wind speeds. The implications of these gradients in CCN conditions for microphysical and dynamical effects on deep convective clouds have thus far not been investigated.

In this work it is investigated how CCN variations affect cloud properties as well as surface precipitation. Real-case numerical simulations are performed for days with weak and strong forcing, respectively, and subsequently homogeneous and heterogeneous CCN perturbations are introduced. The analysis is done for the whole domain and differences compared to the region with complex terrain in south-west Germany and eastern France are pointed out. Based on the current state of understanding aerosol-cloud interactions the following research questions are proposed:

8. How do spatially homogeneous variations in CCN affect surface precipitation and cloud properties over flat and mountainous regions?

9. What is the local and remote effect of spatially heterogeneous CCN conditions on precipitation?

10. Do the results vary depending on the large-scale synoptic condition (i.e. weak or strong forcing)?

2.6. Aims of this thesis

In this project, the contribution of orographic features, land surface heterogeneities and heterogeneities in the aerosol field on cloud formation, cloud characteristics, and subsequent precipitation is investigated. It is also investigated how these results change depending on the the underlying terrain and different meteorological situations. The proposed research questions will be addressed to assess the individual contribution and mechanisms associated with orography, soil moisture and aerosols. At the end, all results will be combined and the following question can be assessed: What is the relative importance of orography, soil moisture and aerosols regarding timing, amount and location of precipitation?

3. Model Setup

3.1. General model description

The COnsortium for Small-scale MOdeling model (COSMO, version 5.3) is used to perform the numerical simulations (Schättler et al., 2016). The model is a non-hydrostatic limited area atmospheric prediction model. It employs an Arakawa C-grid for horizontal differencing on a rotated latitude/longitude grid. In order to obtain initial and boundary conditions for the high-resolution (500 m grid size) simulations, simulations on a coarser grid (2.8 km) are performed first. The 2.8 km setup was also used operationally until May 2018 by the German Weather Service and covers large parts of central Europe (461×421 grid points, Figure 3.1, light blue box). COSMO-EU analyses are used on 7 km resolution to drive the simulations on 2.8 km. In the vertical, these simulations span 50 levels on terrain-following coordinates. Shallow convection is parameterized using a modified Tiedtke scheme (Tiedtke, 1989). No parametrization is used for deep convection. A two-time-level Runge-Kutta method (Wicker and Skamarock, 2002)

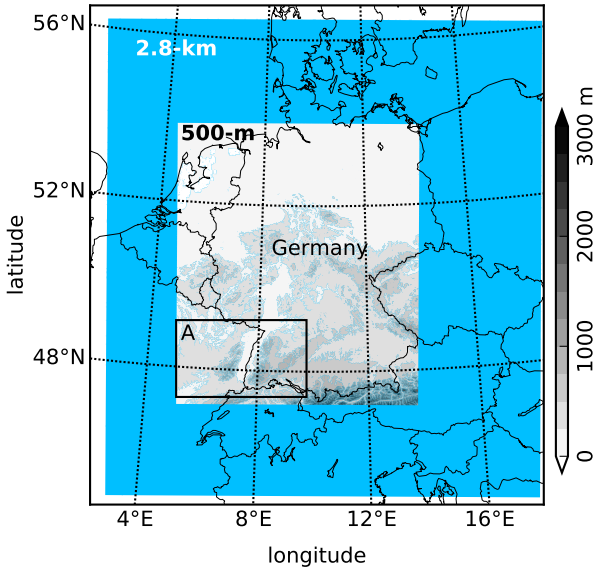

Fig. 3.1.: COSMO simulation domains with 2.8-km (blue) and 500-m (orography) grid spacing.

for time integration is used in the model and the time step is 25 s. In contrast to the operational setup, a double-moment cloud microphysics scheme (Seifert and Beheng, 2006) is used in these simulations. Two-moment schemes were developed to simulate aerosol effects on cloud microphysics and have been found to better represent clouds and cloud feedbacks (Igel et al., 2015), and they are therefore worth

the extra computational cost. The double-moment scheme predicts mass, and number densities of six hydrometeor classes (cloud water, rain water, cloud ice, snow, hail, and graupel) and allows for varying the aerosol concentrations. The reference aerosol assumption represents a continenal case, which is typical for central Europe (Hande et al., 2016). Furthermore, three other prescribed conditions can be chosen to mimic maritime, intermediate and polluted conditions. The activation of cloud condensation nuclei is calculated using pre-calculated activation ratios from Segal and Khain (2006), which depend on the vertical velocity at cloud base and the aerosol properties (Noppel et al., 2010). A 1-D turbulence scheme, classified as Mellor-Yamada level 2.5 (Mellor and Yamada, 1974), is applied, which is based on a prognostic equation for the turbulent kinetic energy.

The external parameters for the soil properties are taken from the Harmonized World Soil Database (HWSD). Terrain elevation is based on 30 arcsec (1 km) gridded, quality-controlled Global Land One-km Base Elevation Project (GLOBE) and the land-use characteristics are taken from the GLOBCOVER Database (Bontemps et al., 2011). The soil processes are simulated using the six-layer soil model TERRA-ML (Doms et al., 2011). Preprocessing of initial and boundary data for the model is done with the preprocessor INT2LM (Schättler, 2016).

Simulations are performed with 500-m horizontal grid spacing, using the output from the 2.8-km domain as initial and boundary conditions. The domain size is reduced to approximately 750 $\times$ 700 km covering most parts of Germany and eastern France (1510$\times$1300 grid points, Figure 3.1, box showing terrain height). The number of vertical levels is increased to 80, with 18 levels in the lowest kilometer. In the 500-m simulations, no parametrization is used for convection. Turbulence is parameterized with a 3-D closure, which uses a 3-D subgrid-scale model with vertical and horizontal turbulent coefficients (Doms et al., 2011) instead of a boundary-layer approximation. To meet the Courant-Friedrichs-Lewy-criterion and allow for numerical stability, the time step is reduced to 3 s. All model runs are initialized at 0000 UTC with an integration time of 24 h. Unless stated otherwise, the results are evaluated for evaluation area A (Figure 3.1, black box), which is characterized by complex terrain.

3.2. Sensitivities

3.2.1. Modifications in orography

As a first set of simulations, the orography is modified in the 500-m simulations by smoothing out valleys or flattening mountain ranges. When the terrain is modified, the preprocessor INT2LM extrapolates the necessary fields to the new surface. This is done such that the atmospheric profile is divided into a boundary layer and a free atmosphere above at the model level, which corresponds to a pressure of roughly 850 hPa. This derived boundary layer is shifted as a whole to the new surface and the forming space either filled with constant values (for vertical velocity, relative humidity and pressure perturbations) or extrapolated based on the gradient at the 850 hPa level (for temperature, horizontal wind). A forecast

Tab. 3.1.: Overview of the orography perturbations

Name	Orography
EXT1000	external parameters with 1 km resolution *
EXT2800	external parameters with 2.8 km resolution *
EXT7000	external parameters with 7 km resolution *
NOVOS	Vosges (VOS) flattened to mean height of 300 m
NOBF	Black Forest (BF) flattened to mean height of 200 m
* interpolated on model grid	

time of 1–2 h is used to spin up the simulations. This technique was also successfully applied by Barthlott et al. (2016) and Ehmele et al. (2015).

Table 3.1 shows the orography perturbations and their abbreviations, which were used for these simulations. The reference orography is shown in Figure 3.2 (a). To deduce the effect that individual valleys have on convection, external terrain features (height, land-use, roughness length etc.) are interpolated from 7 km (EXT7000), 2.8 km (EXT2800) and 1 km (EXT1000) to the 500-m model grid (Figure 3.2(b)–(d)), respectively. To investigate the impact of individual mountain ranges on convection, the Vosges and the Black Forest region are flattened and set to a mean height of 300 m and 200 m, respectively (Figure 3.2(e)–(f)). The flattening is done by applying a smoothing function (Langhans et al., 2011) to the 500-m reference orography in the area of the Vosges or Black Forest. The mean heights were chosen such that they match the nearby orography.

3.2.2. Modifications in soil moisture

For the simulations with soil moisture perturbations, the initial relative soil moisture content is changed for all six days of investigation in eight different ways (Table 3.2). The relative water content (RWC) at each grid point is derived from the volumetric water content (VWC), the wilting point (WP) and porosity (PO), which are characteristic for the present soil type, in the following way:

$$RWC = \frac{VWC - WP}{PO - WP} \qquad [3.1]$$

A simulation with a spatially homogeneous soil moisture content $\overline{w}_{so}$ is performed at model initialisation (SM_UNI). $\overline{w}_{so}$ is the same as for the reference case (Figure 3.3, top left). The bias experiments comprise simulations with 25% increased (SM_125) or decreased (SM_075) soil moisture at each grid point. In the chess board simulations tile structures with grid lengths of 10 km (Figure 3.3, SM_10k, bottom left), 56 km (Figure 3.3, SM_56k, bottom center) and 112 km (Figure 3.3, SM_112k, bottom right) are implemented. The soil moisture content is increased (decreased) by 25% of the domain averaged water content within the tiles, thereby keeping domain-averaged soil moisture content the same. When

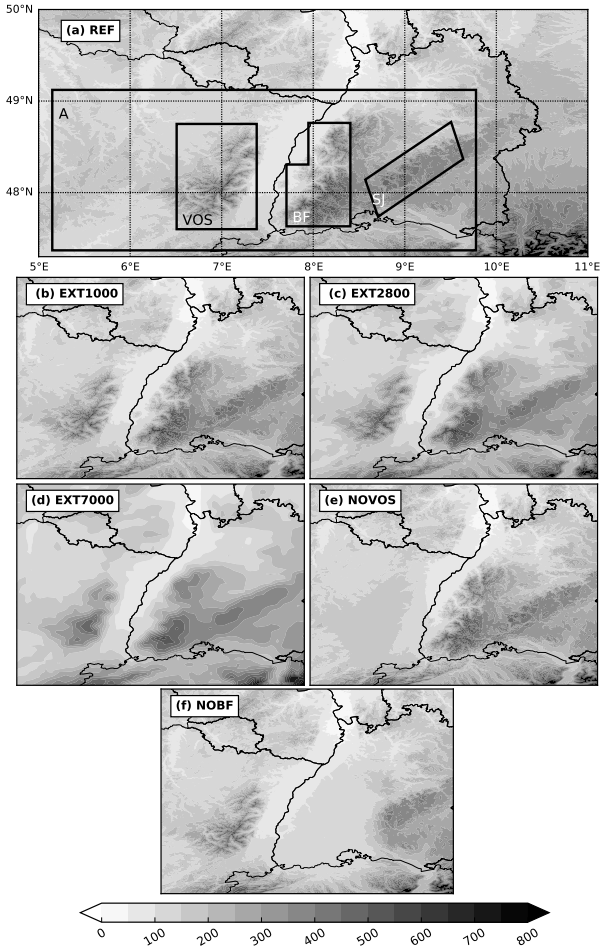

Fig. 3.2.: Model orography (m above msl) of the reference run (a) and the sensitivity runs (b)–(f). The Vosges mountains in eastern France are depicted VOS, the Black Forest mountains in south-west Germany BF and the Swabian Jura SJ. Domain A describes the evaluation domain.

Tab. 3.2.: Overview experimental design for soil moisture simulations

Type	name	water content	patch length
Uniform	SM_UNI	$\overline{w}_{so}$	full domain
Bias	SM_075	-25% w_{so}	each grid point
	SM_125	+25% w_{so}	each grid point
Chess board	SM_10k	+/-25% $\overline{w}_{so}$ (wet/dry)	10 km
	SM_56k	+/-25% $\overline{w}_{so}$ (wet/dry)	56 km
	SM_112k	+/-25% $\overline{w}_{so}$ (wet/dry)	112 km
Random	SM_RS	+/-25% $\overline{w}_{so}$ (wet/dry)	~10km
	SM_RM	+/-25% $\overline{w}_{so}$ (wet/dry)	~25km

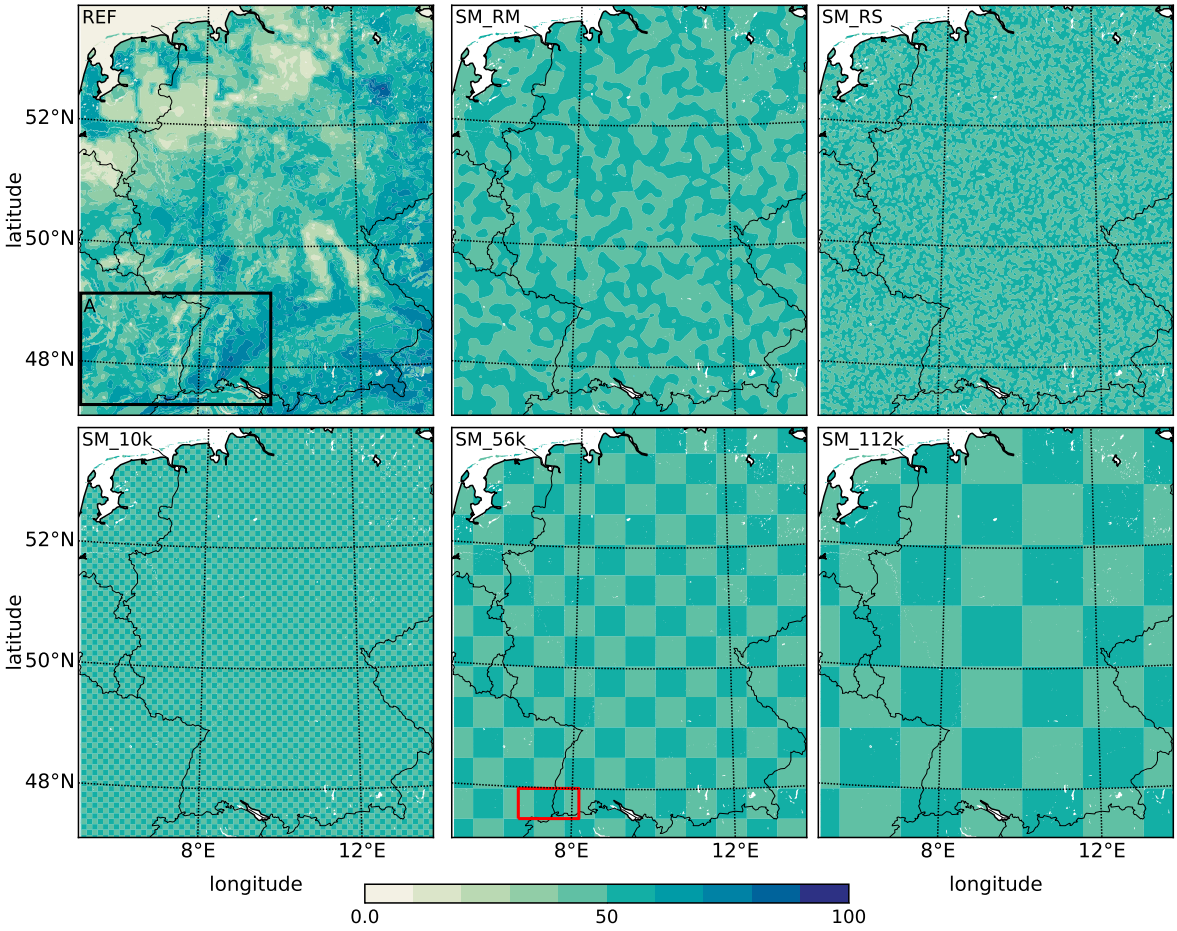

Fig. 3.3.: Initial relative soil moisture content (%) on 1 July 2009 for the reference case (REF, top left), the random simulations with medium (SM_RM, top center) and small (SM_RS, top right) patch size, and the chess board simulation with 10 km (SM_10k, bottom left), 56 km (SM_56k, bottom middle) and 112 km (SM_112k, bottom right) grid length. Area A shows the evaluation domain for this study. The red box highlights the pattern, which is moved through area A for Figure 4.27.

distributing the two discrete values of 25% increased and decreased mean soil moisture randomly, two sets of simulations are obtained: In the simulations with small random structures (Figure 3.3, SM_RS, top right) the average number of connected grid points within the latitudinal or longitudinal direction is around 20 (10 km), which resembles the SM_10k case. In the simulations with larger random structures (Figure 3.3, SM_RM, top center), this average is roughly 50 (25 km). The simulations with random soil moisture patterns are unique, as in previous studies only equally shaped patches have been implemented.

3.2.3. Modifications in aerosols

The impact of aerosols on clouds and precipitation is investigated by prescribing various CCN (cloud condensation nuclei) concentrations, both spatially homogeneous and heterogeneous. The two-moment microphysics scheme in the model allows for four different prescribed CCN concentrations: Maritime

Tab. 3.3.: Overview of the aerosol perturbations

Name	mean CCN concentration	Description
MAR	$100\,\mathrm{cm}^{-3}$	homogeneous maritime concentrations
INT	$500\,\mathrm{cm}^{-3}$	homogeneous intermediate concentrations
CON*	$1700\,\mathrm{cm}^{-3}$	homogeneous continental concentrations
POL	$3200\,\mathrm{cm}^{-3}$	homogeneous polluted concentrations
VAR	$1675\,\mathrm{cm}^{-3}$	chess patterns with maritime, intermediate, continental and polluted patches

**reference simulation*

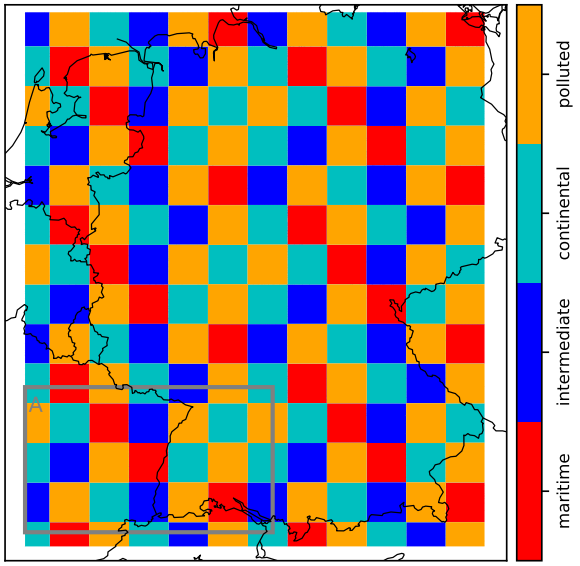

Fig. 3.4.: CCN concentrations for spatially heterogeneous experiments (VAR).

($100\,\mathrm{cm}^{-3}$), intermediate ($500\,\mathrm{cm}^{-3}$), continental ($1700\,\mathrm{cm}^{-3}$) and polluted ($3200\,\mathrm{cm}^{-3}$). The continental CCN concentration is used in the reference simulation for the orography and soil moisture experiments. All experiments with their abbreviations and CCN concentrations are listed in Table 3.3. To invoke spatial variability, chess board patterns (VAR) with a size of $56\times56\,\mathrm{km}^2$ are used, which have one of the four prescribed CCN concentrations. Figure 3.4 shows the distribution of CCN concentrations within the chess board patterns. The perturbations were designed such that the domain mean is close to the continental (reference) CCN concentration and all concentrations are represented. However, the location was chosen randomly. The average concentration in the domain is $1675\,\mathrm{cm}^{-3}$ and in evaluation area A $1687\,\mathrm{cm}^{-3}$, respectively. As for the runs with homogeneous aerosol concentrations, the size distribution is also updated in the variable CCN run in each cell. In all simulations, the CCN concentration is constant up to a height of 2 km and decreases exponentially above.

3.3. Cases analysed[1]

In this study we focus on six cases, which can be classified into weak and strong large-scale synoptic forcing and represent synoptic conditions, which often occur in this area. Figure 3.5 shows the synoptic conditions based on 7-km COSMO-EU analyses of the selected cases at 1200 UTC. On 1 July 2009 and 30 June 2009 (Figure 3.5(a) and (b)), a high pressure system was found over Europe at the surface. A ridge in the middle troposphere was located over France on 30 June 2009 which penetrated further north, and amplified on 1 July. The dominant mid-tropospheric wind direction in south-west Germany was from the north-west (30 June 2009) and north-east (1 July 2009). Figure 3.6 shows the RADar-ONline-ANeichung (RADOLAN) product (Winterrath et al., 2012) for the days of investigation. This product combines radar data with hourly surface precipitation measurements from about 1300 rain gauges. On 1 July and 30 June 2009, precipitation occurred in small cells, with accumulations more than 80 mm locally (Figure 3.6(a) and (b)). On 30 June 2009, precipitation fell mostly over western and eastern Germany, as well as in south-west Germany. On 1 July 2009, local small-scale precipitation occurred, except in north-west Germany, where no precipitation fell. On 23 July 2013 (Figure 3.5(c)), central Europe was dominated by a ridge stretching from the Alps to the North Sea and two low pressure systems were located west of the British Isles and over north-eastern Europe. This lead to westerly winds in south-west Germany. Precipitation was organised in convective cells over central, west and south-west Germany, and local amounts exceeded 80 mm.

The synoptic conditions for the cases with strong synoptic forcing are shown in Figure 3.5 (bottom row). On 11 September 2013 (Figure 3.5(d)) a low pressure system was located over northern Germany. This resulted in a strong cyclonic flow, also visible in the precipitation distribution (Figure 3.6(d)). The main precipitation occurred over south-west and central Germany. South-east and north-east Germany were free of precipitation. The conditions on 11 September 2011 (Figure 3.5(e)) show a low pressure system north of the British Isles. A band of high precipitation was oriented in a north-easterly direction over central Germany. In the rest of the model domain, the precipitation was more stratiform with embedded deep convection. The wind was from the south-west. On 28 July 2013, a low is situated east of Scotland (Figure 3.5(f)). Germany was located ahead of the long wave trough. Mid-tropospheric south-westerly winds were present. Two main areas of precipitation exceeding 80 mm were observed by the radar over eastern France and south-west Germany (Figure 3.6(f)). Precipitation showed again a banded structure and was oriented with the mean wind in a north-easterly direction.

[1] Published in: Schneider et al. (2018). © Quarterly Journal of the Royal Meteorological Society. With permission from John Wiley & Sons, Inc.

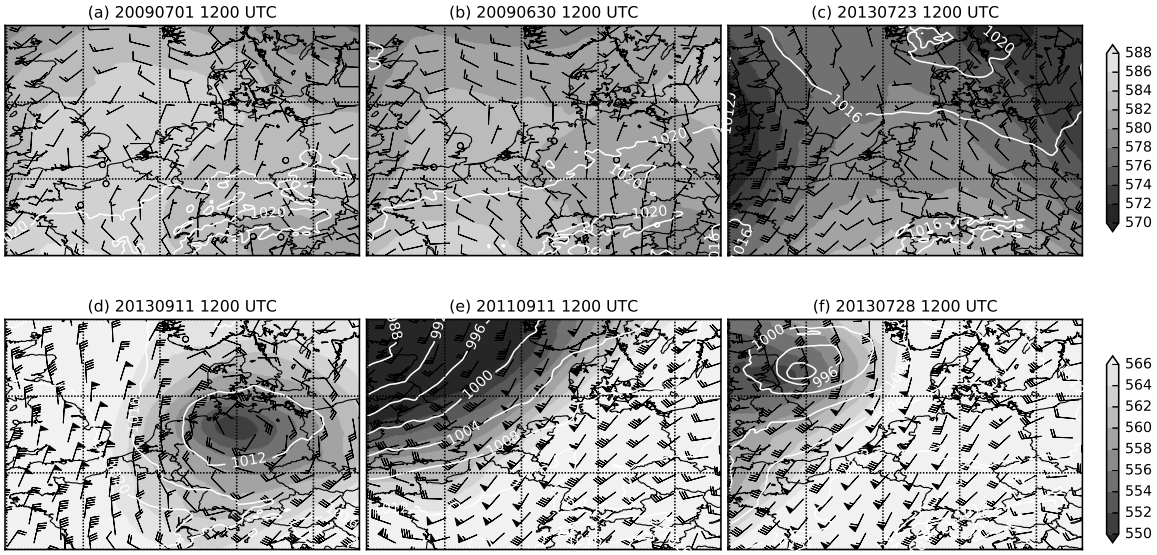

Fig. 3.5.: COSMO-EU 7-km grid length analyses at 1200 UTC for the cases with weak large-scale forcing (top row) and strong large-scale forcing (bottom row) showing 500-hPa geopotential height (gpdm, grey shading), sea-level pressure (hPa, white contours) and 500-hPa wind barbs (black).

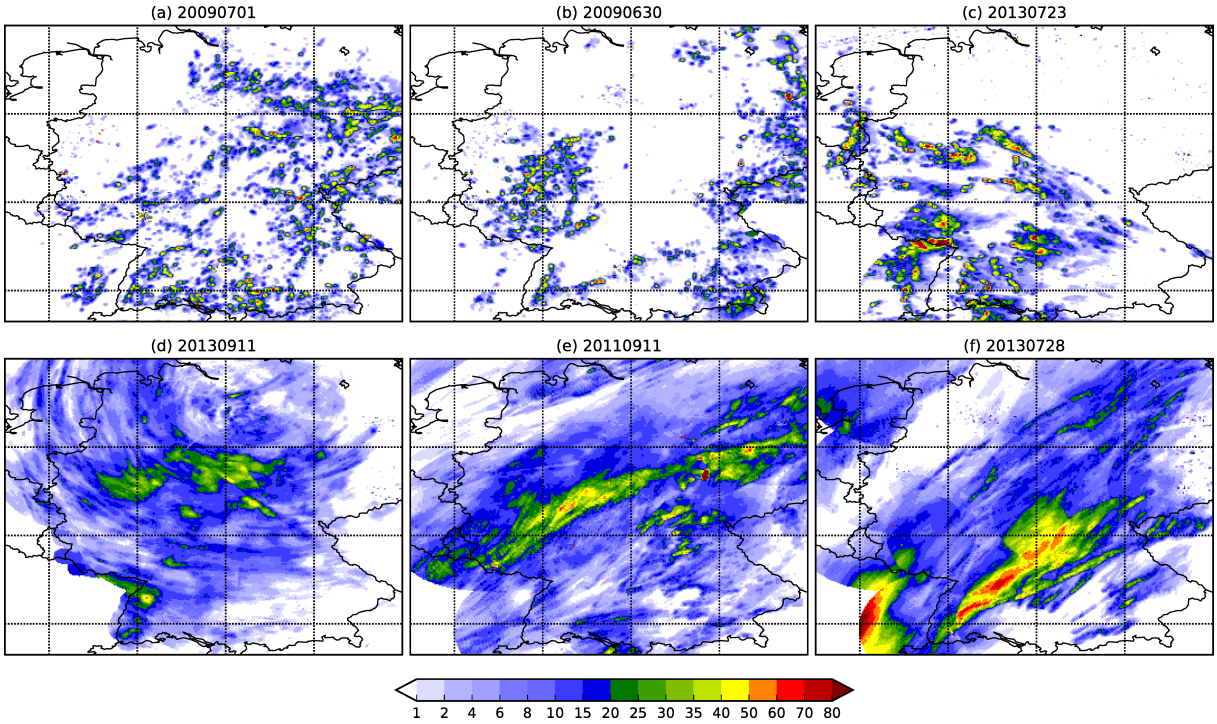

Fig. 3.6.: Radar-derived 24-h accumulated precipitation (RADOLAN) in mm.

4. Results

4.1. Model evaluation against radar data[1]

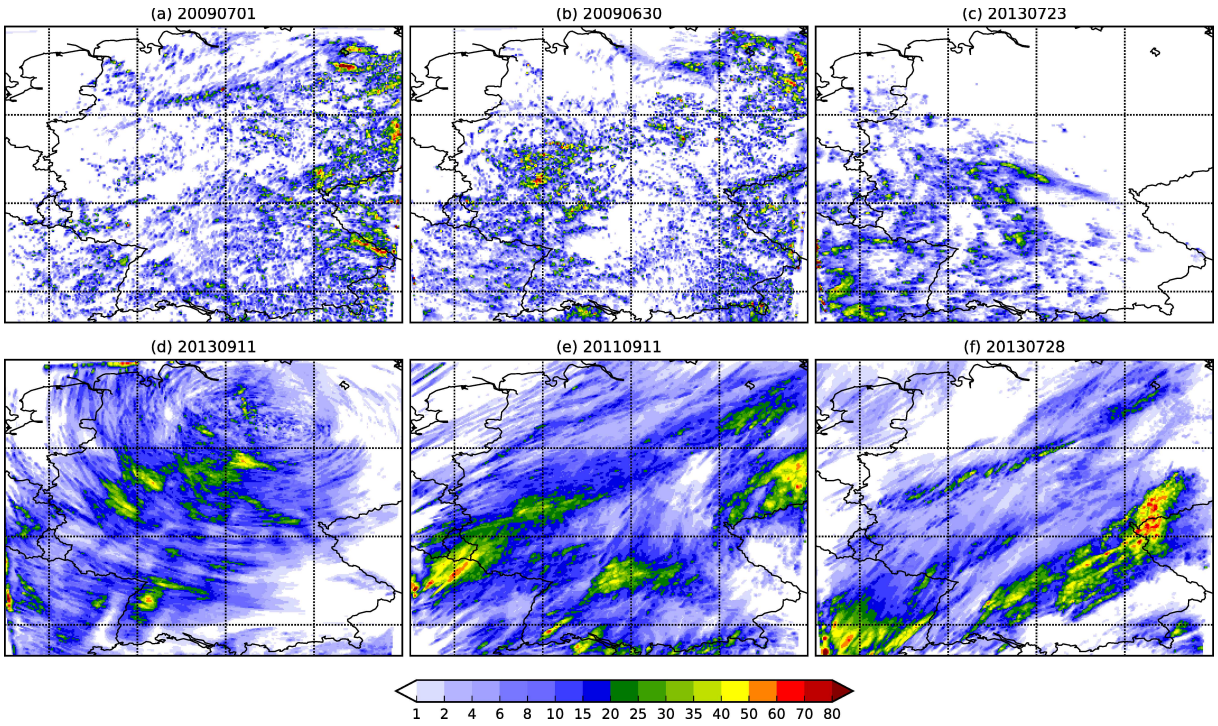

Fig. 4.1.: Simulated 24-h accumulated precipitation in mm for the reference run.

In order to evaluate the reference runs, we compare the 24-h radar-derived precipitation with the simulated precipitation. Because we focus on the sensitivity of the model to different terrain forcing, the evaluation is mostly qualitative.

The location of precipitation under weak synoptic forcing in the simulated REF runs (Figure 4.1) generally agrees well with the radar-derived precipitation (Figure 3.6). On 1 July 2009, the model simulates more precipitation (Table 4.1), over northern and south-western Germany, but captures precipitation over eastern Germany well. In southern Germany, the model locally underestimates the observed amounts of precipitation, but distributes precipitation more widely. On 30 June 2009, differences exist over central Germany since the model simulates more small-scale convective cells than observed. However, mean and maximum precipitation over the whole domain agree well. On 23 July 2013, the model predicts precip-

[1]Published in: Schneider et al. (2018).

Tab. 4.1.: Mean and maximum of reference simulation and radar-derived (in brackets) 24-h precipitation [mm].

Day	Mean	Maximum
20090630	2.4 (1.6)	111 (105)
20090701	1.1 (1.4)	67 (64)
20130723	2.5 (1.3)	48 (100)
20130911	5.9 (5.4)	52 (47)
20110911	7.7 (6.3)	60 (31)
20130728	9.1 (4.4)	69 (80)

itation in central, southern and western Germany, but more widespread and with only 48 mm maximum precipitation, compared to 100 mm seen by radar.

Under strong synoptic forcing, the precipitation amounts between radar and the model differ more than for the cases with weak forcing. However, both data sets show banded structures in the precipitation field oriented in the main wind direction. On 11 September 2013, the simulated and radar-derived data correspond well in location, although the model predicts more precipitation over the elevated mountains in central and south-west Germany. On 11 September 2011, the model predicts more precipitation in the west of the domain compared to the radar. Similarly, more precipitation is simulated in the central part of southern Germany, resulting in a higher mean precipitation. The radar observed a band of precipitation more to the north over central Germany and further to the south in eastern Germany. On 28 July 2013, the precipitation location and amounts over northern Germany are captured rather well by the model. However, in southern Germany, precipitation is shifted eastwards in the model compared to the radar.

Despite the local differences between model and radar, the model reasonably captures the overall precipitation distribution. Differences in the amount of precipitation could also result from small uncertainties in the radar data, as a radar is not an instrument that measures precipitation in a quantitative sense (see e. g. Rossa et al., 2005). For a more quantitative comparison of simulated rainfall to observations, we computed probability density functions of 24-h total precipitation. Under weak synoptic forcing, the probability density function derived from model output agrees well with the radar data (Figure 4.2, top). For all three days, the corresponding lines lie close to each other, however the model underestimates precipitation greater than 10 mm on 23 July 2013. Under strong synoptic forcing, the agreement in relative frequency of precipitation amounts between radar and model is poorer. With increasing precipitation, the deviation between the two data sets becomes larger, especially on 11 September 2013. However, probabilities for large amounts of precipitation are small. To sum up, the COSMO model simulates the general weather patterns of the days analysed reasonably well. Even if not all precipitation is simulated at the right place with the correct intensity, we conclude that these runs serve as a good basis for our analysis, as the focus of this study is the model sensitivity and not a quantitative evaluation or model improvement.

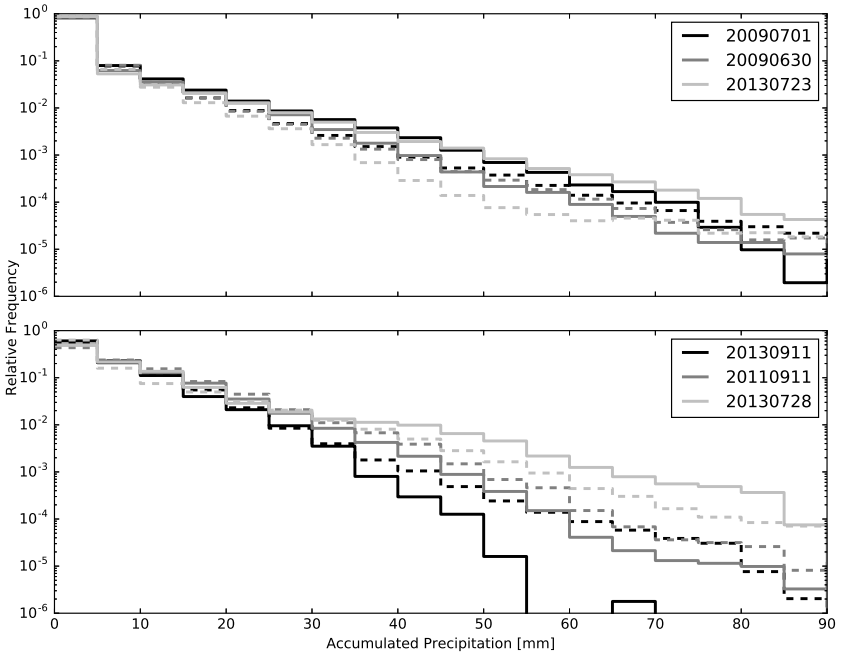

Fig. 4.2.: Probability density function of the 24-h accumulated precipitation for the RADar OnLine ANeichung product (solid) and reference runs (dashed). The top panel shows the days with weak forcing and the bottom panel shows strong forcing.

4.2. Orography[2]

4.2.1. Precipitation amounts in the sensitivity simulations

At first, we analyse the 24-h accumulated precipitation in area A (see Figure 3.2) in the south-western model domain. As can be seen from Figure 4.3, the precipitation amounts differ strongly between the cases with weak and strong synoptic forcing as well as between the individual runs. Days with weak synoptic forcing show amounts of 1–4.5x10^{11} litres, for days with strong synoptic forcing, the precipitation amount lies between 5.8–9.8x10^{11} litres.

A negative relative deviation of up to -21% can be found in 4 out of 6 cases with flattened individual mountain ranges (NOBF, NOVOS). In general, weak forcing days show stronger deviations (relatively to the daily precipitation) than strong forcing days. No systematic behaviour is evident in the runs with smoothed external parameters (EXT1000, EXT2800 and EXT7000). Whereas the deviations are small under strong synoptic forcing (up to 5%), larger deviations exist for weak forcing days (up to 18%).

[2]Published in: Schneider et al. (2018).

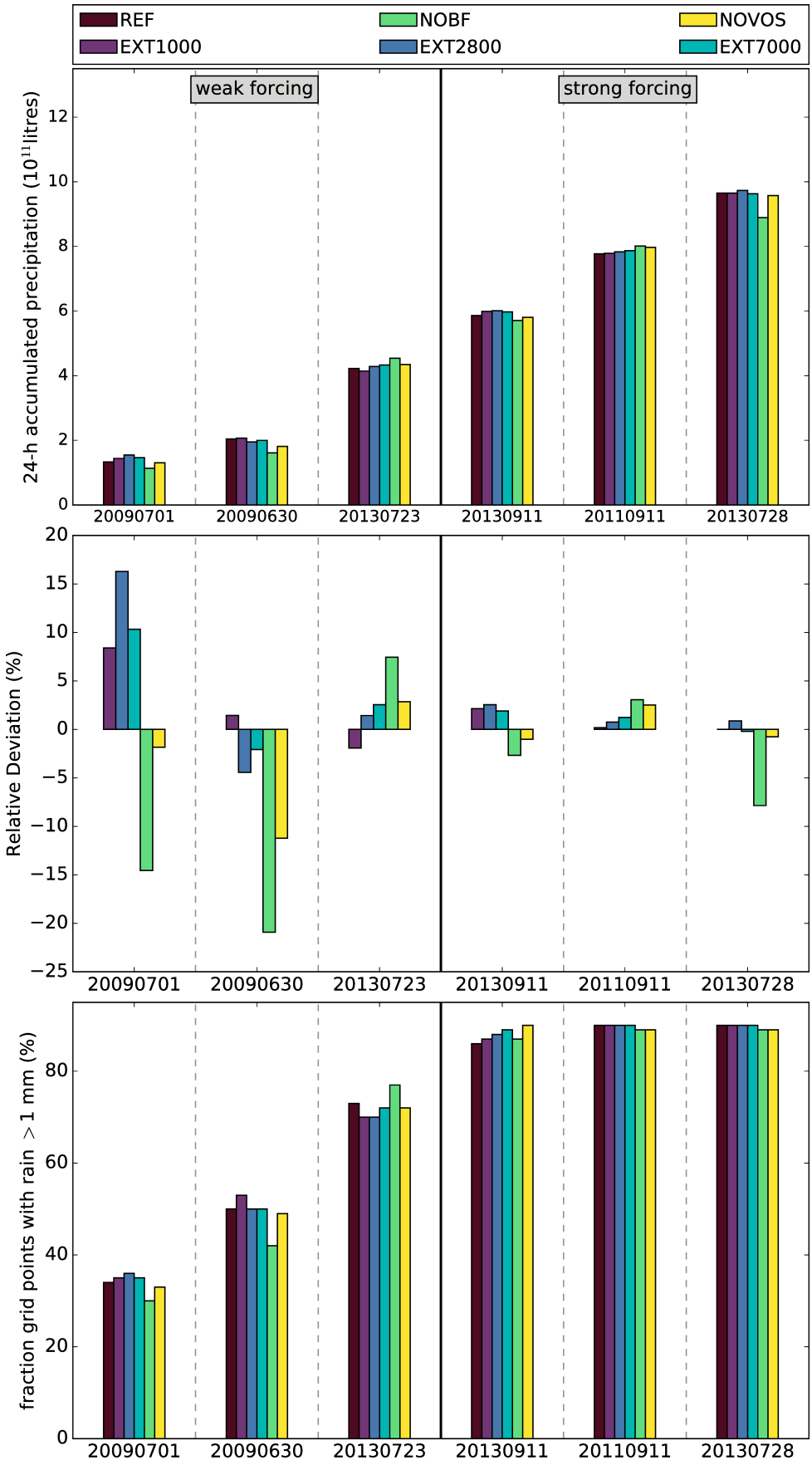

Fig. 4.3.: Top: 24-h precipitation for the cases with weak (left) and strong (right) synoptic forcing, shown for area A (Figure 3.2). Middle: Relative deviation of the precipitation amounts from the sensitivity runs to the reference run. Bottom: Fraction of area that experiences rain in 24-hrs.

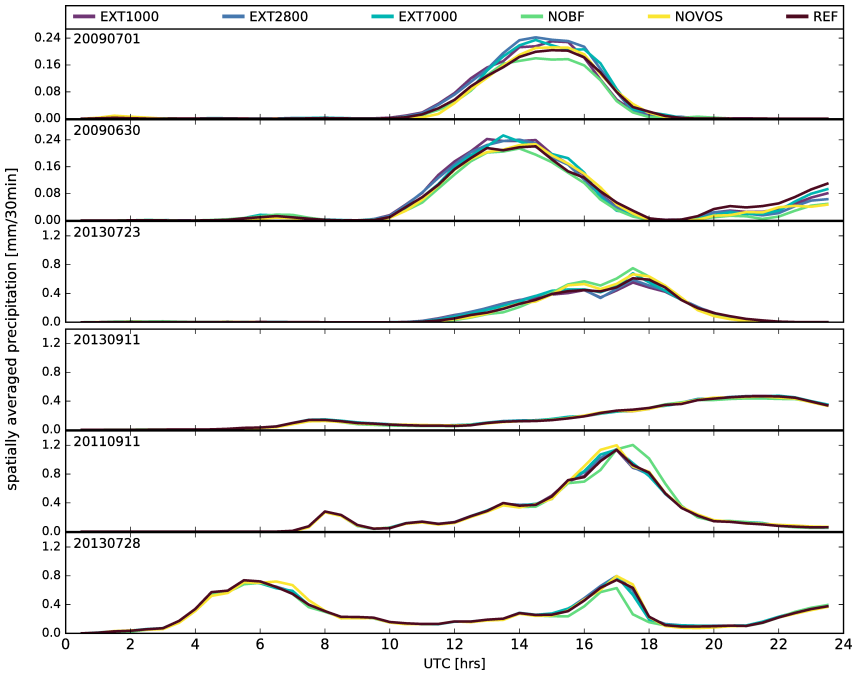

Fig. 4.4.: Domain-averaged precipitation intensity for all days of investigation and all sensitvities. Note the different y-axis scaling for 1 July and 30 June 2009 compared to all other days.

One important quantity to explain the differences in total precipitation is the rain coverage, i.e. the fraction of grid points with an accumulated precipitation greater than 1 mm. Figure 4.3 (bottom) shows that the rain coverage is variable under weak forcing. This quantity explains well the increase in total precipitation, e.g. the runs with smoothed external parameters on 1 July 2009, and decrease in NOBF and NOVOS simulations on 30 June and 1 July 2009. Only on 23 July 2013, when precipitation changes are minor, the area covered with rain does not fully explain the changes. All days with strong forcing show a comparably high, but rather constant, fraction of rainy grid points, as precipitation is distributed widely. The small differences in total simulated precipitation can hence not be attributed to changes in the area covered with rain.

As the fraction of rainy grid points does not explain the total precipitation amounts in several simulations, we now analyse time series of domain-averaged precipitation to identify differences in rain intensity and duration (Figure 4.4). On 1 July 2009, precipitation starts during late morning and reaches its peak in the afternoon, before diminishing. On 30 June 2009 the pattern is simular, but additionally some more precipitation develops after 2000 UTC and the reduced amounts in the EXT2800 and EXT7000 simulations can be explained by less precipitation, though the area covered with rain was similar. On 23 July 2013 the overall pattern and the timings are similar, but higher amounts occur in the NOBF and NOVOS simulation, which explains the increase in total precipitation, even though for the NOVOS simulation, the area with rain is smaller than in the reference run. On 11 September 2013, all simulations show similar patterns. However, the time series as well as the fraction of grid points with precipitation cannot explain the differences in total precipitation. On 11 September 2011, precipitation in

the NOBF run remains larger after 1700 UTC and decreases faster until 1930 UTC, compensating for the weaker increase between 1530–1700 UTC and resulting finally in more total precipitation (Figure 4.3). On 28 July 2013, two maxima exist, between 0500–0700 UTC and at 1700 UTC. Although the timing is identical, differences exist between the simulations and lower values are simulated in the NOBF run, resulting in less total precipitation (Figure 4.3). In general, the domain-averaged precipitation has a similar temporal evolution in all runs. The different precipitation amounts are mainly due to differences in the simulated rain intensities. The reasons for these differences will be analysed in sections 4.2.3 and 4.2.4.

4.2.2. Perturbation propagation

In the runs with flattened individual mountain ranges (NOBF, NOVOS), we modify the terrain in a comparably small part of the model domain. However, we see differences in the simulated precipitation not only in that area, but also at remote locations. For example, Figure 4.5 shows the difference of 24-h accumulated precipitation for 1 July 2009 between the NOBF and the REF run. Less precipitation occurs on average over the region of the Black Forest, when these mountains are flattened. In other parts of the model domain and also upstream of the Black Forest (to the north on this day), positive and negative deviations occur close to each other. These deviations are caused by small spatial shifts of convective cells and not by different temporal evolutions, which we conclude from similar patterns on half hourly basis (not shown). Hohenegger and Schär (2007) found that especially in high-resolution models, initially introduced temperature perturbations can be transported throughout the model domain by sound and gravity waves, and perturbations may even be enhanced where convective instability exists. For all our simulations, we see this small-scale variability related to wave activity. We like to point out that these propagation of perturbations does not influence the total precipitation amount, which remains almost identical in these regions far from the initial perturbation.

4.2.3. Flattened orography

Black Forest

The simulations with smoothed Black Forest show pronounced differences in the 24-h accumulated precipitation over the Black Forest (Figure 4.6). A reduction in precipitation is visible over the Black Forest region marked by the black lines (encompassing the modified orography) on 30 June (-75%) and 1 July 2009 (-56%). On 23 July 2013, an increase in precipitation of 45% is simulated. For weak forcing days, the reduced/increased precipitation over the Black Forest also determines the negative/positive signal seen in the larger evaluation area A (Figure 4.3).

Weak forcing

The local precipitation differences shown in Figure 4.6 can be explained by looking at convection-related variables averaged over the region marked with the black line. Whereas the reference run shows its

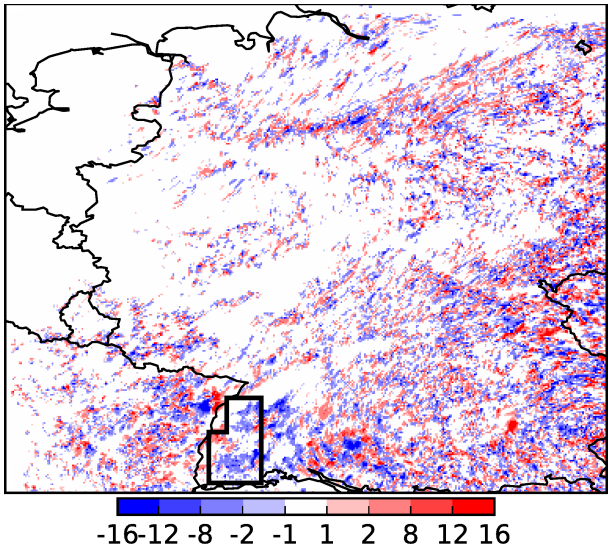

Fig. 4.5.: Difference in 24-h accumulated precipitation in mm of the NOBF run to the REF run on 1 July 2009. The black box denotes the Black Forest region in which orography has been flattened.

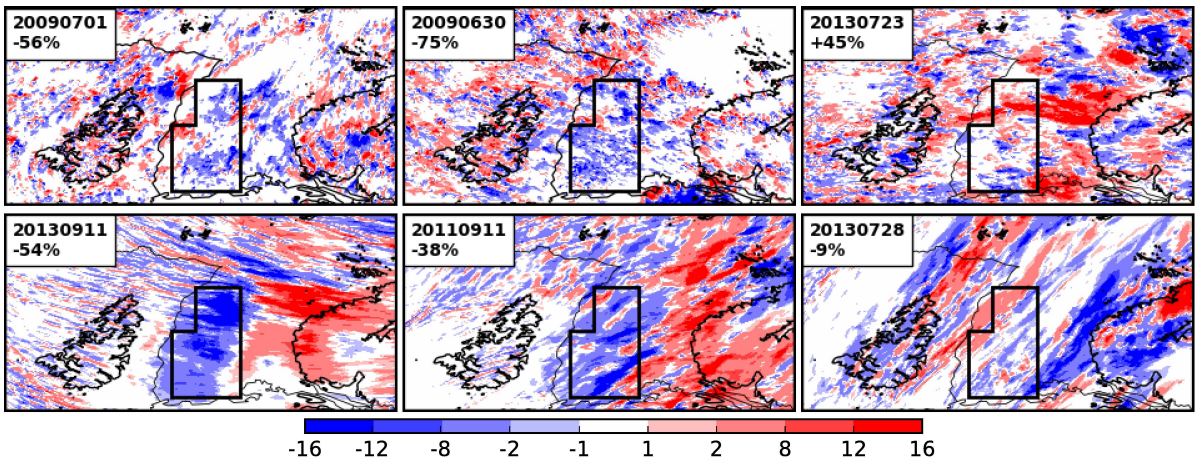

Fig. 4.6.: Difference plot (NOBF-REF) for the 24-h accumulated precipitation in mm. Percentages show relative deviations from the reference run over the Black Forest (black box), where orography has been flattened.

maximum precipitation at 1230 UTC and only a smaller second peak at 1600 UTC, the NOBF simulation reaches its maximum only at 1600 UTC (Figure 4.7 (a)). Despite the peaks at 1600 UTC being at the same time, the rain in the NOBF simulation falls in the flat area west of the Black Forest, whereas it falls over the mountains in the reference run (not shown). Convective available potential energy (CAPE) values increase in both runs from 0600 UTC until the onset of precipitation at 1100 UTC and reach 840 $\mathrm{J\,kg^{-1}}$ (REF) and 1300 $\mathrm{J\,kg^{-1}}$ (NOBF), respectively (Figure 4.7(b)). A second maximum occurs before the maximum precipitation at 1600 UTC (Figure 4.7 (a)). On this day, the systematic offset of about 200 $\mathrm{J\,kg^{-1}}$ in CAPE in the NOBF simulation results from the interpolation routine that our model applies. The atmosphere deepens when mountains are flattened, leading to higher temperatures at the surface. Due to the similar relative humidity, the level of free convection (LFC) is lower which results

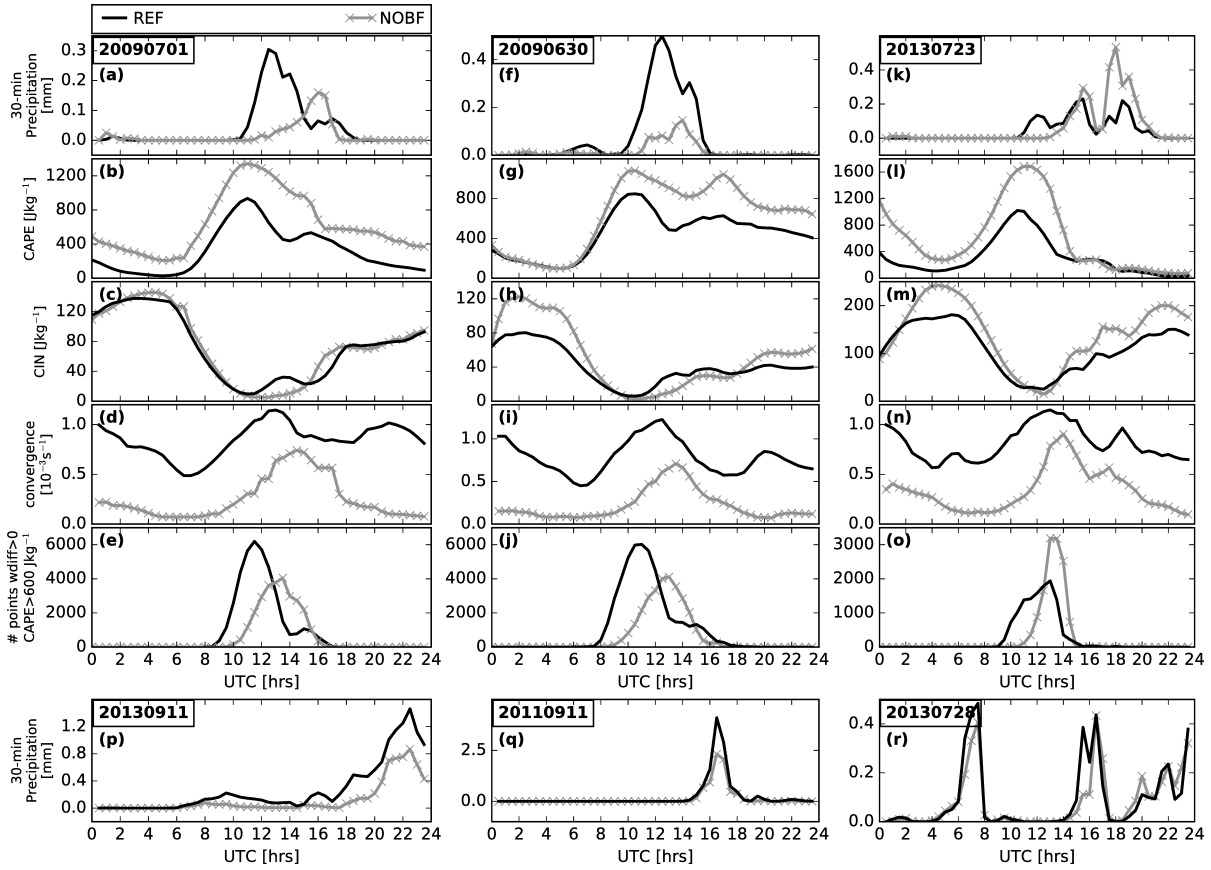

Fig. 4.7.: Domain-averaged precipitation, CAPE, CIN, low-level convergence and number of grid points with $w_{\mathrm{diff}} > 0\ \mathrm{m\,s^{-1}}$ and CAPE $> 600\ \mathrm{J\,kg^{-1}}$ for a region covering the Black Forest on 1 July 2009 ((a)–(e)), 30 June 2009 ((f)–(j)) and 23 July 2013 ((k)–(o)). Domain-averaged precipitation for 11 September 2013 (p), 11 September 2011 (q) and 28 July 2013 (r) in the Black Forest region.

in higher CAPE values at model initialisation. In contrast to CAPE, convective inhibition (CIN) shows a similar behaviour between the reference and the NOBF run. CIN values decrease from 0500 UTC and reach their minimum of 10 $\mathrm{J\,kg^{-1}}$ at 1100 UTC (Figure 4.7 (c)). To release CAPE and by that initiate convection, CIN has to dissolve (i. e. when the near-surface temperature reaches the convective temperature) or be overcome. The latter happens by lifting of air parcels, due to low-level convergence or mountain induced lifting. Trier (2003) stated that the velocity to overcome CIN needs to be higher than

$$w_{\mathrm{CIN}} = \sqrt{2 \times \mathrm{CIN}} \qquad [4.1]$$

The velocity $w_{\mathrm{diff}} = w_{\mathrm{max}} - w_{\mathrm{CIN}}$ describes the difference between the simulated maximum vertical velocity below the level of free convection (w_{max}) and the required updraught velocity to overcome CIN. Positive values of w_{diff} indicate that air parcels can reach their respective LFC, release CAPE and initiate convection. On this day, the 10-m wind convergence, calculated as $(-1) \times (\partial u/\partial x + \partial v/\partial y)$, is much stronger in the REF run as the lack of an elevated heating area and valleys in the NOBF run produces only weak convergence. Already 30 min after model initialisation, values are $1 \times 10^{-3}\ \mathrm{s^{-1}}$, decrease slightly

thereafter and increase from 0630 UTC due to thermally induced winds (Figure 4.7 (d)). The maximum of $1.1\times10^{-3}\,s^{-1}$ is reached when precipitation peaks at 1230 UTC because of convergence created at cold pool boundaries. In the NOBF simulation, the convergence increases similarly during daytime, but reaches its maximum of only $0.7\times10^{-3}\,s^{-1}$ later at 1430 UTC. Although the mountains are flattened, weak convergence occurs even in the absence of terrain height changes, because all original soil and surface properties (e. g. soil moisture) are retained and only the terrain height is changed. Positive w_{diff} values indicate air at the surface that can reach the LFC, but it is not an indicator of whether convection will be initiated or not. Therefore, we counted the number of grid points where w_{diff} is positive and CAPE is higher than $600\,J\,kg^{-1}$. As a result of the stronger low-level convergence, up to 6200 grid points meet these criteria in the REF run. In the NOBF run, only 4000 grid points fulfill these criteria and the maximum is reached 2 h later (Figure 4.7 (e)). These patterns correspond well with the time series of precipitation. To summarise, the low-level wind convergence is crucial to initiate convection. Weaker convergence over flat terrain results in less precipitation.

On 30 June 2009, the overall pattern is similar to the one on 1 July 2009. Precipitation increases from 1000 UTC and peaks at 1200 UTC in the reference run and 2 h later in the NOBF simulation (Figure 4.7(f)). The low-level convergence is weaker in the NOBF simulation (Figure 4.7(i)) and only starts to increase at 0830 UTC. CAPE (Figure 4.7(g)) is higher in the NOBF simulation and can build up more since precipitation is initiated 1 h later in the NOBF simulation. In both simulations, CIN values (Figure 4.7(h)) are equally small between 0800–1100 UTC and hence favour the initiation of convection. The combined parameter of $w_{\text{diff}} > 0\,m\,s^{-1}$ and CAPE $> 600\,J\,kg^{-1}$ shows a clear delay of 2 hours and is satisfied at 30% fewer grid points in the NOBF simulation (Figure 4.7(j)), which is also reflected in the delayed and weaker precipitation. For this day, we find again that the low-level wind convergence is determining the initiation of precipitation. Weaker convergence over the flattened area results in less precipitation, despite the CAPE values being higher.

On 23 July 2013, precipitation starts in the reference run at 1030 UTC and peaks at 1200, 1500 and 1830 UTC (Figure 4.7(k)). In the NOBF simulation, it starts later at 1230 UTC and shows two higher maxima at 1400 and 1800 UTC. The first peak in the reference run is from precipitation over the eastern part of the Black Forest, where the low-level convergence and CAPE are both high (not shown). Over the Black Forest, domain-averaged CAPE can build up more because no convection is initiated and therefore CAPE is around 1100 UTC approximately $1700\,J\,kg^{-1}$, twice as high as in the reference run (Figure 4.7(l)). CIN values are similarly low in both simulations between 1030–1230 UTC (Figure 4.7(m)). Around 1000 UTC precipitation develops over the Vosges region (not shown). The cold pool outflow from this precipitation reaches the Black Forest region around 1200 UTC, the low-level convergence increases (Figure 4.7(n)) and precipitation is initiated over the flat part, where atmospheric instability exists. Around 1330 UTC, 30% more grid points with $w_{\text{diff}} > 0\,m\,s^{-1}$ and CAPE $> 600\,J\,kg^{-1}$ exist in the NOBF simulations. The low-level convergence increases further, resulting in a large convective cell. In the following hours, this produces significant amounts of precipitation over the flat area. The

daily total is therefore higher in the NOBF run. In the reference run, the afternoon precipitating cells are smaller and more isolated (not shown). To summarize, in our simulations, the timing of precipitation over the Vosges region is crucial to initiate precipitation over the flattened Black Forest, as cold-pool induced outflow increases the low-level convergences over the flat area where CAPE had more time to build up.

From these results, we conclude that on days with weak synoptic forcing, the low-level wind convergence over mountainous terrain is the main trigger mechanism to initiate convection. The weaker convergence in the NOBF run on 1 July and 30 June 2009 is not able to trigger convection in the same way, despite higher values of CAPE. However, flattening of the Black Forest can also lead to higher precipitation totals (23 July 2013), which is due to a combination of still sufficient uplift from low-level wind convergence (from cold pool outflow from cells initiated elsewhere) and generally increased atmospheric instability. The combined parameter of $w_{\text{diff}} > 0\ \text{m s}^{-1}$ and $\text{CAPE} > 600\ \text{J kg}^{-1}$ turns out to be a suitable indicator for convection initiation and total precipitation amount.

Strong forcing

Under strong synoptic forcing, all runs show a systematic precipitation decrease over the flattened region (-54% on 11 September 2013, -38% on 11 September 2011 and -9% on 28 July 2013). An amplification occurs east of that region for 11 September 2011 and 2013, where the moist air is forced to ascend at the Swabian Jura (Figure 4.6).

On 11 September 2013, the main precipitation starts at 1500 UTC (Figure 4.7(p)). With two smaller maxima in-between, the highest amount of 1.5 mm $(30\ \text{min})^{-1}$ is reached at 2230 UTC. Precipitation in the NOBF run is always lower, but follows the same characteristic behaviour. CAPE and CIN are both small (not shown), indicating that precipitation is more driven by synoptic-scale processes. Cells are advected from the west into the area of the Black Forest and precipitate more heavily and widespread over the mountains. This corresponds to locations where air is forced to rise and the low-level convergence is high. Because of the strong background flow, we also see changes in precipitation downstream of the Black Forest. In the NOBF simulation, precipitation is initiated over the Swabian Jura, where stronger vertical updraughts exist (not shown). In contrast, the air in the REF run has already passed and precipitated over the (comparably higher) Black Forest (not shown). The combination of reduced precipitation over the Black Forest and enhanced precipitation over the Swabian Jura leads only to a change of -3% in total precipitation within area A (Figure 4.3).

The strong spatial shifts and enhancement of precipitation over mountains, which we discussed for 11 September 2013, happen on 11 September 2011 and 28 July 2013 as well. On 11 September 2011, precipitation falls between 1430–2000 UTC and shows similar timings, but higher amplitudes in the reference run (Figure 4.7(q)). Precipitating clouds which are advected into the area of the Black Forest undergo enhancement when mountains are present, but still exist when orography is flattened (not shown). The relative deviation over the Black Forest on 11 September 2011 is -38% and at the same

time, precipitation over the Swabian Jura is enhanced. This combination of reduced precipitation over the Black Forest and enhanced precipitation over the Swabian Jura also leads to marginal differences of only +3% in area A. On 28 July 2013, precipitation falls around 0730, 1600 and after 1900 UTC and is only slightly higher in the reference run at 0730 and 1530 UTC (Figure 4.7(r)). CAPE values are even smaller than on the other strong forcing days (maximum domain average below $450\,\mathrm{J\,kg^{-1}}$, not shown). Over the flattened mountains, precipitation is reduced in its intensity and even more pronounced differences exist over the Swabian Jura, where more precipitation occurs in the REF run (Figure 4.6). This is because of higher CAPE and lower CIN values, rather than stronger moisture transport (not shown).

We conclude that under strong synoptic forcing, effects attributed to large-scale forcing dominate. We see bands of precipitation, passing over the Black Forest region that are larger and more intense over the mountains. At some locations, small cells in the reference run are totally absent over flat terrain. For 11 September 2011 and 2013, we see an enhancement in precipitation over the Swabian Jura with flattened Black Forest, as a result of more moisture transported towards this region and rising air at the flanks of the mountains. No major difference in moisture is visible on 28 July 2013 and precipitation over the Swabian Jura is enhanced, where CAPE values are high and CIN values are low. For 11 September 2011 and 2013, the reduction over the Black Forest and the intensification downstream over the Swabian Jura are almost equal.

Vosges

The runs with flattened Vosges show a reduction in total precipitation of 16% and 29% for 1 July and 30 June 2009 over this area (area 'VOS' Figure 3.2). On 23 July 2013, the COSMO model simulates a different sensitivity. On this day, an increase in precipitation of 15% is simulated over the Vosges area, when mountains are flattened.

Weak forcing

We now analyse the the mechanisms leading to the initiation of convection in the NOVOS simulations. On 1 July 2009, the precipitation maximum in both simulations is at 1400 UTC, with precipitation stopping around 1600 UTC (Figure 4.8(a)). Although the maximum is slightly higher in the NOVOS simulation, the shorter duration of precipitation leads to a decrease in total precipitation. CAPE and CIN follow the same diurnal cycle as in the NOBF simulation (section 4.2.3, Figure 4.8(b) and (c)). In contrast, the low-level wind convergence increases in the NOVOS simulation up to a surprisingly high value of $0.5\times10^{-3}\,\mathrm{s^{-1}}$ (Figure 4.8(d)). This is also reflected in the combined parameter of $w_{\mathrm{diff}} > 0\,\mathrm{m\,s^{-1}}$ and CAPE $> 600\,\mathrm{J\,kg^{-1}}$, which has similar patterns in the reference and the NOVOS simulation (Figure 4.8(e)).

The flattening of the Vosges mountains leads to a moderate reduction of total precipitation (-16%), whereas the NOBF run shows a much stronger precipitation decrease (-56%) on this day. Thus, we inves-

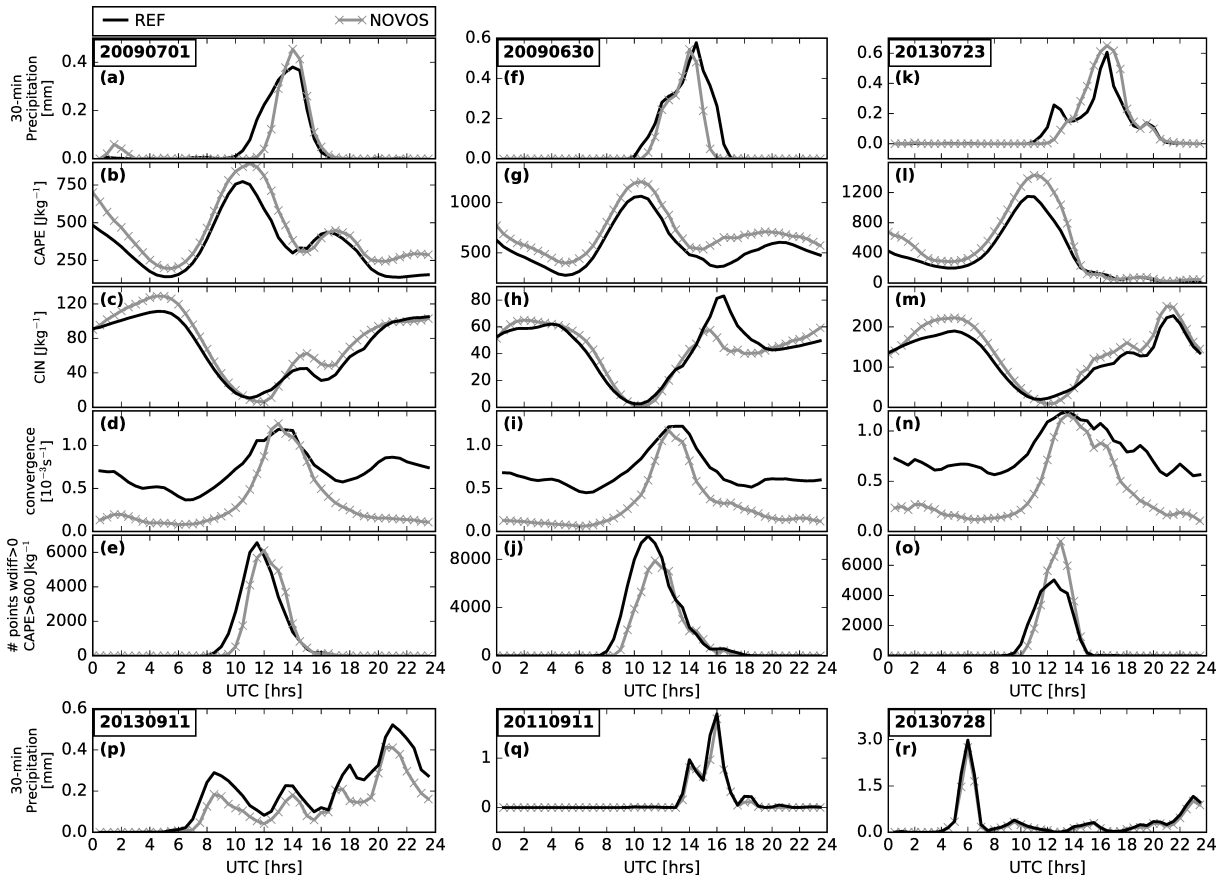

Fig. 4.8.: Domain-averaged precipitation, CAPE, CIN, low-level convergence and number of grid points with $w_{\mathrm{diff}} > 0$ m s^{-1} and CAPE > 600 J kg^{-1} for a region covering the Vosges on 1 July 2009 ((a)-(e)), 30 June 2009 ((f)-(j)) and 23 July 2013 ((k)-(o)). Domain-averaged precipitation for 11 September 2013 (p), 11 September 2011 (q) and 28 July 2013 (r) in the Vosges region.

tigate why the orographic effects of the Vosges mountains are weaker than those from the Black Forest on that day. We find that besides the small temporal shift of 30 min, the fraction of grid points with positive w_{diff} and CAPE > 600 J kg^{-1} is very similar in the NOVOS and REF run (Figure 4.8(e)). On the contrary, there are larger differences between the respective runs for the flattened Black Forest (Figure 4.7(e)). As CAPE is higher in both simulations with flattened mountain ranges when compared to the reference run, we can attribute the higher number of grid points with positive w_{diff} and CAPE > 600 J kg^{-1} mostly to the low-level wind convergence. Whereas the wind convergence for flattened Black Forest is lower than in the reference simulation, the values in the NOVOS run are almost as high as in the reference run before convection starts to develop. The reason for this high wind convergence in absence of the Vosges mountains can be attributed to the formation of boundary-layer rolls in that area. As can be seen in Fig. 4.9(b), the COSMO model with reference orography reveals the signature of boundary-layer rolls (i. e. elongated zones with alternating convergence and divergence) in the low-level wind convergence in the Rhine valley, the region in between the Vosges and the Black Forest. The near-surface wind comes from north to northeasterly directions. These roll-vortices are most probably generated by thermal insta-

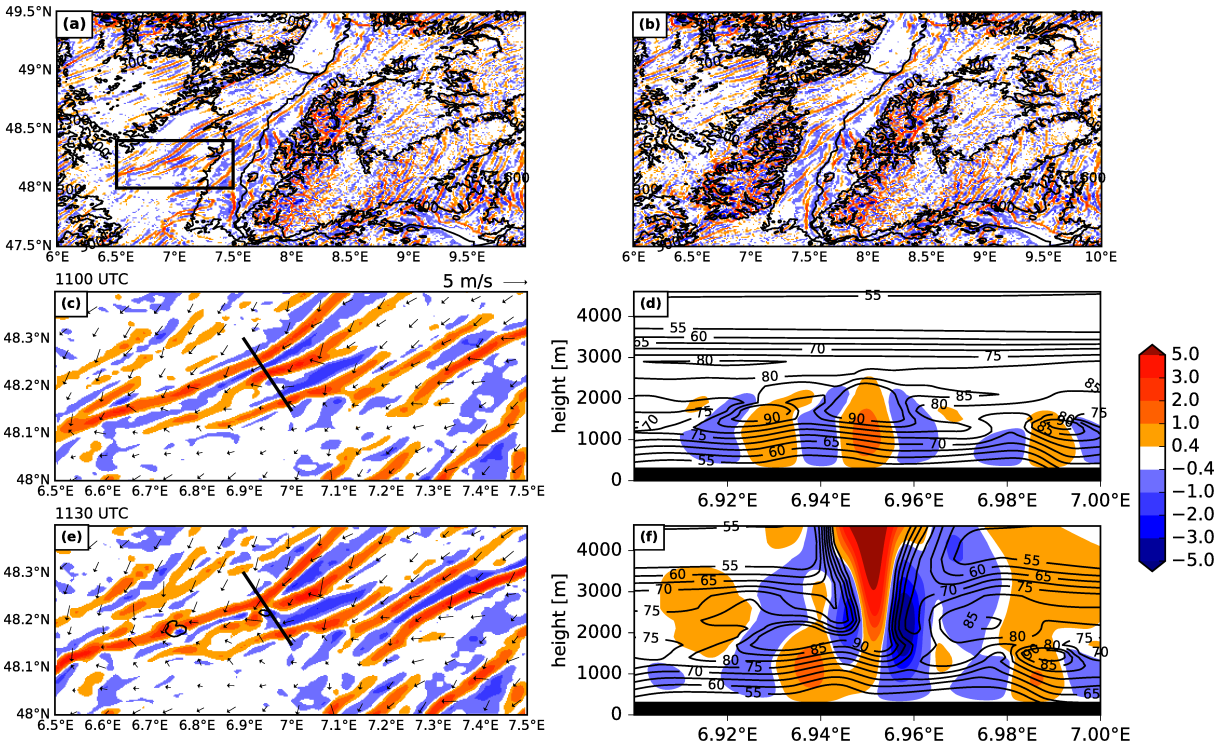

Fig. 4.9.: 10-m wind convergence for the NOVOS run (a) and the REF run (b) and 10-m wind convergence (c,e) and vertical cross section of vertical wind (d,f) (colors, in m s^{-1}) and relative humidity (contours, in %) for 1 July 2009. The rectangle in (a) indicates the domain for (c,e). The black contour lines in (e) indicate 30-min precipitation larger than 0.01 mm.

bility in a convective boundary layer and also evident in cloud streets of shallow cumulus (not shown). According to the review article by Etling and Brown (1993), those rolls have vertical extents of 1–2 km, aspect ratios of 2–15, and downstream extents of 10–1000 km. The length of the rolls lies between 50–150 km and the mean width of the updraft region is approximately 3 km. This means that the COSMO model with operational grid spacing (2.8 km) is not able to resolve these features. As the effective resolution lies between 6–7 times the nominal resolution (e. g. Barthlott and Hoose, 2015), our simulations with 500-m grid spacing are able to resolve those roll vortices. This is in agreement with recent findings from Thurston et al. (2016) who stated that a resolution of less than 600 m is required to resolve the secondary circulation of the rolls and therefore accurately predict their onset, scale and evolution. The zoom into a region with convective precipitation over the flattened Vosges (Fig. 4.9(c)–(f)) reveals that due to daytime heating the wind convergence increases, leading to an intensification and growth of the rolls. At two areas with convergence and updrafts, deep convection is initiated and precipitation starts to fall at 1130 UTC (Fig. 4.9(e)). Thirty minutes later, the typical divergent wind patterns of the convective precipitation is apparent and an almost circular cold pool outflow is simulated with convergence at the leading edge of the convective outflow (not shown). To summarise, the low-level wind convergence is high, even in the absence of mountains, because of the formation of boundary-layer rolls. This low-level

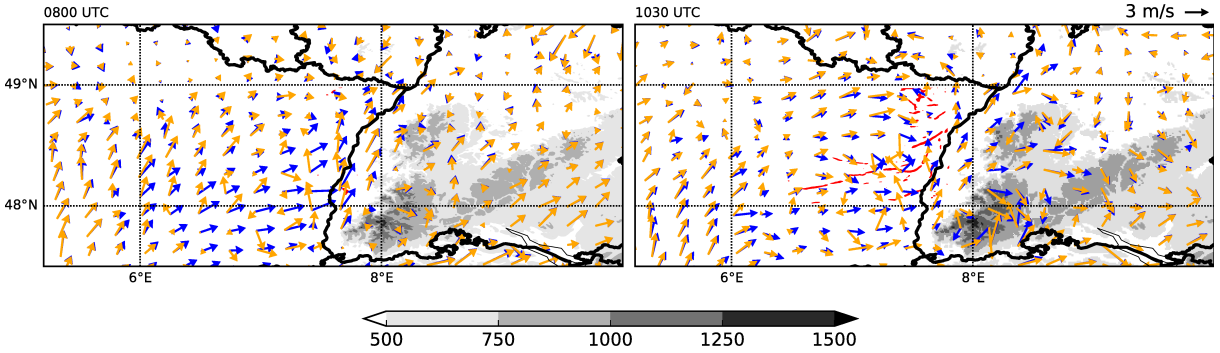

Fig. 4.10.: 10-m wind for the REF (orange) and NOVOS (blue) simulation on 23 July 2013, 0800 UTC (left) and 1030 UTC (right). Grey shading show the orography and red contours convergence > 0 s^{-1} for the subregion of the Vosges (see Figure 3.2 (a)) in the NOVOS simulations.

convergence results in significant precipitation over flat terrain, but still less precipitation than in the reference run.

The mechanisms leading to the initiation of precipitation on 30 June 2009, are very similar to those in the NOBF run. Hence we refer the reader to the explanation in section 4.2.3 and the time series in Figure 4.8 (f)–(j).

In contrast to the two days analysed before, the total precipitation amount on 23 July 2013 increases in the NOVOS simulation compared to the REF run, similarly as in the NOBF run. However, the strong convergence on this day is not a result of roll vortices, but rather a consequence of changing wind direction on larger scales: At 0800 UTC, the wind approaches the Vosges in the reference run from the south-west (Figure 4.10). The flow splits around the Vosges mountains and the eastern branch is channeled in a northward direction west of the Black Forest. In addition, upslope winds are simulated on the eastern crests of the Vosges mountains. In the NOVOS simulation, the wind comes from a southwesterly direction in most parts of the flattened Vosges. When it approaches the Black Forest, the wind is deviated towards the north west of the mountains. The flow in the northern part of the flattened Vosges mountains up to the French border shows a cyclonic shift in the morning hours, probably caused by a shallow heat low over the flat terrain. This leads to the formation of a convergence zone (Figure 4.10) over the central part of the flattened area and results in an increase of the low-level convergence. Where the convergence zones develop in the NOVOS simulation, CAPE values are high and CIN values low. This favours the initiation of convection and precipitation develops here around 1100 UTC (not shown). Hence, precipitation in the NOVOS simulation exceeds the amount in the reference run between 1400–1800 UTC. Consequently, on this day, the high precipitation amounts result from strong low-level wind convergence, which is due to the formation of convergence zones.

We therefore conclude that, as for the Black Forest case, the low-level wind convergence is the main driver for deep convection on days with weak synoptic forcing. Surprisingly, the convergence over the flattened Vosges mountains has a similar strength as when the mountains were present in all three cases.

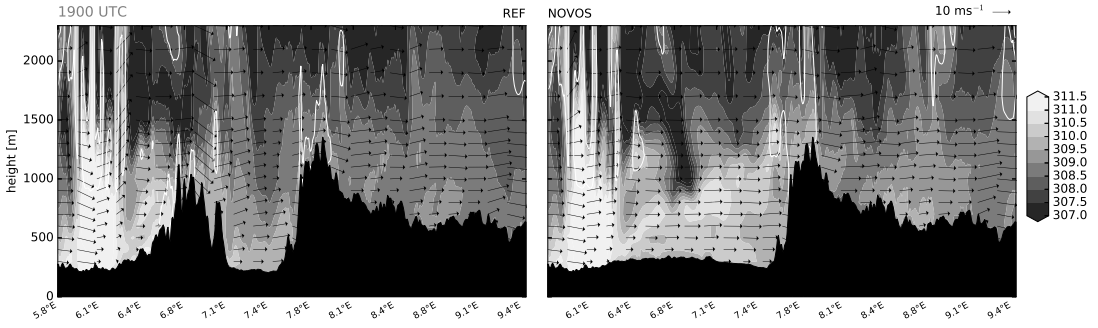

Fig. 4.11.: Vertical cross section showing equivalent potential temperature and contour lines for 0.2 kg m^{-3} cloud ice and cloud water content along 47.85° N on 11 September 2013 at 1900 UTC for the reference run (left) and NOVOS simulation (right). Vertical winds are multiplied with a factor 5 for better visualisation.

This can be attributed to (i) the formation of boundary-layer rolls and (ii) convergence due changes in the large-scale wind direction. As a consequence of the strong convergence and subsequent lifting, the percentage deviations of total precipitation with respect to the reference run are considerably smaller than in the simulations with flattened Black Forest.

Strong forcing

For the days with strong forcing, the precipitation deviations over the Vosges area are -34% (11 September 2013), -15% (11 September 2011) and -14% (28 July 2013). On 11 September 2013 four precipitation peaks occur. There is a time delay of 30 min between the individual peaks in the REF and the NOVOS run (0830, 1400, 1800, 2100 UTC; Figure 4.8(p)). As discussed for the Black Forest case, CAPE is small on this day (not shown)). The low-level convergence is very weak in the case for flattened Vosges (not shown) which reflects the missing orographic enhancement when the mountains are flattened. On this day, the strong synoptic forcing also leads to a redistribution of precipitation: because there is less precipitation over the flattened Vosges mountains, comparably moist and warm air, thus air with high equivalent potential temperature (Figure 4.11), is present west of the Black Forest in the NOVOS simulation. When this air is advected towards the east and ascends at the Black Forest, more precipitation develops.

On the other two days with strong synoptic forcing (11 September 2011 and 28 July 2013), the timing of precipitation is identical in the respective reference and sensitivity runs. Both sensitivity runs show a widespread reduction of precipitation over the region of flattened Vosges mountains. However, and in contrast to 11 September 2013, the wind comes from the south-west. This affects the precipitation pattern downstream of the flattened Vosges more to the north-east.

For the analysed cases with strong synoptic forcing, we conclude that the large-scale precipitation patterns determine the potential for rain in our investigation area. However, on the upstream side of the Vosges, where the low-level convergence is greater, precipitation is enhanced in the REF run. On the

downstream side, precipitation is comparably lighter in the reference run. The flattening of the Vosges mountains also alters the precipitation over the Black Forest. Because less precipitation falls in the NOVOS simulation over flat terrain, the air in the NOVOS simulation is comparably moister and transported towards the Black Forest by westerly winds. Here, more precipitation falls in the NOVOS than in the REF run. This interaction between neighbouring low mountain ranges is relevant for quantitative precipitation forecasting and is in agreement with findings of Ehmele et al. (2015) for two neighboring islands.

4.2.4. Resolution of external parameters

The runs with smoothed external parameters (terrain height, land use, roughness length) have both positive and negative deviations of the total precipitation amount with respect to the REF run (Figure 4.3). In general, the deviations are larger on days with weak synoptic forcing than on days with strong synoptic forcing. Furthermore, there is no systematic relationship. Four days show a weak to moderate precipitation increase in the runs with smoothed external parameters (1 July 2009, 11 September 2013, 11 September 2011, 28 July 2013), whereas on the remaining two days both positive and negative deviations are simulated, depending how the surface parameters are smoothed. We use 30 June 2009 as an example of a weak forcing case, and 11 September 2013 from the strong forcing cases.

Weak forcing

On 30 June 2009, the difference plots reveal that increased and decreased precipitation occurs in clusters with approximately 10 km in diameter fairly close to each other (Figure 4.12). For all those three sensitivity runs, there is no clear behaviour as to where these spots are with respect to the underlying orography. However, in the to the west and north of the Black Forest, there is always less precipitation than in the REF run. The time series shows weak precipitation around 0600 UTC in all runs (Figure 4.13(a)). From 0930 UTC precipitation increases until the maximum around 1400 UTC. All sensitivity runs have slightly higher rain intensities around that time than the reference run. After a decline, precipitation increases again after 1800 UTC. CAPE and CIN values (Figure 4.13(b) and (c)) show opposing trends and have their maximum and minimum before precipitation increases, but in general show similar values for all runs. The most pronounced difference can be seen in the low-level wind convergence (Figure 4.13(d)). The smoother the terrain is, the weaker the wind convergence becomes. Consequently, the number of grid points with $w_{\text{diff}} > 0$ m s^{-1} and CAPE > 600 J kg^{-1} (Figure 4.13(e)) is also reduced with smoother terrain. Although a good agreement of this measure could be seen to the simulated precipitation in the NOBF and NOVOS sensitivity runs, a direct link is missing for the simulations with smoothed external parameters. From Figure 4.13(e), we would expect that precipitation decreases with smoother surface. But we see an increase for the EXT1000, no change for the EXT2800 and a decrease for the EXT7000 simulation. Similarly non-intuitive patterns can be seen on 1 July 2009 and 23 July 2013 (not shown).

Once deep convection is initiated on that day, it is probably only partly controlled by surface conditions during its mature or dissipation stage.

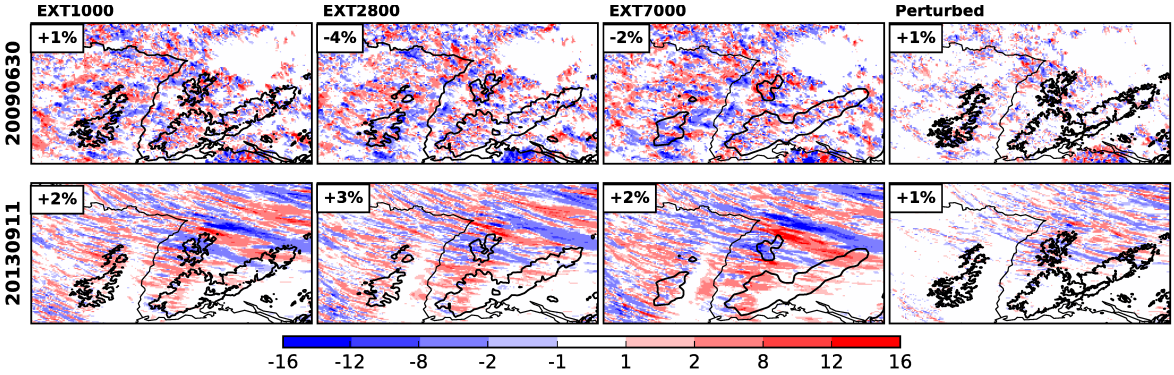

Fig. 4.12.: Difference plot of 24-h accumulated precipitation for the runs with smoothed surface parameters (EXT1000, EXT2800, EXT7000) and a temperature perturbed run on 30 June 2009 (top row) and 11 September 2013 (bottom row). Percentages indicate the deviation from the reference run in the seen part of the model domain.

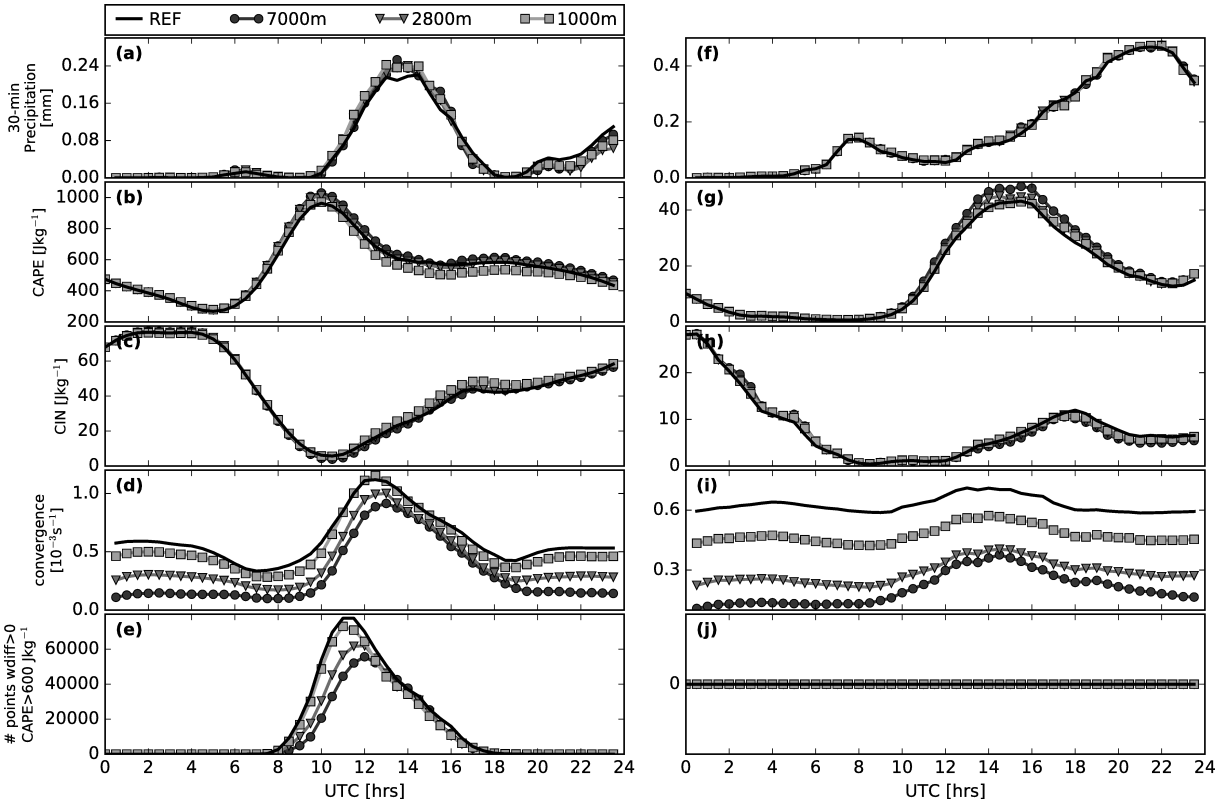

Fig. 4.13.: Domain-averaged precipitation, CAPE, CIN, low-level convergence and number of grid points with $w_{\mathrm{diff}} > 0\ \mathrm{m\,s^{-1}}$ and CAPE $> 600\ \mathrm{J\,kg^{-1}}$ for 30 June 2009 ((a)-(e)) and 11 September 2013 ((f)-(j)).

Strong forcing

For 11 September 2013, the time series reveal an almost identical rain evolution for all sensitivities (Figure 4.13(f)), which results in changes in total precipitation of less than 5% (Figure 4.3). CAPE and CIN values are, as discussed before, small on this day (Figure 4.13(g) and (h)). Subtle differences exist in CAPE and the low-level convergence becomes weaker with increasing surface smoothness (Figure 4.13(i)). The conditions are synoptically driven and the presence of mountains is sufficient to maintain precipitation as in the reference run. A similar pattern can be seen for 28 July 2013 and 11 July 2011 (not shown).

Both for the strong and the weak forcing cases we do not see a systematic relationship regarding precipitation, CAPE and the number of grid points with $w_{\text{diff}} > 0$ m s^{-1} and CAPE > 600 J kg^{-1} with respect to the resolution of the external parameters. Therefore, we wanted to test whether these results rather show random results than those linked to the underlying topography. We performed additional runs with standard orography in which we add random temperature fluctuations at model initialisation. We apply a gaussian perturbation with zero mean and a standard deviation of 0.01 K to the whole model domain and all levels. The total precipitation shows an increase of 3% on 30 June 2009 within area A (not shown). The precipitation patterns resemble very much the runs with smoothed surface parameters (Figure 4.12). The organisation of small cells and small spatial shifts can be seen both in the run with smoothed external parameters as well as the perturbed run. From these results, we computed probability density functions of 24-hr accumulated precipitation for these sensitivities and all regions of investigation (southern Germany, whole model domain, Black Forest and Vosges, not shown). They look almost identical and indicate that the runs with smoothed terrain show the same variability as runs with artificially created noise. For the strong forcing case on 11 September 2013, the effect of the temperature perturbation is weaker than those derived for the runs with smoothed external parameters. However, all four simulations have deviations smaller than 5% in total precipitation, as the deviations cancel out when averaged over a somewhat larger domain.

From these simulations we conclude that the resolution of external parameters has small effects on precipitation amount and timing for most cases. On days with weak synoptic forcing, the noise introduced by convection (i. e. transport by sound and gravity waves, discussed in 4.2.2) lies within the order of the magnitude of artificially created noise and precipitation totals can vary between -4% and +16%. Under strong forcing, the smoothing has an effect locally, but cancels out when looking at domain-averaged quantities. The lack of systematic effects demonstrate the need of more cases than the six cases analysed in this study. We plan to perform such sensitivity runs in the future. Moreover, the spread of these simulations indicates that smoothing the surface parameters might also be suitable to be used in operational ensembles.

4.2.5. Summary and conclusions

In this article we investigated the sensitivity of the simulated precipitation in the COSMO model to terrain forcing. We gathered an extensive set of high-resolution simulations with 500 m grid spacing spanning almost the whole of Germany and parts of eastern France. In the simulations, the terrain has been modified by either flattening the Vosges or Black Forest mountain ranges or by smoothing the terrain by interpolation of external parameters to 1 km, 2.8 km or 7 km. We analysed six cases and classified them as either strongly or weakly synoptically forced. The 500-m model provided a valuable analytical tool for understanding the physical processes that lead to the initiation of precipitation above complex terrain. From our study we conclude that the surface properties, which includes the terrain height, have an important impact on both the initiation of convection and the amount and location of precipitation. In all cases we see that the low-level wind convergence is crucial to initiate convection and that its strength determines the amount of precipitation. The main findings regarding our research question in the introduction are:

(1) Orography influences the initiation of deep convection in various ways. Our results show that mechanical lifting over or flow deviation around the mountains and wind changes induced by thermal instabilities are all important processes. These findings highlight the complex effects of mountains on the initiation of deep convection. For weakly synoptically-forced days, the onset of precipitation is delayed by around 2 hours on each of the days when the orography is flattened. There is a corresponding decrease of precipitation on two of the three weak-forcing days, which results from weaker low-level wind convergence in regions where the orography was removed. On the third weak-forcing day, a slight increase in precipitation is simulated because a different convection initiation mechanism is possible; in the region of the flattened Vosges mountains, thermal heating results in the formation of a weak low-pressure system, which induces changes in the wind direction, enhancing the low-level wind convergence. On the same day, more convection is initiated over the Black Forest where cold pool outflow from convection over the Vosges region flows over the flattened Black Forest region, and initiates convection here. Our results support the findings from Groenemeijer et al. (2009) and Bennett et al. (2011), who showed that under weak forcing, the terrain height often controls the initiation of deep convection. Interestingly, in the simulations with flattened Vosges, the deviations from the reference runs are smaller than in the corresponding runs with flattened Black Forest. We find that the removal of the Vosges and flattening of the land creates a secondary mechanism for convection initiation by allowing a larger expanse of convective rolls over the flattened land. Under strong synoptic forcing, there is a similar 2-hour delay in the onset of precipitation when the orography is flattened on one of the three days. On the other two days, the change in precipitation characteristics are small. Despite the sign of the feedback not being consistent across all simulations, we find a strong agreement between regions with reduced upward movement and less precipitation (both compared to the reference run). We confirm the findings from Langhans et al. (2011) and Barrett et al. (2015) for the flattened Black Forest and Vosges cases, as we also see a combination

of local and large-scale effects. Precipitation advected from the large-scale into the evaluation area is increased in the presence of mountains, rather than that mountains are crucial for initiation.

(2) We find that neighbouring mountain ranges are influenced strongly when strong synoptic conditions are present, as precipitation is reduced in the absence of mountains. As a result of reduced precipitation, the air is moister when transported with the mean wind. Downstream of the flattened area, at the adjacent mountain range, strong upward movements are evident and the additional moisture results in increased precipitation. This suggests that representing the orography well allows the correct prediction of moisture transport and as a result which regions receive the heaviest precipitation. This can be of great importance for accurately forecasting in which river catchments the precipitation falls. Other more complex interactions between the mountainous regions are possible. For example, under weak synoptic conditions, cold-pool outflow from one mountainous region induces stronger low-level winds over the flattened neighbouring region, which then acts as a trigger mechanism to initiate deep convection.

(3) When smoothing the surface parameters, we find that the effect of individual valleys on the daily accumulated precipitation is small. Nevertheless, we see that the low-level wind convergence decreases with smoother surface parameters on all days. A limited sensitivity of precipitation to smoothing the orography was also found by Schumacher et al. (2015), who showed that when the terrain is smoothed, even minor precipitation bands and small-scale circulations remain. Also, Kirshbaum and Durran (2005) found in semi-idealised simulations that precipitation over smoothed orography is similar to the results produced for roughened terrain, especially when precipitation was more randomly distributed (which resembles our weak forcing cases). Despite the indication that the resolution of external parameters is of minor importance for the initiation of convection, when predicting the exact location of clouds down to a scale of a few kilometres, i.e. for flood risk management, the resolution of external parameters may be of greater importance. Horizontal differences of a few kilometres can make the difference between a flash flood and no flash flood (e. g. Burt, 2005). To determine how large the changes from smoothing the orography are, compared to chaotic changes to the location and intensity of precipitation, we compared our simulations for two days to those derived from introducing a random temperature perturbation at model initialisation. We see that the variability of precipitation by gradually smoothing out orographic features is on the same order as artificially created noise. Therefore, we propose that using coarser external data as an ensemble member could be used in operational ensembles at weather services. Our results show a need for more research regarding the effects of small-scale terrain features, since the analysed six cases were not enough to properly quantify the effects on precipitation.

(4) We find that the impacts of the terrain on the amount and timing of precipitation are generally larger when the synoptic forcing is weak. This points towards the important role of surface and boundary layer processes for convection initiation in weakly-forced weather conditions. In return this means that precipitation forecasting for high-impact weather should start by capturing large-scale synoptic features, like fronts, correctly.

From this study we see that in contrast to the operationally used setup, our model setup with a horizontal grid spacing of 500 m allows to resolve thermally induced roll-vortices over the flattened Vosges region with a width of about 3 km. This is in agreement with findings from Schwitalla et al. (2008), who showed that increasing the resolution up to 500 m produces fewer errors in quantitative precipitation forecasting. Based on this result, we recommend that models used in operational mode should account for the deficiencies introduced by differences in the resolution, for example by applying stochastic perturbations. There is a need to further investigate the physical mechanisms behind the inconsistent precipitation response, that we observe in simulations with removed and smoothed orography. Also evaluating the relative importance of surface properties compared to other uncertainties, for example soil moisture and aerosol concentrations, would be desirable. These are both topics we can address with our high-resolution modelling setup and are the subject of ongoing work.

4.3. Soil moisture

Soil moisture affects precipitation by changing the surface energy balance, which then alters temperature and humidity within the boundary layer. Within this chapter, the effects of soil moisture biases, and soil moisture gradients will be investigated. The runs with changed soil moisture show precipitation amounts ranging between 1-5.5x10^{11} litres on weak forcing days and 5.5-9.8x10^{11} litres on strong forcing days (Figure 4.14). Weak forcing days show changes up to 17%, compared to the reference run, with an

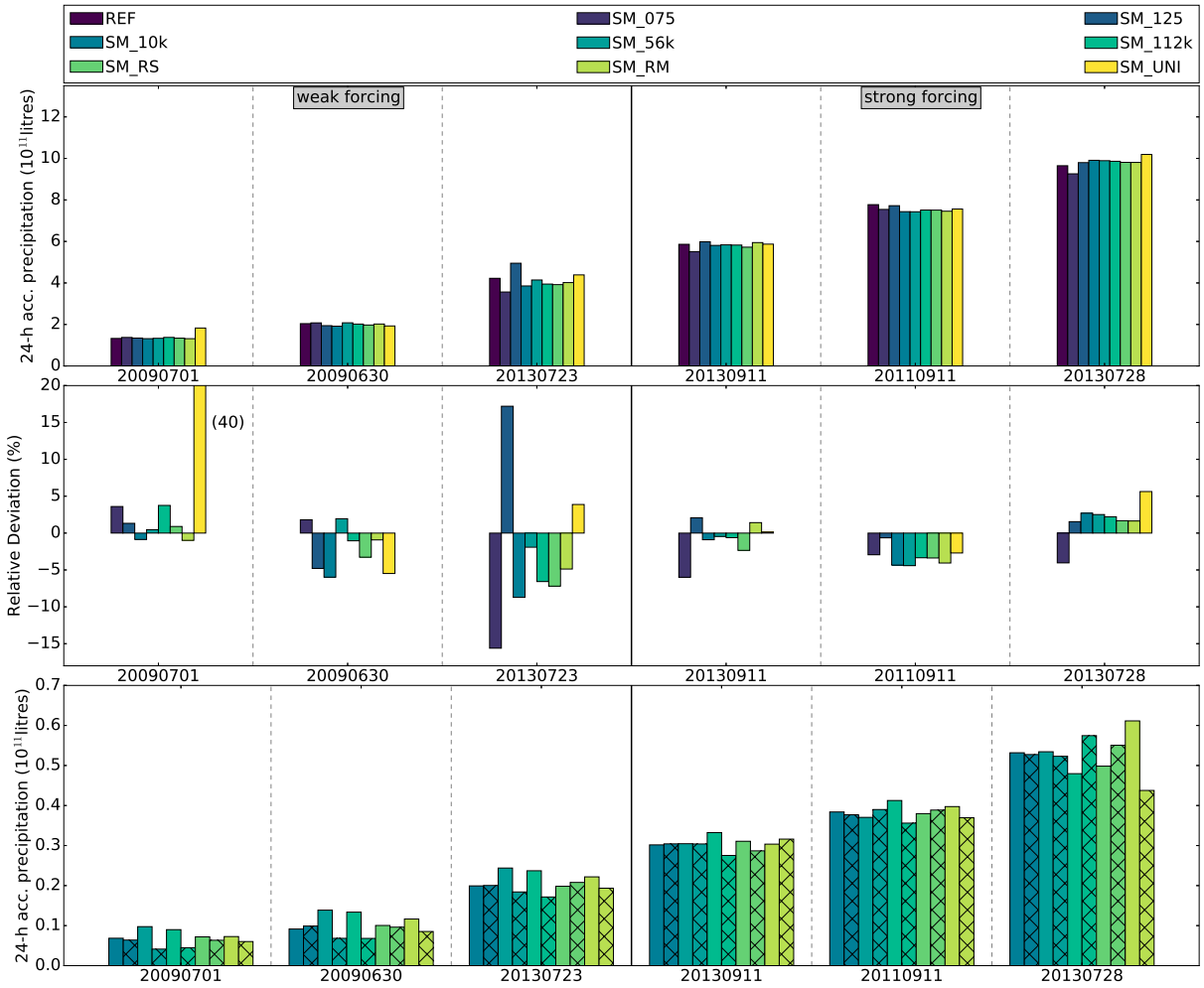

Fig. 4.14.: Summary of the 24-h precipitation totals in evaluation area A. Top: 24-h precipitation for the cases with weak (left) and strong (right) synoptic forcing. Middle: Relative deviation of the precipitation amounts from the sensitivity runs to the reference run. Bottom: 24-h precipitation separated for dry (non-hatched) and wet (hatched) patches.

exception of the uniform simulation (SM_UNI) on 1 July 2009, where an increase of 40% is modeled. In contrast, simulations with strong forcing conditions show variations around 5% and lower. The sign of the soil moisture–precipitation feedback is not consistent within one set of simulations, i.e. runs with decreased soil moisture (SM_075) can show more or less precipitation than in the reference run,

Tab. 4.2.: Precipitation deviation compared to the REF simulation in the run with reduced (SM_075) and enhanced (SM_125) soil moisture in the whole domain.

Type	20090701	20090630	20130723	20110911	20130911	20130728
SM_075	-6%	-5%	-13%	-6%	-5%	-11%
SM_125	+7%	+3%	+11%	+2%	-1%	-6%

depending on the individual case. On three out of six days, a decrease in precipitation is modeled for the run with decreased soil moisture, and an increase for the run with increased soil moisture. On two days, 1 July 2009 and 11 September 2011, the same sign of precipitation change is simulated when soil moisture is increased or decreased compared to the reference simulation. The last day (30 June 2009) shows increased precipitation with decreased soil moisture and decreased precipitation with increased soil moisture. For the simulations with chess board (SM_10k, SM_56k, SM_112k) and random (SM_RS, SM_RM) patterns, no systematic trend can be observed in the precipitation response. However, the spatially accumulated precipitation on weak forcing days show similar or more precipitation over the dry patches (Figure 4.14, bottom). It is suspected that thermal forcing is more important over the dry than over the wet patches and this will be analyzed further. For most of the strong forcing cases, there is also more precipitation over the dry than over the wet patches (Figure 4.14). At this point it needs to be emphasized that these results are for evaluation area A. Looking at the whole domain, a positive soil moisture – precipitation feedback can be seen for the bias simulations in all weak forcing cases. Table 4.2 lists the relative deviations compared to the reference simulation for the whole domain. Because of this pronounced difference, there will be a separate analysis of the underlying causes of preciptiation change for the weak forcing bias simulations within evaluation area A and the domain. In contrast, the strong forcing simulations show similar deviations in evaluation area A and in the whole domain. This indicates that the large-scale situation is more relevant on those days than the available moisture in the soil and hence the results will be discussed only for evaluation area A. The chess, random and uniform simulations show a similar behavior, independent of the analyzed domain (not shown).

The area that experiences precipitation is very similar (differences $<2\%$ compared to the reference case) for all simulations (not shown) and can hence not explain any variations. Also, maximum precipitation amounts cannot clarify the relative deviations from the reference run in most cases (not shown). Only in the SM_125 and SM_UNI simulations, a positive relative deviation (Figure 4.14, middle) always goes along with a higher maximum precipitation amount than in the reference simulation (not shown). However, the cumulative probability density function of the accumulated precipitation reveals that the 24-h precipitation distribution differs between the simulations (Figure 4.15), especially for weak forcing cases. Whereas the average precipitation amounts are similar, the median changes. On 1 July 2009, the uniform simulation shows the greatest shift towards larger precipitation amounts, followed by the SM_075, whereas the SM_112k and SM_RM simulations have the lowest median. On 30 June 2009, the

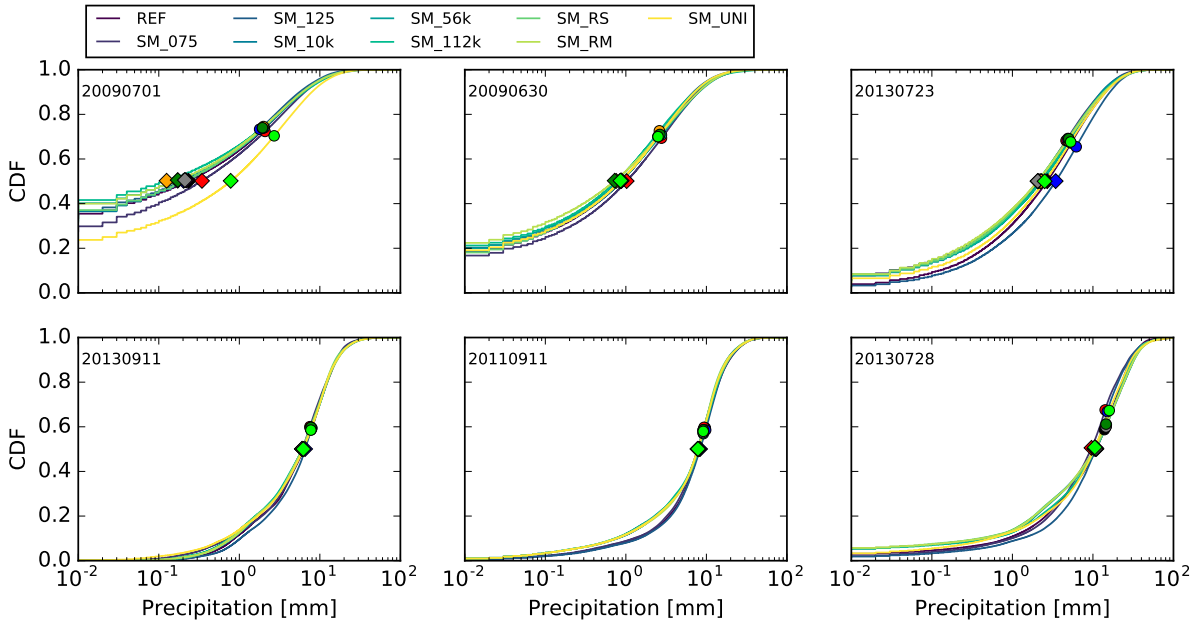

Fig. 4.15.: Cumulative probability density (CDF) function of daily accumulated precipitation for the weak forcing cases (top) and strong forcing cases (bottom). Filled circles indicate the average, filled diamonds the median for each simulation.

SM_075 simulation shows a shift towards more grid points with more precipitation. On 23 July 2013, there is a precipitation shift towards larger amounts, compared to the other two weak forcing days. Here, the SM_125 simulation shows the highest frequency of strong precipitation, which can explain the large precipitation amounts. The strong forcing days are dominated by more intense precipitation, and their mean and median do not differ a lot. Although the area with precipitation hardly changes, the spatial distribution of precipitation shows small-scale discrepancies. For example, Figure 4.16 shows the 24-hr accumulated precipitation for 1 July 2009. The bias simulations show locally varying precipitation changes compared to the reference simulation, e.g. less precipitation in the SM_075 run in the northern part of the domain. The chess board simulations show a slightly higher degree of organization compared to the reference case, especially in the SM_10k simulation. This can also be seen for the simulations with random patterns, e.g. over central Germany. The uniform simulation shows increased precipitation amounts compared to the reference simulation, especially at the eastern boundary. To better understand the precipitation responses to modified soil moisture, time series of convection-related variables are now analyzed.

4.3.1. Uniform experiments

The main purpose of introducing a constant soil moisture field is to eliminate effects induced by horizontal differential heating, and to determine the effects introduced by terrain structures. However, a constant

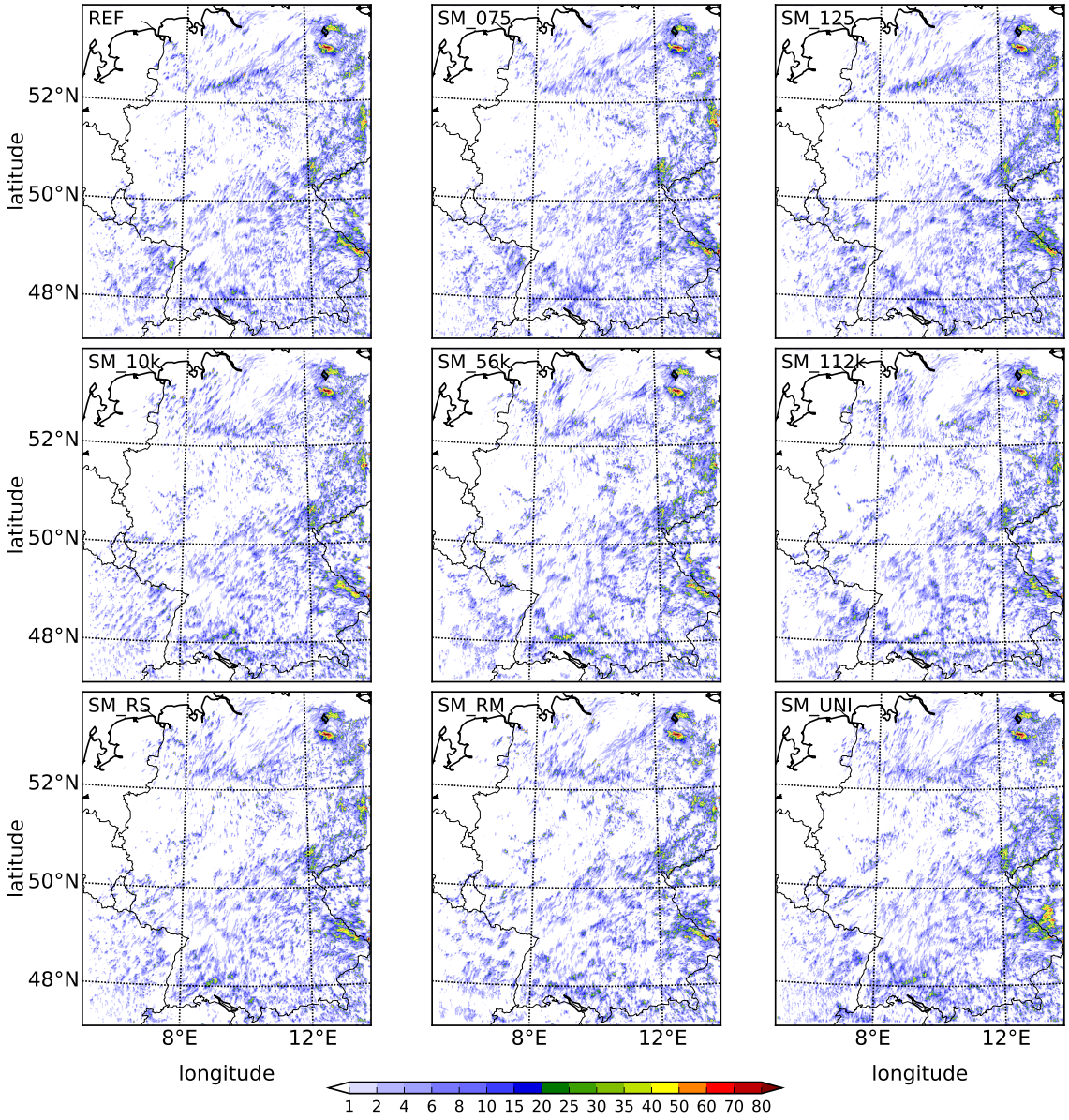

Fig. 4.16.: 24-hr accumulated precipitation for 1 July 2009.

soil moisture does not imply a constant land cover, meaning that horizontal gradients in volumetric soil moisture can occur due to differences in the soil or vegetation type.

On 1 July 2009, precipitation occurs predominantly over the mountain crests in the reference and uniform simulations between 1000–1300 UTC (not shown). Pronounced differences only become visible thereafter, when much stronger rain intensities are achieved in the uniform simulation (Figure 4.17(a)), but when the location of precipitation is likewise similar in both simulations (not shown). The time series shows enhanced specific humidity in the uniform simulation compared to the reference simulation (Figure 4.17(b)). The higher specific humidity can be explained as follows: In the reference run the probability density function of initial relative soil moisture is almost symmetrically distributed around the mean

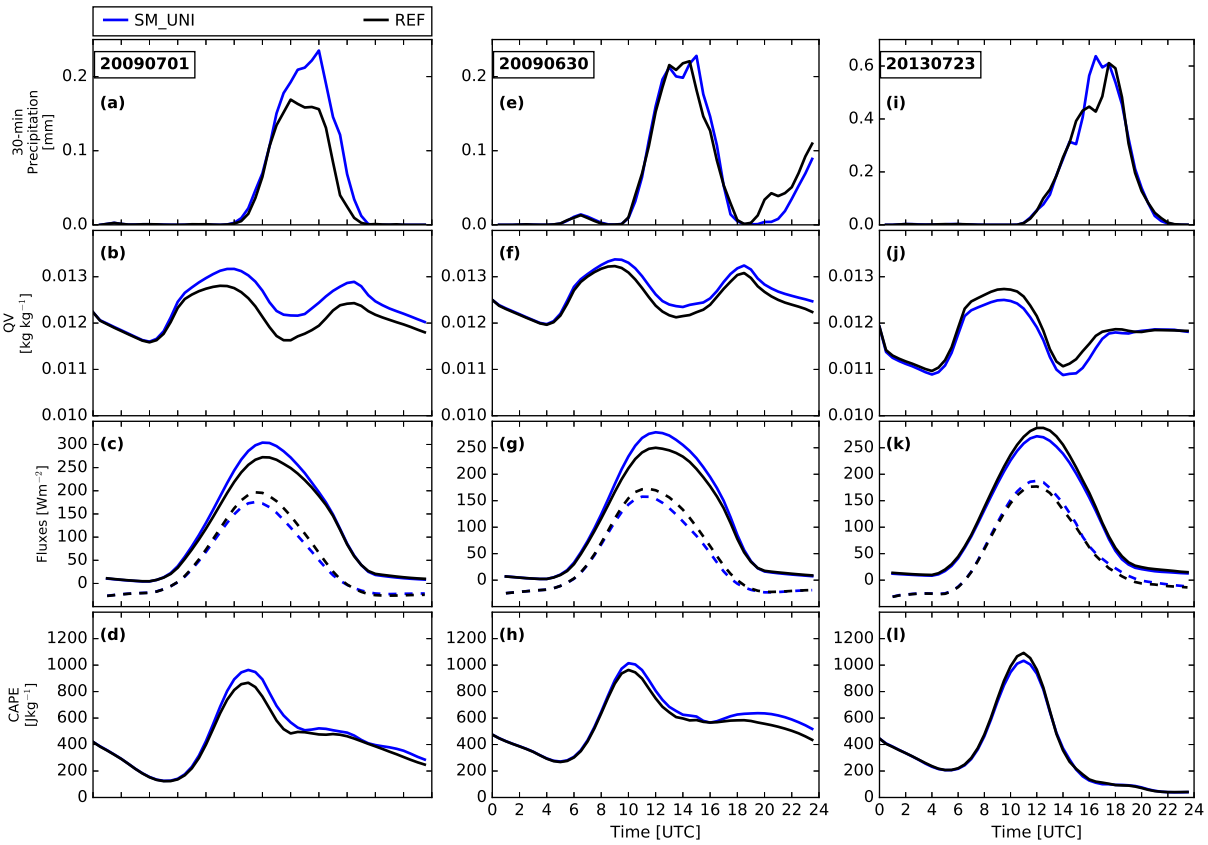

Fig. 4.17.: Half-hourly averaged precipitation over evaluation area A, 2-m specific humidity (QV), latent (solid) and sensible (dashed) heat flux and convective available potential energy (CAPE) for 1 July 2009 ((a)–(d)), 30 June 2009 ((e)–(h)) and 23 July 2013 ((i)–(l)).

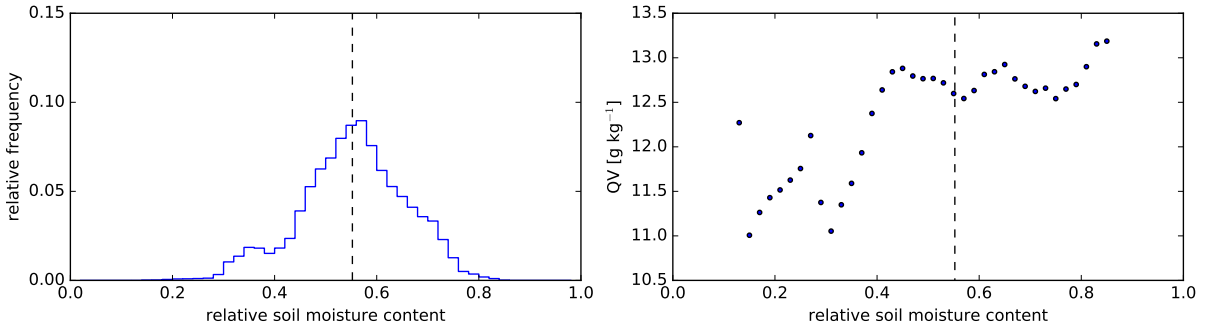

Fig. 4.18.: Left: Probability density function of the initial relative soil moisture content in evaluation area A for 1 July 2009. Right: simulated initial soil moisture and averaged specific humidity at 0800 UTC. The black lines denote the mean soil moisture content.

(Figure 4.18(left)). However, the relation between specific moisture at 0800 UTC and initial soil moisture content, shows a strong susceptibility for soil moisture values lower than 40% (Figure 4.18(right)). This is the regime where evapotranspiration is limited by the availability of moisture in the ground. For the uniform simulation, all soil moisture values are set to the mean value of 55%. Thus, points that were

below the mean in the reference simulation, and which are increased for the uniform simulation, will contribute to an increase in specific humidity. Those points that were above the mean in the reference simulation will not affect the specific humidity much in the uniform simulation, despite a decrease in the relative water content. The specific humidity is determined by the latent heat flux, which increases in the uniform simulation compared to the reference simulation (Figure 4.17(c)). Most likely, this small increased humidity is not responsible for triggering precipitation, but rather only enhances precipitation, by increasing CAPE (Figure 4.17(d)) and increasing the amount of precipitable water (not shown), which would be in accordance with the findings that the location of precipitation is similar (Figure 4.16).

On 30 June 2009, the evolution of precipitation is similar between the reference and uniform simulation until 1300 UTC. After 1500 UTC the uniform simulation dominates and after 2000 UTC the reference simulation dominates. After 2000 UTC, there is one location in the reference simulation, where it has not been precipitating before and CAPE values have build up to more than 1800 $\mathrm{J\,kg^{-1}}$ (not shown). The emerging precipitating cells hence show very high precipitation amounts and smaller cells even organize to a more complex system of about 30×30 km. This particular system can explain the total precipitation difference between the reference and uniform simulation. In contrast, CAPE did not build up the same way in the uniform simulation, resulting in less precipitation at this particular location. On 23 July 2013, the average soil moisture content is much lower (38%) and the probability density function narrower (not shown). The relationship between specific humidity and soil moisture is similar as on 1 July 2009 (not shown), but there is a shift towards a regime in which both the increase and decrease of specific humidity impacts the latent heat flux almost equally, resulting in a similar temporal evolution (Figure 4.17(k)). The reduction in specific humidity (Figure 4.17(j)) results from a similar or lower latent heat flux in the uniform compared to the reference simulation and a half-hour earlier increase in the sensible heat flux (Figure 4.17(k)). Therefore, CAPE is on average higher in the reference than the uniform simulation before precipitation onset (Figure 4.17(l)). Most likely the decrease in the precipitation rate at 1430 UTC in the uniform run is a result of the less favourable conditions for convection. However, the precipitation increases in the uniform simulation later on and it looks that one particular cell is responsible for a change in this signal. This was checked by computing domain averages of the convection-related parameters for everything but the location of the intense cell and it turns out that precipitation in the SM_UNI simulation is then equal or lower than in the reference simulation (not shown). The reason that this cell becomes so active and intense is that over this location strong CAPE and high low-level wind convergence exist (not shown).

On two of the strong forcing days (11 September 2013 and 11 September 2011), the change in daily precipitation by a homogeneous soil moisture field is small (Figure 4.14). Similarly, the time series of precipitation shows only very small differences between the SM_UNI and reference simulation (Figure 4.19(a) and (d)), despite an increase in the latent heat flux (Figure 4.19(c)) and the specific humidity (Figure 4.19(b)) on 11 September 2011. More prominent differences are visible on 28 July 2013 (Figure 4.19(g)). Until 1800 UTC, the latent heat flux is higher in the uniform than in the reference simula-

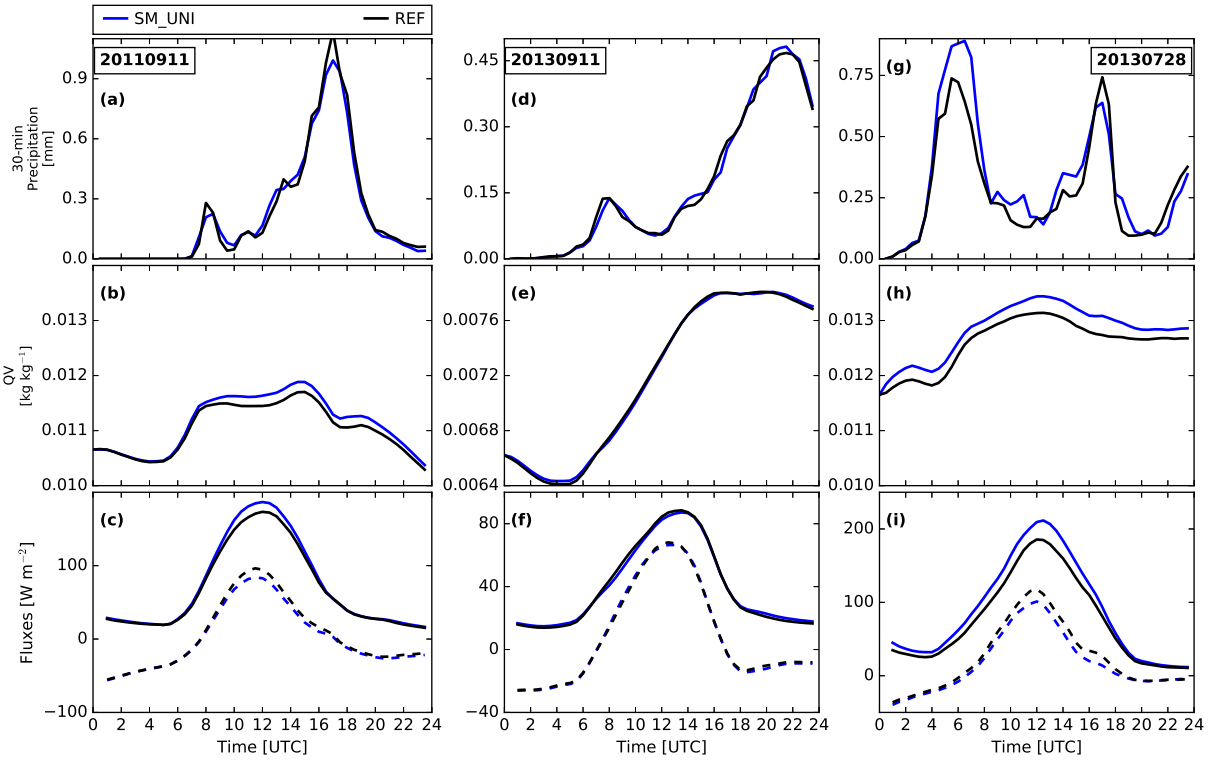

Fig. 4.19.: Half-hourly averaged precipitation over evaluation area A, 2-m specific humidity (QV), latent (solid) and sensible (dashed) heat flux for 11 September 2011 ((a)–(c)), 11 September 2013 ((d)–(f)) and 28 July 2013 ((g)–(i)).

tion (Figure 4.19(i)) resulting in higher specific humidity than in the reference run (Figure 4.19(h)). At 0600 UTC, when precipitation is higher in the uniform than the reference simulation, an intense precipitation cell passes an area, which is now 37% moister than in the reference run (Figure 4.20). This extra moisture leads to the intensification of precipitation over this area.

4.3.2. Bias experiments

Weak forcing

The time series of domain-averaged precipitation reveals a diurnal cycle with a precipitation maximum in the afternoon on 1 July 2009 (Figure 4.21(a)). The timing between the SM_075, SM_125 and the reference simulation is very similar. All convection-related variables displayed in Figure 4.21 show a systematic evolution: As expected, the soil moisture correlates positively with the specific humidity (QV) near the surface (Figure 4.21(b)). After sunrise, QV increases in all simulations until precipitation onset and shows a second maximum when precipitation stops. Also θ_e (not shown), follows this evolution. The ratio between sensible and latent heat flux, the Bowen ratio β (Figure 4.21(d)), can become greater than 1 during daytime hours (6–18 UTC). This is the time when the sensible heat flux dominates. In these simulations, the Bowen ratio will only become greater 1 in the SM_075 simulation, but not in

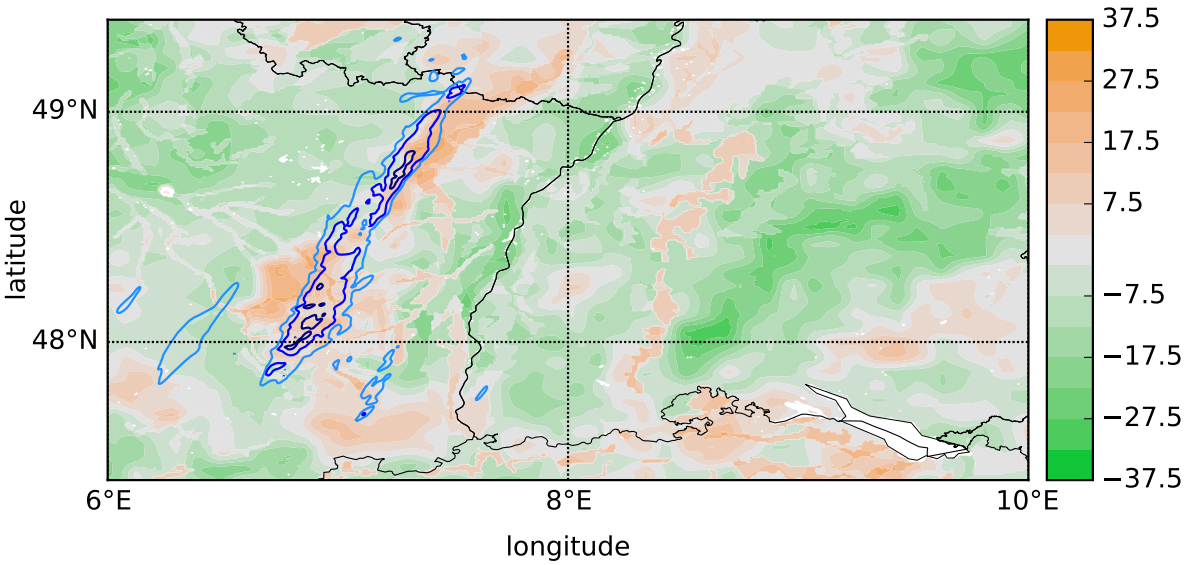

Fig. 4.20.: Filled contours show changes of initial soil moisture in percentage points that were applied to the reference simulation in order to obtain the uniform simulation. Blue contour lines show from light to dark the 5, 10 and 20 mm precipitation amounts for 28 July 2013 at 0600 UTC.

the reference or the SM_125 simulation. Negative values of β indicate that the sensible heat flux is reversed, and directed towards the ground, like it is during night when the ground is colder than the surrounding air. During daytime, the simulation with higher soil moisture content shows lower 2-m temperature (Figure 4.21(c)) than the reference simulation, as more of the available energy is partitioned into latent heat. Vice versa, the 2-m temperature in the runs with drier soil is higher than in the reference run, because of a higher sensible heat flux (Figure 4.21(c)). Higher 2-m specific humidity and lower temperatures in the SM_125 simulation, compared to the drier REF and SM_075 run, result in a lower lifting condensation level and in these cases also in a lower level of free convection (both not shown). As a result, domain averaged CAPE is higher in the SM_125 simulations than in the reference runs (Figure 4.21(e)), given that the atmospheric stability is the same in the middle and upper troposphere. The variance of the sensible heat flux is highest in the SM_075 simulation (not shown), followed by the reference and SM_125 simulation. In the SM_075 simulation, this induces horizontal thermal gradients at the surface and promotes horizontal transport of air. Consequently, the low-level wind convergence is stronger in the SM_075 simulation, than in the REF and SM_125 simulation (Figure 4.21(f)).

The precipitation response of the reference and the SM_125 simulations are similar on 1 July 2009 (Figure 4.21(a)). Despite the weaker low-level triggering, precipitation amounts are comparable to the reference simulations, which is due to increased CAPE in the SM_125 compared to the reference simulation (Figure 4.21(e)). In contrast, the SM_075 simulation on 1 July 2009 shows a little more precipitation after initiation of deep convection, than the reference run. Here, the surface triggering is stronger than in the reference simulation, but smaller CAPE values only lead to small changes in the precipitation. On

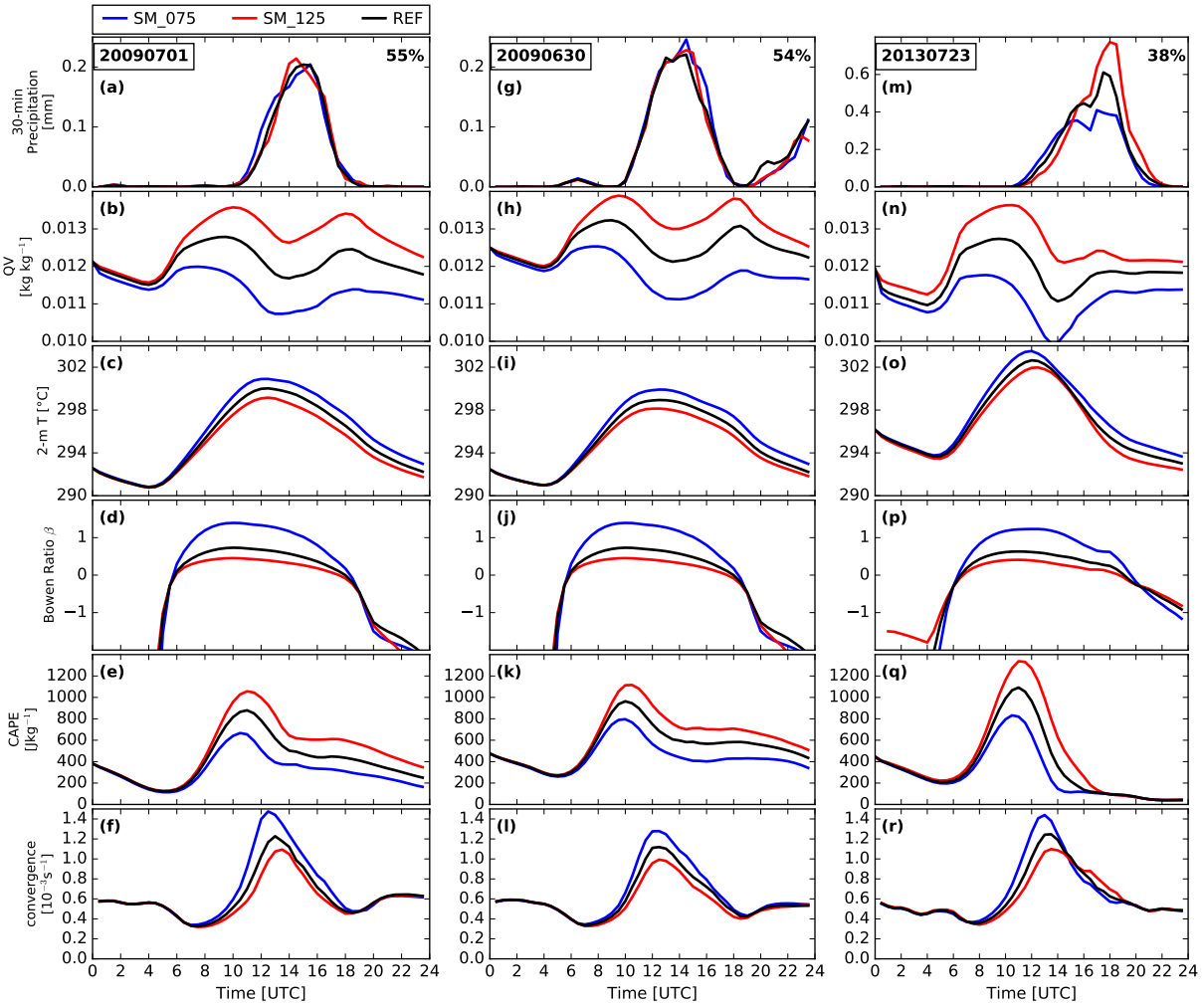

Fig. 4.21.: Half-hourly averaged precipitation over evaluation area A, 2-m specific humidity (QV), Bowen ratio (β), convective available potential energy (CAPE) and low-level wind convergence for 1 July 2009 ((a)–(f)), 30 June 2009 ((g)–(l)) and 23 July 2013 ((m)–(r)). Numbers in the top right corner of the first row indicate the relative water content at model initialization for the reference simulation.

30 June 2009, there are no differences regarding the precipitation time series between the SM_075 and the reference run between 1000–1200 UTC, but only thereafter when first the SM_075 shows increased precipitation amounts (1400–1800 UTC) and then the reference run (1900–2300 UTC). The temporal evolution of convection-related parameters is similar as on 1 July 2009. On 23 July 2013, the precipitation responses between modified soil moisture runs and the reference run look different than on the other two days. Although the timing of precipitation initiation is similar, the intensity between 1500-1900 UTC is strongest in the SM_075 run and weakest in the SM_125 simulations (Figure 4.21(m)). Despite the strong surface triggering in the SM_075 simulations compared to the reference run, and therefore a stronger precipitation increase after convection initiation, low CAPE values inhibit intense precipitation after 1500 UTC. In return, the SM_125 simulations show less precipitation than the reference run after

convection initiation. CAPE can therefore build up and this favors convection in the following hours. CIN values are similar in all three simulations (not shown).

The variation of susceptibility to different soil moisture conditions between the three weak forcing days (i.e. strong variations between dry and wet simulations on 23 July 2013, but little on 30 June and 1 July 2009) could again be associated with the overall soil moisture content. The relative water content is only 38% on 23 July 2013, but about 55% on the other two days. Barthlott et al. (2011b) have shown in a numerical study for a day with high volumetric water content, that there is only a high sensitivity regarding soil moisture to daily precipitation when significantly lowering the moisture content. In case of high soil moisture, evapotranspiration is controlled by the available net radiation. On 23 July 2013, however, the availability of soil moisture controls evaporation, resulting in a strong response of precipitation to changes in the initial soil moisture.

Since the conditions at the surface affect the distribution of moisture and heat within the lower troposphere, they also influence cloud formation and dynamics. On all days, the location of clouds is similar between the bias simulation and the reference simulation (not shown). The timing of clouds forming, which is deduced from the liquid water path, follows the time series for precipitation (not shown), indicating that clouds form at similar times as in the reference case. However, the vertical structures show disparities. Figure 4.22 shows the domain-averaged profiles of different hydrometeors averaged between 0800–1800 UTC. On 1 July 2009, the cloud water content shows that the cloud base is highest in the SM_075 and lowest in the SM_125 simulation (Figure 4.22(a)). This can be explained by higher temperature and lower specific humidity at the surface in the SM_075 compared to the SM_125 run, resulting in a higher lifting condensation level and more mixing in the boundary layer, which is deduced from higher updraft values in the SM_075 simulation (Figure 4.22(f)). The rain content is highest in the SM_075 simulation (Figure 4.22(b)). This could be a result of strong surface triggering, which brings moisture into the altitudes between 2–4 km. However, the rain content near the surface is similar, indicating that strong evaporation occurs between 1–3 km height. Around 8 km, the maximum of graupel is likewise higher in the SM_075 simulation (Figure 4.22(d)), compared to the REF and SM_125. In even higher altitudes the ice content values are lowest in the SM_075 compared to the REF and SM_125 simulation (Figure 4.22(c)). It could be that the available moisture in the SM_075 simulation has condensated at lower altitudes, resulting in less ice. In general, all hydrometeors have their maximum at similar levels in all simulations, except the cloud water content. On 30 June 2009 and 23 July 2013, differences to 1 July 2009 are visible in the cloud water, rain water and ice content, as all three simulations show a similar behavior with less pronounced differences. An exception is the graupel content on 23 July 2013, where the SM_075 shows less graupel than the other two simulations.

In contrast to the results previously described for evaluation area A, results in the whole domain show a positive soil moisture–precipitation feedback for all weak forcing cases, when introducing a soil moisture bias (Table 4.2). This response already indicates that the underlying terrain, in addition to the soil moisture, affects precipitation under weak forcing. The evolution of precipitation (Figure 4.23) is similar to

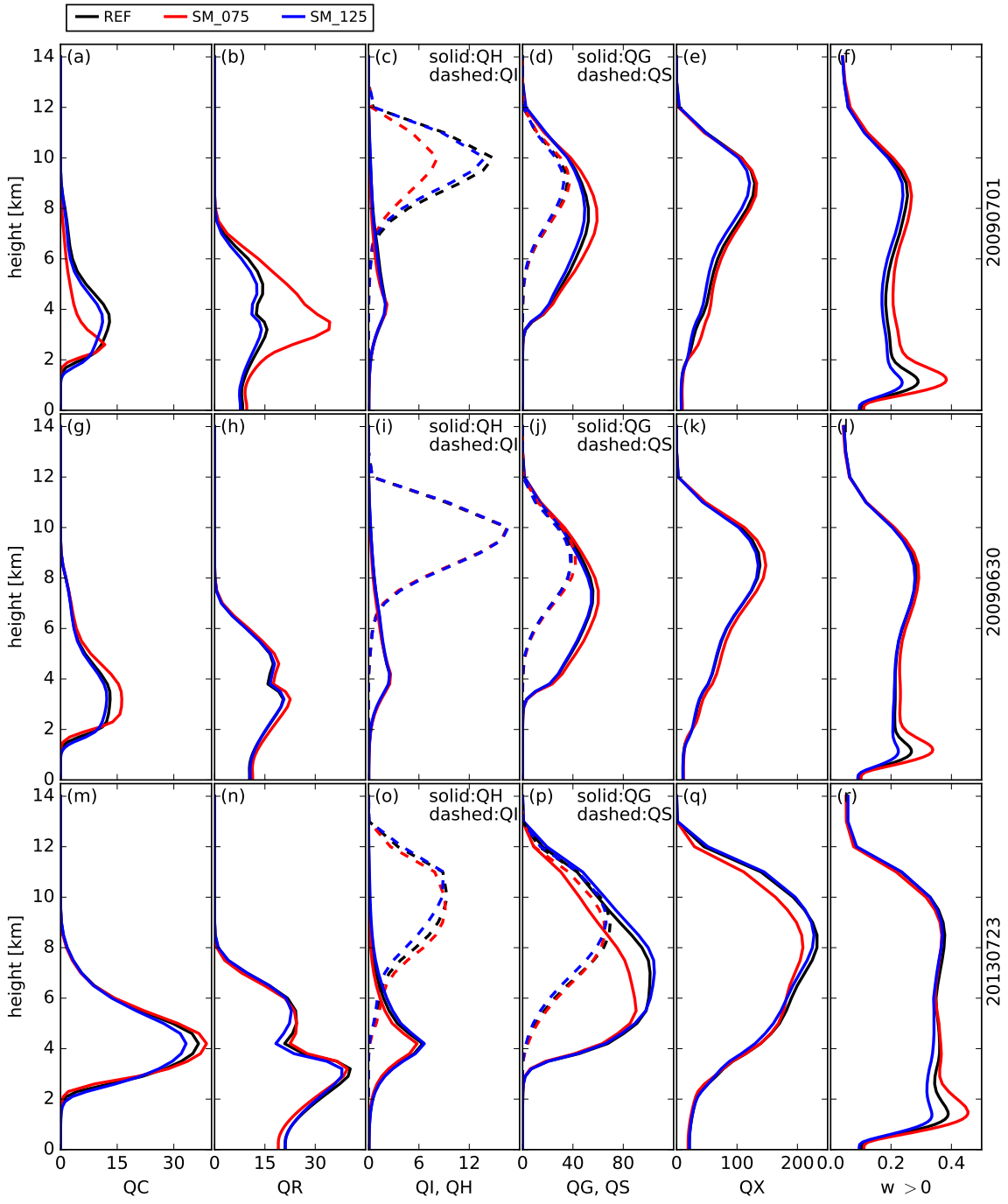

Fig. 4.22.: Domain-averaged cloud water (QC), rain (QR), ice (QI), hail (QH), graupel (QG), snow (QS) and total condensate (QX) in mg kg^{-1}, as well as updraft velocity (in ms^{-1}) between 0800–1900 UTC for 1 July 2009 (top row), 30 June 2009 (middle row) and 23 July 2013 (bottom row).

the one for evaluation area A (Figure 4.21). However, on 1 July 2009 the maximum precipitation amounts and timing differ (Figure 4.23(a)). The SM_075 simulation shows its maximum at 1200 UTC. Precipi-

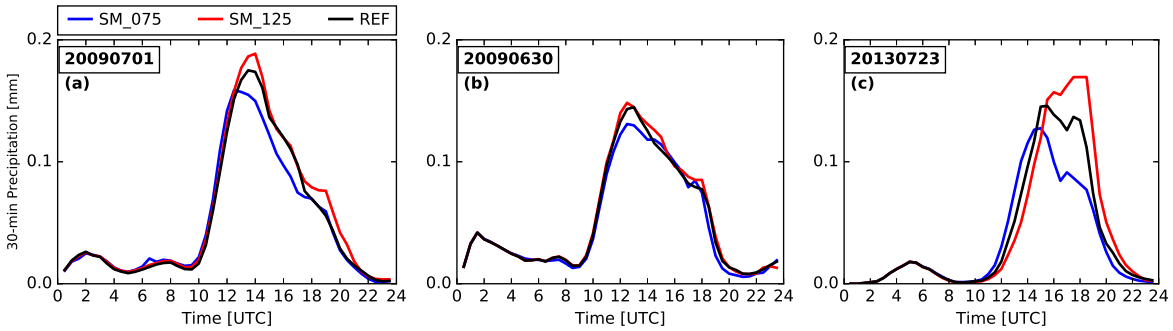

Fig. 4.23.: Half-hourly averaged precipitation for (a) 1 July 2009, (b) 30 June 2009 and (c) 23 July 2013 for the full domain.

tation continues in the REF and SM_125 simulation, possibly because of higher CAPE (not shown), and reaches its maximum around 1300 UTC. This determines the overall precipitation amount, especially because the rate at which precipitation declines is similar. On 30 June 2009, the timing is similar in all regards, but the maximum amounts are highest in the SM_125 and lowest in the SM_075 simulations (Figure 4.23(b)). On 23 July 2013, the time series of precipitation in the whole domain is similar as for evaluation area A and hence it is omitted from the detailed analysis. As pointed out earlier, the initial soil moisture content may impact the susceptibility of precipitation. This is indeed in agreement with the findings for the weak forcing cases on 1 July and 30 June 2009, when the relative water content is in the whole domain about 5–10% lower than in evaluation area A. By that the soil moisture is below a critical threshold, under which the evaporation is determined by the initial soil moisture content.

Strong forcing

On 11 September 2013, the precipitation evolution is similar between the SM_125 and reference run (Figure 4.24(a)). The SM_075 simulation only shows lower values between 1600–1900 UTC. Interestingly, the specific humidity is much lower on this day than on the other two days (Figure 4.24(b)). This can be explained by a very weak response of the surface to solar heating, as the net radiation is lower than 300 W m^{-2} (not shown), and moisture may even be influenced by advection of dry air into the evaluation domain. In the SM_075 simulation, the level of free convection is on average 200 m higher than in the other two simulations (not shown). This is possibly due to an even drier soil in the SM_075 run, which leads to a higher surface temperature, thereby increasing the LFC. On 11 September 2011, the precipitation response to soil moisture perturbations is marginal (Figure 4.24(d)). This indicates that large-scale processes dominate, which would be in agreement with small CAPE values and weak low-level wind convergence (both not shown). On 28 July 2013, the evolution of precipitation in SM_075 and SM_125 shows increased maximum precipitation than the reference run at 0600 UTC, but reduced precipitation amounts at 1800 UTC (Figure 4.24(f)). This can be linked back to the amount of precipitable water

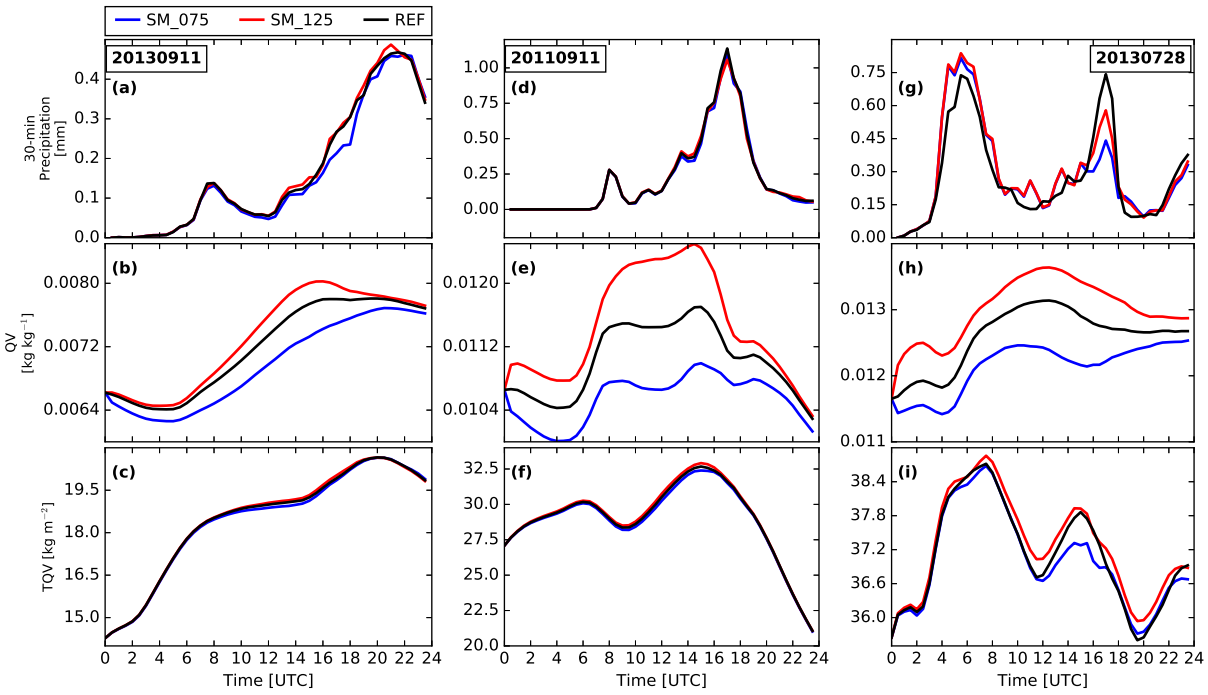

Fig. 4.24.: Domain averaged precipitation, 2-m specific humidity and precipitable water (TQV) on 11 September 2013 ((a)–(c)), 11 September 2011 ((d)–(f)) and 28 July 2013 ((g)–(i)).

available in the atmosphere (Figure 4.24(i)), which follows a similar trend. CAPE and the low-level wind convergence are also small, and the LFC is similar between the SM_075 and SM_125 (not shown).

The profiles of domain averaged cloud variables show very small differences in all hydrometeors on 11 September 2013 (Figure 4.25(a)–(e)) as well as on 11 September 2011 (Figure 4.25(f)–(j)) . On the first day, clouds are very shallow, possibly due to very low values of specific humidity (Figure 4.24(b)). On 28 July 2013, more pronounced differences exist between the simulations (Figure 4.25(k)–(o)). The vertical extent is highest in the reference simulation, as the cloud top is higher than in the SM_125 and SM_075 simulation, and in addition the reference run shows the largest amounts of condensate, because of increased amounts of cloud water, cloud ice and graupel.

4.3.3. Chessboard experiments

Weak forcing

The chessboard experiments show no clear systematic reagarding the precipitation totals in evaluation area A (Figure 4.14). However, the SM_56k and SM_112k show a distinct sign of more precipitation over the dry patches (Figure 4.14(bottom)). On 1 July 2009, the timing of domain averaged precipitation is very similar over both the dry and the wet patches. However, when looking at the spatial pattern of precipitation, a few small cells (25 km^2) can be seen, which are present about 30-minutes earlier over the dry patch than at the corresponding location in the reference run (not shown). In the SM_10k simulations,

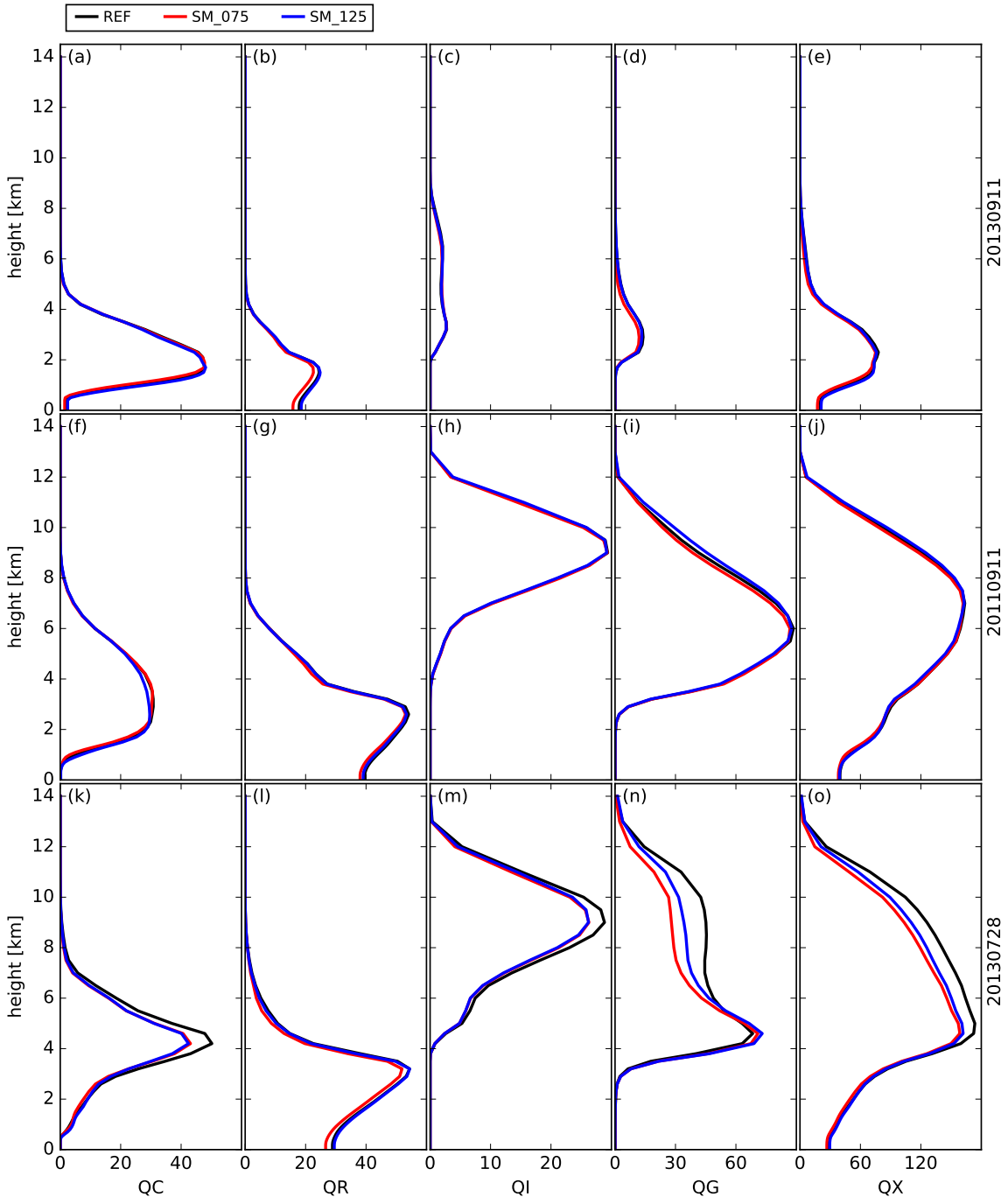

Fig. 4.25.: Domain-averaged cloud water (QC), rain (QR), ice (QI), graupel (QG) and total condensate (QX; note: this also includes snow and hail) in mg kg^{-1} between 0800–1900 UTC for 11 September 2013 (top row), 11 September 2011 (middle row) and 28 July 2013 (bottom row).

both the 24-hr accumulated precipitation (Figure 4.14), as well as the temporal evolution are similar over the wet and dry patches (Figure 4.26(a)), which indicates that the patch size is probably too small to

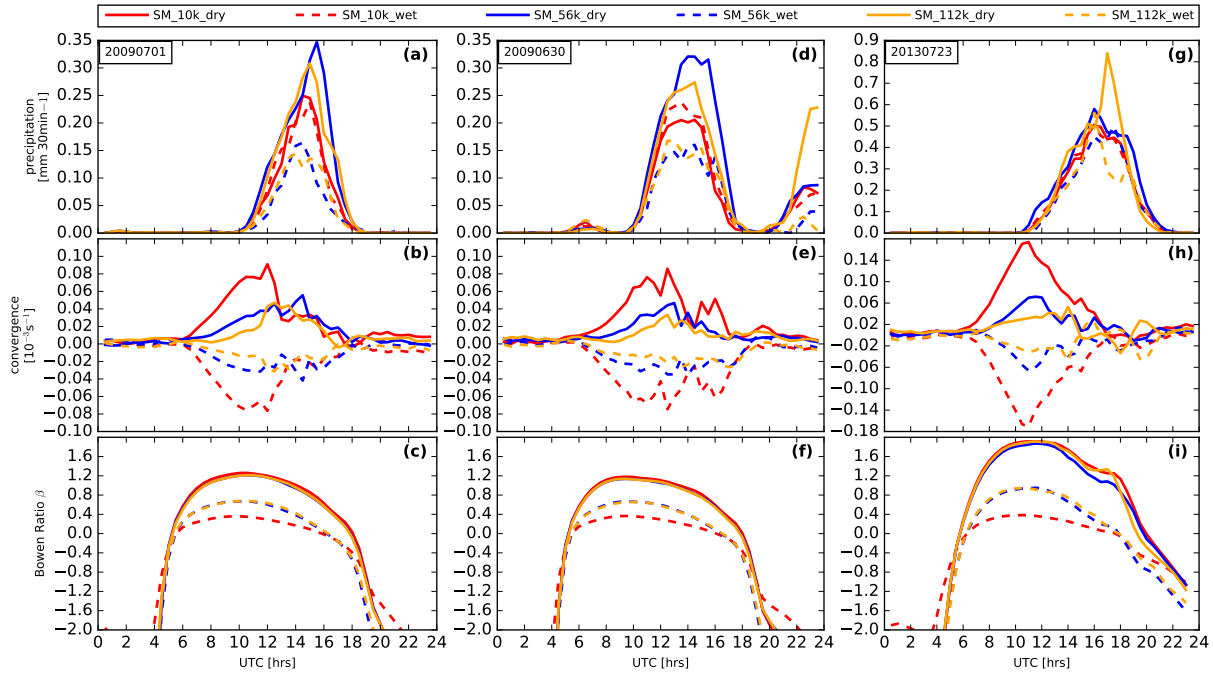

Fig. 4.26.: Domain averaged precipitation, low-level wind convergence and Bowen Ratio for 1 July 2009 ((a)–(c)), 30 June 2009 ((d)–(f)) and 23 July 2013 ((g)–(i)).

allow for distinct signs. After 0600 UTC, all three simulations with different chess boards show a Bowen ratio greater than 1 over the dry, and smaller 1 over the wet patch (Figure 4.26(c)). The reason is that the sensible heat flux increases more over the dry than over the wet patch, and therefore the latent heat flux contributes a larger fraction of the energy input over the wet than over the dry patch (not shown). Additionally, there is convergence over the dry patch and divergence over the wet patch (Figure 4.26(b)). It is suspected that the pronounced sign of convergence and divergence is a result of secondary circulations induced by thermal gradients at the surface. This will now be analyzed exemplarily for 1 July 2009.

The described differences in the energy budget at the surface affect the distribution of moisture and heat within the boundary layer and consequently have an impact on the development of clouds and subsequent precipitation. The moist static energy (MSE) is used to explain the distribution of thermodynamic energy within the atmosphere.

$$MSE = c_p T + L_v Q_v \qquad [4.2]$$

MSE combines the dry static energy ($c_p T$, using c_p=1005 J kg^{-1}K^{-1} and temperature T) and the latent energy ($L_v Q_v$, L_v being 2.6·10^{6}J kg^{-1} and specific humidity Q_v). For better visibility, differences between the chessboard simulations the uniform simulation are displayed. For the analysis all boxes are averaged meridionally covering half a dry, a full wet and half a dry patch (an example of one of these boxes is given in red in Figure 3.3) within evaluation area A. Because of the introduced soil moisture heterogeneities, differential heating occurs at the ground. This induces thermal gradients and consequently near-surface

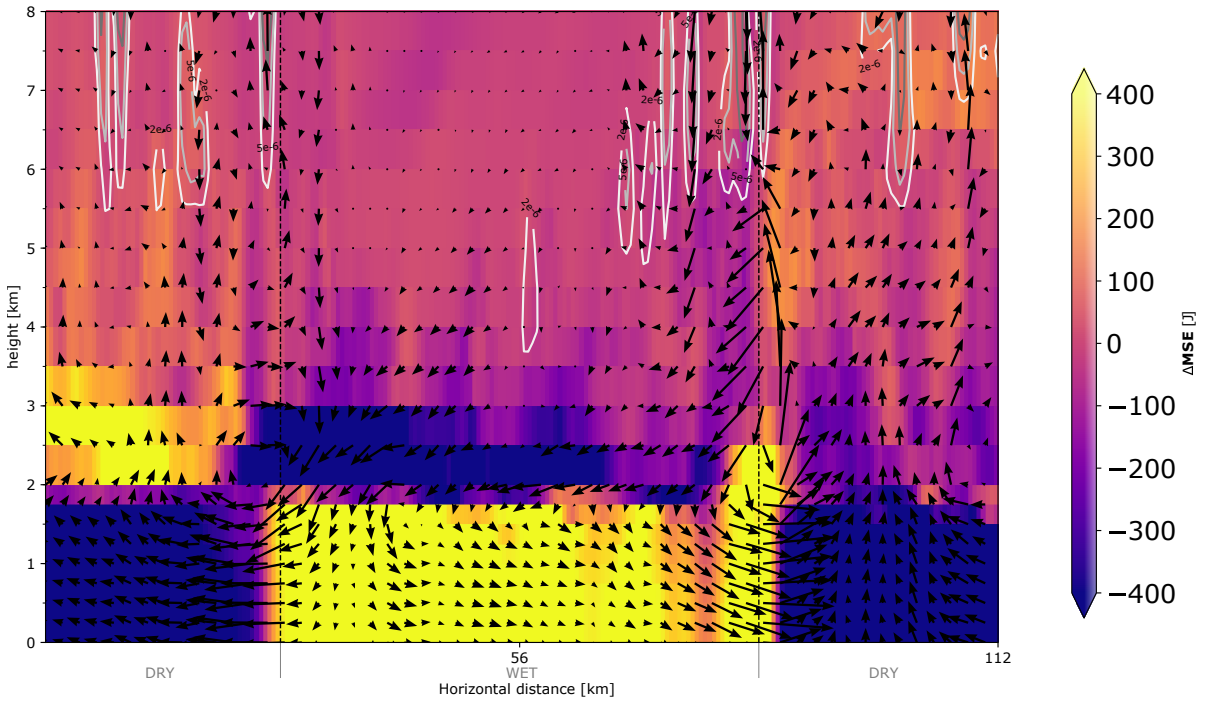

Fig. 4.27.: Cross section of differences in moist static energy (MSE) between the SM_56k and the uniform simulation for 1 July 2009. The contour lines from white to gray denote the 2, 5 and 10 mg kg^{-1} cloud water levels. The cross section was obtained averaging in longitudinal direction over all boxes comprising half dry, full wet and half dry area (red box in Figure 3.3) in evaluation area A.

winds develop from the wet to the dry patch (Figure 4.27). As a result, convergence zones develop over the dry and divergence zones over the wet patch, leading to rising of air over the dry and subsidence over the wet patch. Due to continuity reasons, upper-level winds from the dry to the wet patches are present. Near the ground over the wet patches, positive ΔMSE values are present, mainly because of high values of specific humidity. The moist air is transported with the low-level wind towards the dry patches, where convection is favorable because of the upward movements and the surplus in moist static energy. Therefore clouds form predominantly over the dry patches and result in more precipitation over that area. In the upper-levels over the wet patches, near neutral or negative ΔMSE values are present as the result of subsidence.

Figure 4.27 shows stronger convergence over the right transition zone, than over the left. Consequently, moist and warm air (high ΔMSE) is transported higher upwards into the free troposphere, than over the left transition zone. This region of narrow updraft originates from the superposition of the converging motions over the dry patch and the background wind (mean wind in 850 hPa). On 1 July 2009 the mean background wind in evaluation area A is from the north-east, leading to the sharp updraft over the lee side of the dry patch, where clouds form. Despite the strong signal regarding the location where clouds form, the location where precipitation falls is more variable (not shown). Over the wet patch, the precipitation amount is still about 50% of the amount over the dry patch (Figure 4.14, bottom). This is

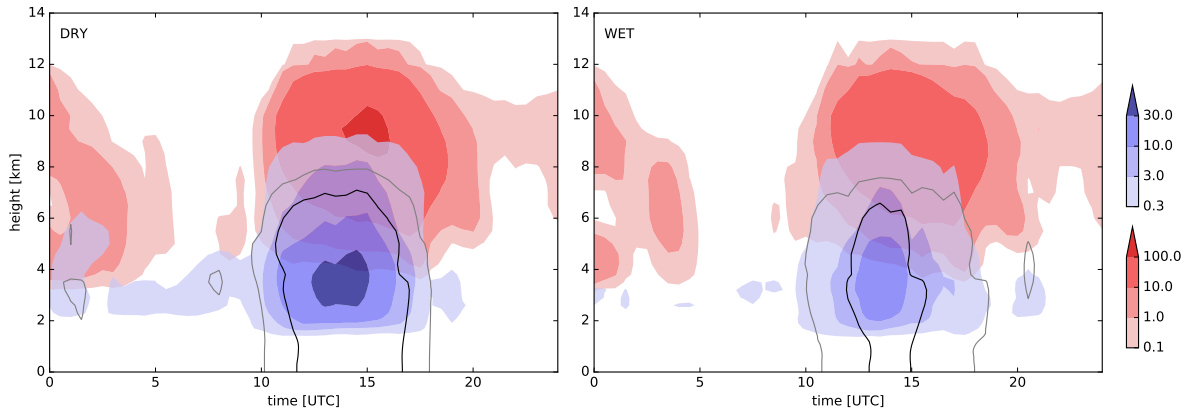

Fig. 4.28.: Temporal evolution in mg kg^{-1}of the liquid (blue), ice (red) and rain water condensate (from gray to black: 1, 10 mg kg^{-1}) for 1 July 2009 SM_56k, showing averages over the dry (left) and wet (right) patch.

probably because of two reasons: first, clouds are transported with the mean wind away from the dry towards the wet patch and second, the location of precipitation is also influenced by the underlying complex terrain. When applying this analysis to the flatter region of northern Germany, precipitation falls predominantly at the edges of the dry patch (not shown), rather than at the center.

The temporal evolution of domain-averaged liquid and ice phase reflects the stronger convergence over the dry patch. At 0900 UTC liquid clouds start to form over the dry patch and only 30-minutes later over the wet (Figure 4.28). In contrast, the ice condensate at 0900 UTC is similar between the two simulations, although the minimum height seems to be 500 m lower over the dry patch. Due to the presence of ice and liquid at the same time, it is not possible to find that the transition from shallow to deep convection is earlier over the dry than the wet patches, which has been shown for idealized simulations by Rieck et al. (2014). Both the liquid and the ice phase grow more rapidly over the dry patch and have higher values around 1500 UTC. Because of the faster cloud development, rain water is present 30-min earlier over the dry than over the wet patch (Figure 4.28). Surprisingly, and in contrast to the bias simulations, there is no shift in the cloud base height.

Within the SM_10k simulations, near-surface winds also establish from the wet to the dry patch because of differential heating. This leads to convergence over the dry and divergence over the wet patches. However, the distribution of ΔMSE is much less pronounced than for the SM_56k case (not shown). The partitioning between moist and dry air is weak, because of the transport with the wind across borders. Also, precipitation amounts are similar over the dry and wet patches. Estimations have shown that cells on 1 July 2009 are, on average, transported up to 5 km within 30 minutes, which is half of a patch. This would be enough to make the signal indistinguishable.

Evaluation domain A is characterized by complex terrain, which certainly also influences the formation of clouds and precipitation by mechanical processes. Additionally, it is not possible to analyze the SM_112k simulations with significance within evaluation domain A, because there is only one box (Fig-

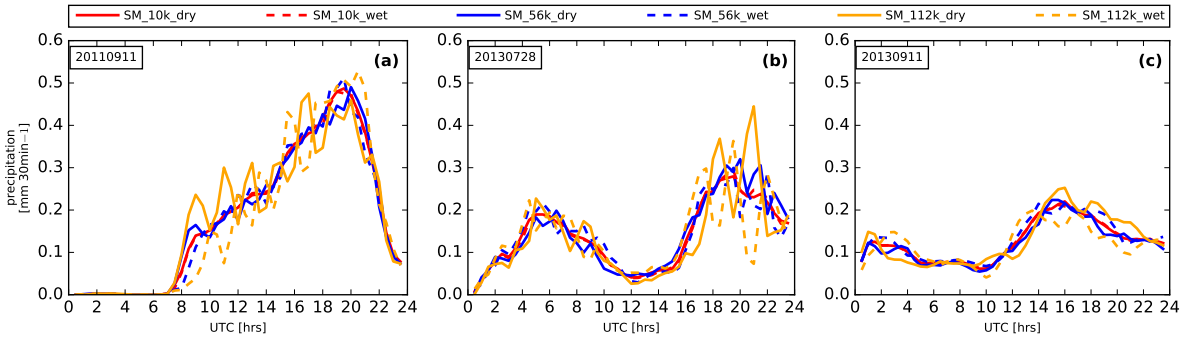

Fig. 4.29.: Domain averaged precipitation for 11 September 2011 (a), 28 July 2013 (b) and 11 September 2013 (c).

ure 3.3) and this cannot be shifted. Therefore, the analysis is done for the whole domain. There, the patterns of MSE in the SM_112k simulation resemble those for the SM_56k run and hence it is concluded that the same mechanisms trigger convection. However, also over the wet patch, there are small and weak regions with updrafts in the SM_112k simulations. It is hypothesized that local updrafts can establish in these simulations because of their comparable large size and the relevance of other trigger mechanisms, which has been similarly stated by Baur et al. (2018). From the results with three different chess boards, it is concluded that there is a scale dependency regarding the precipitation amount and location. It seems that the SM_56k patch is most effective in triggering precipitation as thermally-induced secondary circulations can fully develop. Here, the differences in precipitation amounts between dry and wet patches are more pronounced, compared to the SM_10k and SM_112k simulations.

Strong forcing

The differentiation between wet and dry patches for strong forcing days shows a similar pattern as for the weak forcing days. For nearly all SM_56k and SM_112k simulations, there is more precipitation over the dry patches than over the wet patches, and similar precipitation in the SM_10k run (Figure 4.14). Only on 23 July 2013 in the SM_112k simulation, more precipitation is modelled over the wet patches. For this case, a test simulation was performed, in which the order of wet and dry patches was changed and the opposite effect was found (not shown), indicating that in the relatively small evaluation domain A, it happens that the wer oatches coincides with the region of most precipitation but did not cause it. For all three days, the precipitation evolution in the SM_56k and SM_112k simulations is determined by advected cells passing through the domain, which is concluded because precipitation over the wet and dry patches changes its magnitude in an opposite way (Figure 4.29). In the daily accumulated precipitation, differences up to 5% can still exist, which can be explained by small differences in CAPE over the dry or wet patch, leading to a positive or negative feedback depending on location, timing and most likely the development stage of the cell itself.

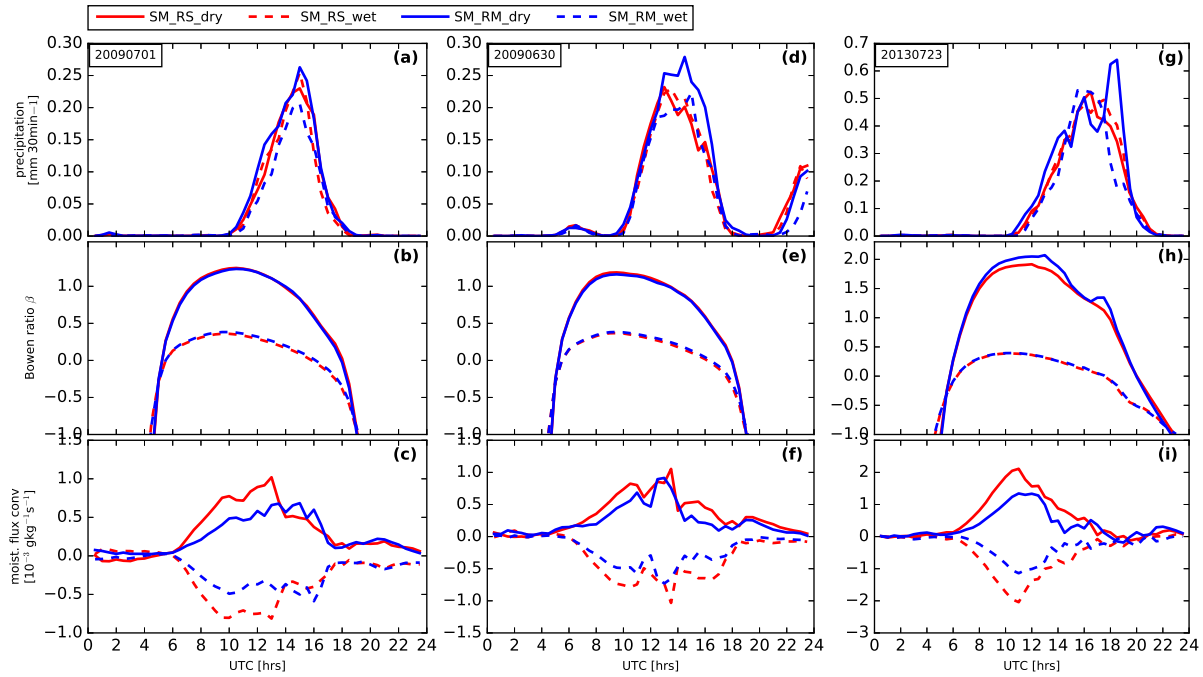

Fig. 4.30.: Domain averaged precipitation, Bowen Ratio β and moisture flux convergence for 1 July 2009 ((a)–(c)), 30 June 2009 ((d)–(f)) and 23 July 2013 ((g)–(i)) for the simulations with random soil moisture structures.

4.3.4. Random experiments

The experiments with randomly distributed patches of increased and decreased soil moisture show no systematic differences regarding the daily precipitation totals. However, two out of three weak forcing cases show more precipitation over the dry patch. On 1 July and 30 June 2009, pronounced differences in the amount of precipitation can be seen in the simulations with medium random structures (SM_RM), where most precipitation falls over the dry patch (Figure 4.30(a), (d)). Despite these differences in the amount of precipitation, the timing is very similar. The SM_RS simulations do not show significant differences regarding the timing and amount of precipitation between the wet and the dry patch. On the third day (23 July 2013) the daily precipitation is higher over the dry than over the wet patch in the SM_RM simulation, because of more precipitation after 1700 UTC. However, and as an exception to the other simulations, the SM_RS simulation shows slightly higher amounts over the wet patch than over the dry (Figure 4.14). Most likely this is by chance as it was already found for the small chess board patterns that the signal of precipitation cannot be distinguished for these small scales. For all three days, the Bowen ratio β exceeds one over the dry patches during day time (Figure 4.30(b), (e), (h)), when the sensible heat flux is greater than the latent heat flux. In contrast it stays below 0.5 over the wet patch. Differential heating, induced by differences in soil moisture, lead to thermal gradients and induces circulations. The moisture flux convergence ($-u\partial q/\partial x - v\partial q/\partial y - q(\partial u/\partial x + \partial v/\partial y)$) shows that low-

level convergence with moisture transport from the wet to the dry patches is present (Figure 4.30(c), (f), (i)). The processes are similar to those seen in the chess board simulations.

Although conditions for convection initiation are more favorable over the dry patches than over the wet patches, concluded from higher moisture flux convergence and more sensible heating, the differences in daily precipitation over the dry and wet patch for the simulations with random soil moisture patterns are much weaker than for the chess board simulations. A reason could be the imposed scale dependency. The SM_RS simulations corresponds roughly to the SM_10k simulation and even the SM_RM simulations are on average only about half as wide as the SM_56k chess board simulations. In both cases, the advection of clouds with the mean wind could be sufficient to weaken the signal of the location of precipitation. Differences in the cloud structure are only visible for the SM_RM simulation and confirm the results from the chess board patterns with more cloud condensate over the dry patch. The simulations with random patterns for the strong forcing days reveal a similar trend as the chess board simulations. Likewise, the impact of CAPE and low-level wind convergence seems to be small, as the time series do not differ much between wet and dry patches (not shown). Again, the conclusion is that the large-scale advection of precipitation determines the overall signal.

4.3.5. Summary and conclusions

In this chapter the effect of soil moisture perturbations on precipitation and cloud structures is investigated with a focus on mountainous regions. Simulations with a dry or wet bias are performed, and spatial gradients by means of chess board and random structures are introduced. The analysis is done for six days, which can be classified into weak and strong synoptic forcing. The previous analysis allows to answer the research questions asked in chapter 2:

(1) The simulations with uniform soil moisture were performed to eliminate the effect of differential heating by horizontal homogeneities. The results show that the the timing of precipitation onset is similar in the reference and uniform simulations and that precipitation occurs in both cases predominantly over the mountain crests. This indicates that the underlying terrain is responsible for the triggering of precipitation. However, the intensity of precipitating cells is modified by the available moisture within the air, which can be locally variable. The specific humidity content in the air depends on the imposed changes in the soil moisture field. Increasing the mean soil moisture content has a negative effect for cases when the initial soil moisture is high, and a positive for the case when the initial soil moisture is lower. This is connected to the stronger susceptibility of evaporation to soil moisture for drier conditions. It also implies, that especially within dry periods, it is crucial to accurately predict the initial soil moisture content, as this may strongly affect the intensity of precipitation.

The timing of precipitation is similar for each weak forcing day between the reference and the bias simulations. The soil moisture only influences the precipitation rate or maximum precipitation amounts. Despite not seeing a systematic soil moisture precipitation feedback, consistent patterns can be seen in time series of atmospheric state variables. Drier soils lead to less moisture and higher temperatures

near the ground than over wet soil. By introducing a dry bias, the Bowen-regime is always changed to values greater than one (i.e. dominant sensible heat flux) and thereby enhancing the low-level wind convergence. In the bias simulations only a small precipitation response, compared to the initial soil moisture, is visible in evaluation area A on two days, but a strong soil moisture – precipitation feedback for one day. This is most likely due to a combination of two mechanisms: First, on the two days with weak response, the initial soil moisture is much higher and closer to saturation than on the day with strong response. For the first two cases, evapotranspiration is then determined by the radiation budget, rather than the soil moisture itself. This hypothesis would need some further testing by performing a sensitivity study with different initial soil moisture conditions. Second, the presence of complex terrain may smooth out some of the signals, which is concluded from a weak, but positive soil moisture – precipitation feedback in the whole domain for these two days. These results support the findings from Barthlott et al. (2011b), who also pointed towards the missing soil moisture – precipitation feedback over complex terrain. These results show that there is an important and complex interplay between terrain height and surface properties, which are both known to affect precipitation initiation. As a follow up, it is suggested to perform simulations with combined changes in the soil moisture and terrain structures.

(2) The weak forcing simulations with chess board patters with length of 56 km and 112 km show a strong location dependency with more precipitation over the dry than over the wet patches, which supports observations by Guillod et al. (2014). Because of differential heating over the dry patches, secondary circulations develop near the borders with converging motions over the dry and diverging motions over the wet patch. The coexistence of diverging motion over the moist patches and background wind leads to a narrow uplift of moist air on the lee-flank of the dry patch. This pattern was also found by Froidevaux et al. (2014) and Taylor et al. (2013). It explains why the results show more cloud condensate, both in the liquid and the ice phase, over the dry than over the wet patch around the onset of precipitation. Contrary to idealized simulations by Rieck et al. (2014) these results do not show differences in the transition from shallow to deep convection. This is because the real-case simulations in this study show shallow clouds throughout the whole day, whereas clouds first have to develop in the idealized simulations. Likewise, no differences are visible in the temporal evolution of precipitation between the dry and the wet patch, which was stated by Rochetin et al. (2017), indicating that the triggering of convection is also determined by other mechanisms.

A scale dependency is observed in the chess board simulations for weak forcing cases regarding the precipitation amount and the chess board size. The simulations with grid length of 10 km are too small to show a distinct change in precipitation amounts, as precipitating cells are transported across borders. The simulations with 56 km chess board size show more precipitation over the dry patches than over the wet patches. Even when weak background wind is present, the cells induced by thermal circulations at the chess board borders have the time to fully develop, before moving into a different patch. There is no pronounced dependency regarding the location of precipitation over the dry patch in evaluation area A. However, within the full domain precipitation falls dominantly close to the edges of the dry

patch. In the 112 km simulations, somewhat less precipitation is simulated over the dry patches than in the corresponding simulation of 56 km patch length. Most likely this difference is because the relative effect of the boundaries to the total area is less and convection can also be initiated by other trigger mechanisms. To fully confirm this hypothesis, it is suggested to run further chess board simulations, introducing different grid lengths.

The simulations with random located dry or wet patches show very similar patterns as the chess board simulations, as (for most cases) more precipitation falls over the dry patch. In all simulations, moisture transport from the wet towards the dry patch can be seen, where convergence zones establish. In the simulations with larger sized random patterns this results in more precipitation over the wet patch, whereas this cannot be seen for cases with small random structures. In general, the difference between dry and wet patches in the simulations with random structures is smaller than in those with chess boards. This possibly has to do with the overall size of the structure, which is even in the simulations with large patches only about half as wide as in the SM_56k simulation. This strengthens the hypothesis that it is possible to observe a scale dependency towards medium-sized structures.

(3) The simulations for strong forcing days are much less affected by the surface forcing than strong forcing days, as the patterns are dominated by the advection of large-scale precipitating cells. However, daily accumulated precipitation amounts in the bias simulations can show up to 5% deviations compared to the reference run. This is because surface conditions slightly influence CAPE and extra instability in the higher atmosphere can then enhance/decrease advected precipitation. For the chess board and random perturbations, the distance an air parcel could move exceeds even the largest patch size and hence no distinguishable signal is visible between dry and wet patches.

The conclusion for the soil moisture simulations and the evaluation over complex terrain is that the timing of precipitation is not changed. The amount of precipitation is modified in various ways, driven by the surface energy balance and the available moisture within the air. Whereas bias simulations show a variety of responses, chess and random simulations show a pronounced negative soil moisture – precipitation feedback, due to the establishment of convergence zones. Therefore these simulations show the greatest change in the location of precipitation.

4.4. Aerosols

Aerosols modify cloud microphysical pathways by acting as cloud condensation nuclei. This can change the hydrometeor distribution as well as the development and structure of the cloud, thereby affecting precipitation. In this chapter, the effect of different cloud condensation nuclei concentration will be investigated.

4.4.1. Homogeneous CCN

Precipitation characteristics

The simulations with varied homogeneous CCN concentrations show precipitation amounts between 0.9–1.3x10^{11} liters on weak forcing and 2.7–4.0x10^{11} on strong forcing days within the simulation domain (Figure 4.31). In evaluation area A, the amounts lay between 1.8–4.3^{10} liters on weak forcing days and 5.3–9.5x10^{10} liters on strong forcing days (not shown). Compared to the continental simulation, weak forcing cases show deviations between -11.1 and +6.9% in the full domain (Figure 4.31, middle). On 23 July 2013, there is a positive aerosol–precipitation response. On 1 July and 30 June 2009 precipitation decreases from maritime to polluted conditions, although this is not systematic on the first day, as precipitation sums are higher in the intermediate than maritime simulation. Within evaluation area A, the precipitation changes are -12.0 to +4.7% , and similar as in the whole domain (Figure 4.31, bottom). This is somewhat contrary to findings from Seifert et al. (2012) and Barthlott and Hoose for the same region, who found a stronger sensitivity of precipitation to CCN due to the coupling with orographically induced dynamics. Differences to these results could originate from (a) the higher model resolution that is used in this study, which allows higher vertical velocities than in the lower model resolutions, (b) the investigation of a limited amount of days compared to the long-term simulations of Seifert et al. (2012), (c) the investigation of a region larger than the mountains itself, where local and remote effects cancel out. In contrast to the full domain, 30 June and 1 July 2009 show no systematic response in evaluation area A, indicating that aerosol effects over mountainous terrain can differ compared to flat terrain. The strong forcing days show smaller deviations than weak forcing days, which are between -9 to +6% within the full domain and -8 to +6% within evaluation area A. In the full domain, 11 September 2011 shows a positive aerosol – precipitation feedback, 11 September 2013 a negative feedback and on 28 July 2013 precipitation increases from maritime to continental and shows similar amounts under continental and polluted conditions. On 11 September 2011, the precipitation response changes between evaluation area A and the full domain, indicating that also under strong forcing conditions, aerosol effects on precipitation may change in different areas.

The cumulative probability density functions of daily precipitation for all CCN specifications within one day look comparably similar (Figure 4.32). Only on 1 July 2009 and 30 June 2009, a shift towards smaller precipitation intensities with increasing CCN concentrations can be seen in the full domain (Figure 4.32, solid line). In addition, the area with precipitation decreases by about 4% (not shown). These

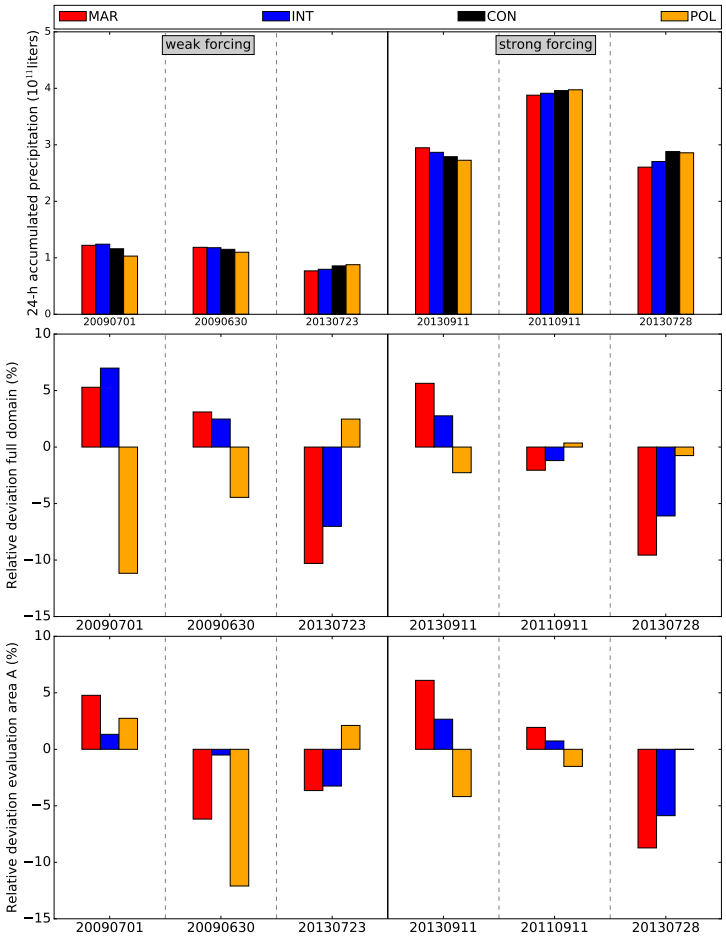

Fig. 4.31.: Top: 24-h precipitation for the cases with weak (left) and strong (right) synoptic forcing for the whole domain. Middle: Relative deviation of the precipitation amounts from the sensitivity runs to the continental (reference) run. Bottom: Relative deviation for precipitation amounts in evaluation area A from the sensitivity runs to the continental (reference) run.

two findings could explain the decrease in precipitation with increasing CCN. For all simulations the time when precipitation starts does not change (not shown). Within evaluation area A, the cumulative probability density functions look even more similar and can thus not explain any differences in precipitation (Figure 4.32, dashed line). Investigating the spatial distribution of precipitation by means of difference plots between the maritime, intermediate or polluted run and the continental simulation, shows that the spatial shift is similar between the full domain and over complex terrain (not shown). For all days, this shift can be up to 80 mm locally, and can be caused even by a small shift in location. Especially over mountainous terrain, this implies that correct aerosol assumptions are very important, as a small shift in the location can have severe effects on the distribution of water into different river catchments.

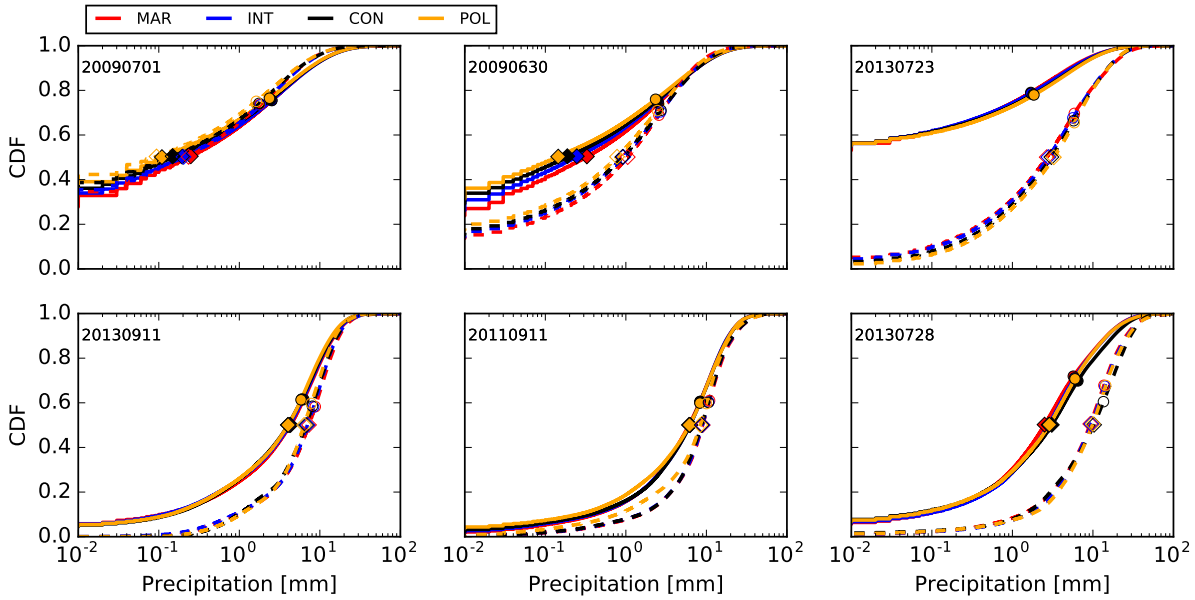

Fig. 4.32.: Cumulative probability density function (CDF) of daily accumulated precipitation for the weak forcing cases (top) and strong forcing cases (bottom). Solid lines are for the full domain, dashed lines for evaluation area A. Filled circles indicate the average, filled diamonds the median for each simulation in the full domain. Open symbols the same for evaluation area A.

Cloud statistics

CCN especially impact the macro- and microphysical aspects of clouds and hence it is worth looking at cloud statistics. Following an approach by Neggers et al. (2003), a cloud is defined as a region of connected grid points where the liquid water path exceeds 50 g m^{-2}. While the average number of clouds is variable between the days, only small variations are visible between the individual simulations for each day (Figure 4.33, left). Within the domain, 1 July, 30 June 2009 and 11 September 2013 show a decreasing number of clouds from maritime (intermediate on 1 July 2009 and 11 September 2013) to polluted conditions (Figure 4.33, left). This could explain the decreasing precipitation amounts, especially because rain intensities and duration do not change (not shown). In contrast, 23 July 2013, 11 September 2011 and 28 July 2013 show a small increase in the number of clouds with increasing CCN, which is also in accordance with the precipitation sums. Interestingly, days with decreasing number of clouds, as CCN concentrations increases, have more clouds (between 893–1190) than days with increasing number of clouds with increasing CCN (between 232–479). The mean area of the clouds is 8 times larger for strong forcing days (242–260 km^2) than for weak forcing days (35–40 km^2). Variations in the average cloud area between the four CCN conditions occur mainly on strong forcing days, most likely because a merging or splitting of a few of these large clouds would slightly affect the number but have a significant effect on the cloud area. 28 July 2013 and 11 September 2011 show a decreasing cloud area, while an increase occurs on 11 September 2013.

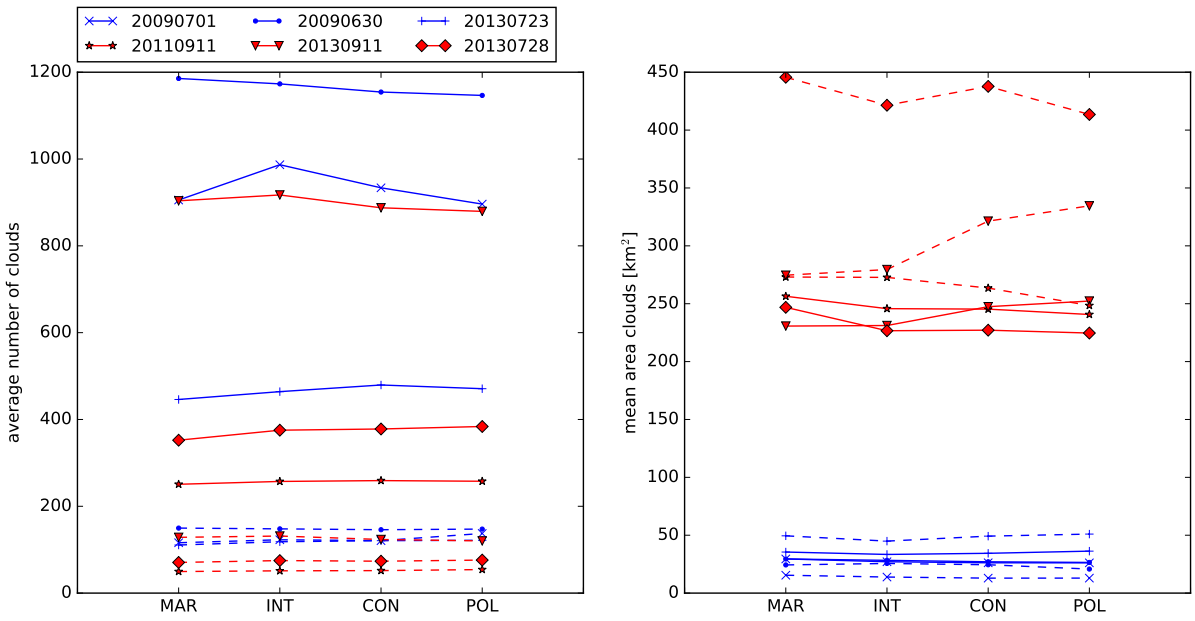

Fig. 4.33.: Average number of clouds, defined as a region of connected points where the liquid water path exceeds $50\,\mathrm{g\,m^{-2}}$, for the maritime, intermediate, continental and polluted CCN concentrations (left) and the corresponding mean area of these clouds (right). Solid lines are for the full domain, dashed lines for evaluation area A.

Cloud microphysics

In order to explain the differences in precipitation sums, microphysical processes are analysed. In a first step, the distribution of the liquid and the ice phase is analyzed within the full domain. Here, only one day is presented for each category, as there is a strong similarity between the days for each category. In the weak case (Figure 4.34, top), after night-time clouds have dissipated, deep-convective clouds develop around 1000 UTC. Whereas the cloud base (defined here as cloud water content $>0.3\,\mathrm{mg\,kg^{-1}}$) stays at a similar level for all simulations, the amount as well as the height at which the cloud water has its maximum increases with increasing CCN. The timing of precipitation derived from the contour lines of rain is similar for all simulations. The evolution of ice-phase stays similar during daytime in all simulations, only after 2000 UTC more ice persists in the polluted simulation, which could potentially impact temperatures at the surface by decreasing nighttime cooling. On the strong forcing case, the ice-phase is very dominant already from the beginning of the simulation. It decreases slightly from maritime to polluted conditions throughout the day. In contrast, the cloud water shows a pronounced enhancement of condensate from maritime to polluted conditions. The rain intensities are stronger on the strong forcing days than on weak forcing days. The $10\,\mathrm{mg\,kg^{-1}}$ contour line of rain shows a decrease in height with increasing CCN. In general, the liquid and the ice phase develop similarly in all simulations.

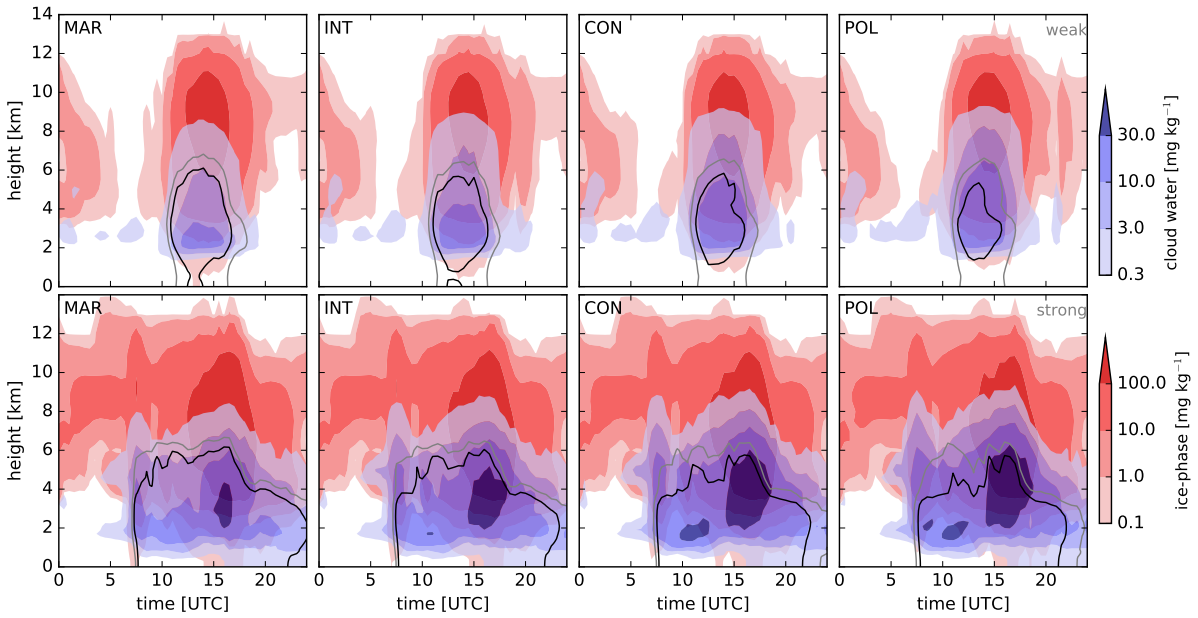

Fig. 4.34.: Domain-averaged mixing-ratios of cloud water (blue fill), frozen hydrometeoros (snow, ice, hail, graupel; red fill), 5 (gray) and 10 mg kg^{-1} (black) rain contour lines. Top row shows 1 July 2009 (weak forcing) and bottom row 11 September 2011 (strong forcing).

Weak forcing

Despite the similar evolution of the liquid and the ice phase, different precipitation totals are simulated. In order to explain these differences in precipitation totals, hydrometeor (cloud water, ice, rain, gaupel, snow and hail) distributions are analyzed in more detail. For the weak forcing days the results are presented for 1 July 2009 (30 June 2009 is similar) and 23 July 2013. The vertical profiles of cloud hydrometeors averaged over space and time look surprisingly similar, given that precipitation totals show an opposite trend (Figure 4.35). The cloud water content increases from maritime to polluted conditions and the maximum is shifted upwards with increasing CCN (Figure 4.35(a), (m)). Along with an increase in QC with increasing CCN, there is a reduction in rain water (Figure 4.35(b), (n)). The reason is the suppression of the warm rain processes towards higher CCN conditions, because of numerous but smaller cloud droplets (not shown). In return, in low CCN conditions, where cloud droplets are larger but less abundant, there is an enhanced growth towards rain drops by autoconversion (Figure 4.35(h), (t)). Despite pronounced differences in the integrated rain content, all profiles converge towards the ground, due to enhanced evaporation in the maritime simulations (Figure 4.35(l), (x)). More numerous but smaller rain droplets are present in the maritime conditions compared to polluted conditions (not shown), which is in accordance with various other studies (e. g. Storer et al., 2010; Altaratz et al., 2008). This leads to a higher surface to volume ratio compared to the polluted case, which explains the enhanced evaporation in the maritime simulations. The similar profiles of rain water near the surface could be one reason why there is no systematic response in the daily accumulated precipitation (Figure 4.31). The hail content

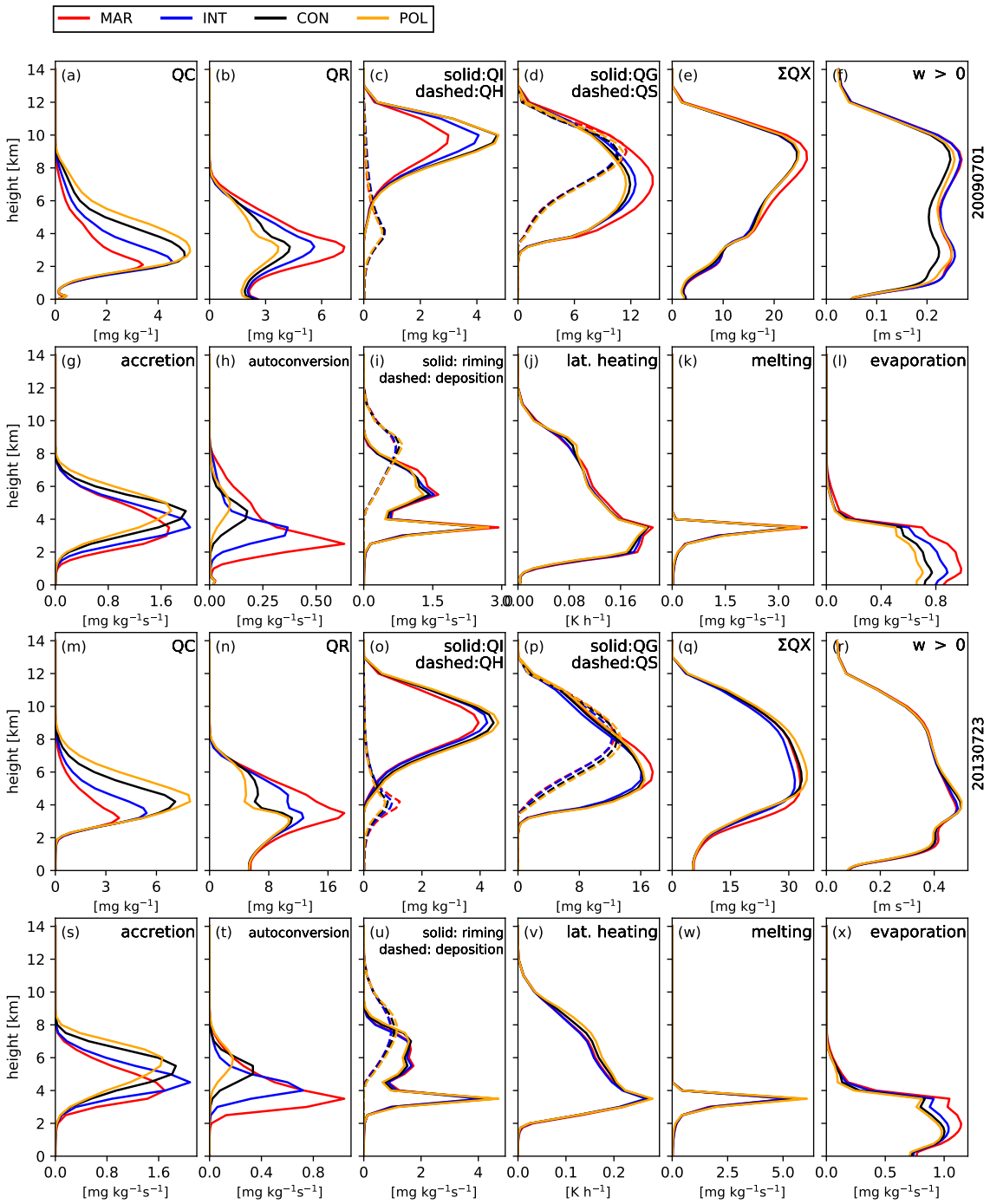

Fig. 4.35.: Time and domain-averaged profiles for cloud water (QC), rain (QR), ice (QI), hail (QH), snow (QS), graupel (QG), summed hydrometeors (∑QX), and vertical velocity W at cloudy grid points ((a)–(f) for 1 July 2009 and (m)–(r) for 23 July 2013). Corresponding conversion and heating rates for accretion, autoconversion, riming, deposition, latent heating, melting and evaporation ((g)–(l) for 1 July 2009 and (s)–(x) for 23 July 2013).

is similar between the four CCN simulations, but ice concentrations increase from maritime to polluted (Figure 4.35(c), (o)). In polluted conditions, the less efficient warm rain process and the higher water load at higher altitudes lead to more ice than in the maritime case. Graupel mixing ratios show a decrease with increasing CCN on 1 July 2009, while the snow content stays similar (Figure 4.35(d), (p)). The difference in graupel mixing ratios is less pronounced on 23 July 2013, but overall amounts are higher than on the other day. Looking at the process rates, vapour deposition slightly increases with increasing CCN and riming rates systematically chante, but the sign depends on the altitude (Figure 4.35(i), (u)). Riming seems to be more pronounced on 23 July 2013, but depending on the altitude, it is higher in the polluted (7-8.5 km) or maritime (4-7 km) simulation. This is probably because riming at lower altitudes happens when graupel collects rain and cloud water while at higher altitudes, ice and snow are the main collectors. The total condensate is highest in the polluted run on 23 July 2013 (Figure 4.35(q)), which corresponds to the runs with highest precipitation amounts for this day (Figure 4.31).

It is still an open question whether the convective invigoration hypothesis is valid (e. g. Fan et al., 2013; Tao et al., 2007; Khain et al., 2008; Altaratz et al., 2014), a process that could influence cloud dynamics significantly. The convective invigoration hypothesis says that more numerous but smaller droplets reach the freezing level in polluted conditions, compared to pristine conditions. Once these droplets freeze, latent heat is released, thereby adding extra energy. This additional energy would invigorate clouds and consequently lead to higher surface precipitation. Despite small differences in latent heating around the freezing level (Figure 4.35(j), (v)), it is not possible to confirm the convection invigoration hypothesis from these simulations. First, differences in freezing between the four CCN are too small to account for differences in latent heating (not shown). Second, the domain-averaged vertical velocity is similar on 23 July 2013 and for three out of four simulations on 1 July 2009 (Figure 4.35(f), (r)), and also the maximum vertical velocity is very similar (not shown). If the hypothesis were true for these simulations, higher updrafts would be expected at the freezing level in the polluted simulations because of the extra energy that is released during phase transition. Third, the depth of the cloud core, defined as the height between cloud base and cloud top (defined by a threshold of cloud ice and cloud water greater $10^{-3}\,\mathrm{g\,kg^{-1}}$), shows similar heights between the four CCN conditions (not shown). Again, in case of convection invigoration higher core depth in polluted conditions would be expected. One reason for the missing convection invigoration could be the use of the saturation adjustment in the COSMO model, which has been shown to enhance condensation and latent heating at lower altitudes, thereby reducing the effect at higher altitudes (Lebo et al., 2012).

Vertically integrated rates of warm-phase (autoconversion and accretion) and cold-phase (riming and vapor deposition) processes show large differences between the two days regarding the individual importance. Warm-phase processes decrease systematically with increasing CCN (Figure 4.36, right) because of a less efficient warm rain process, due to smaller but more numerous droplets. This can be seen by a strong decrease in autoconversion. On 23 July 2013, cold-phase rates increase from intermediate to polluted conditions (Figure 4.36), because of an increase in vapor deposition, while riming stays similar.

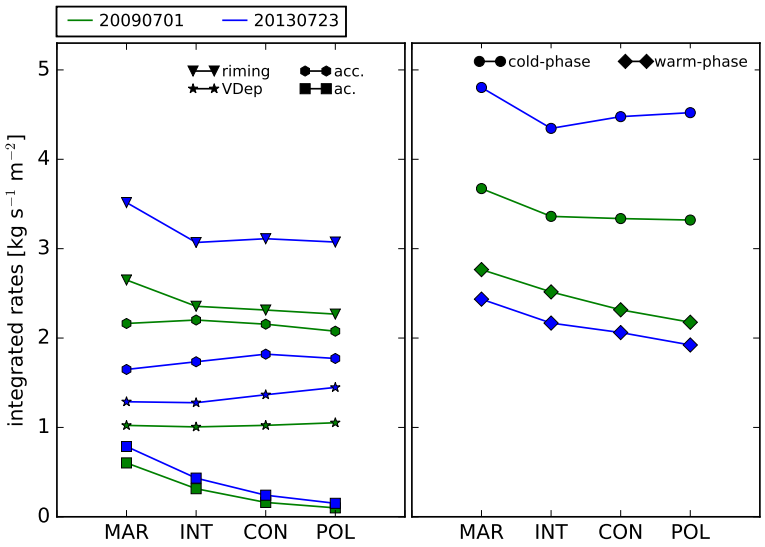

Fig. 4.36.: Integrated rates for autoconversion, accretion, riming and vapor deposition (left) and combined rates for warm (autoconversion and accretion) and cold (riming and vapor deposition) processes (right) on 1 July 2009 and 23 July 2013.

On 1 July 2009, cold-phase rates decrease strongly from maritime to intermediate conditions and weakly thereafter, as both vapor deposition and riming decrease. Not only do the amounts differ between the days, but especially the ratio between warm- and cold-phase processes differs. On 1 July this ratio is 0.71 and on 23 July 2013 only 0.47.

These results highlight the importance of warm-phase processes on 1 July 2009. On 23 July 2013, cold-phase processes become more important with increasing CCN and result in more precipitation. The reason for the different importance of microphysical pathways can be found in the environmental conditions (Table 4.3). On 23 July 2013, the vertical velocity is higher and the instability greater than on 1 July 2009. This imposes more vertical exchange within the clouds and enables more water to reach higher levels, therefore enhancing ice-phase processes. In addition, the lower atmosphere is drier on 23 July 2013 than on 1 July 2009. This could induce secondary effects, as cold-pool strength may be enhanced due to increased evaporation, resulting in more instability and/or more convective cells (e. g. Storer et al., 2010; Tao and Li, 2016).

Within evaluation area A, the precipitation response differs for 1 July 2009 and 30 June 2009 compared to the full domain, while the same systematic behavior is present on 23 July 2013 (Figure 4.31). The profiles of cloud hydrometeors and conversion rates (both not shown) show similar responses to different CCN concentrations as in the full domain. However, looking at the contribution of warm- and cold-phase processes, the ratio on 1 July 2009 is with 0.6 smaller in evaluation area A than within the full domain (0.71) and stays constant (0.47) independent of the region on 23 July 2013. The shift towards cold-phase processes on 1 July and 30 June 2009 is because of changes in the environmental conditions (Table 4.3). As a result of the complex terrain, flow deviation, and differential heating at the slopes, evaluation area A

Tab. 4.3.: Environmental conditions for the simulation with continental aerosol. CAPE values are taken before the onset of precipitation. Vertical velocity and relative humidity are for the lowest 6 km.

		CAPE [Jkg^{-1}]	vertical velocity [ms^{-1}]	relative humidity [%]
20090701	Full domain	470	0.17	68
	Box	670	0.21	69
20130723	Full domain	590	0.33	51
	Box	1095	0.34	61

has stronger updrafts as well as greater variance of w compared to the full domain. This locally enhances the strength of convection and the importance of ice-phase processes for rain formation. Because this does not occur everywhere with an equal contribution, the resulting precipitation response does not show a clear systematic behavior, but most likely represents the combined effect of a positive and negative aerosol – precipitation feedback.

Strong forcing

On 11 September 2013, clouds are on average up to 8 km high, show weak conversion rates and the ratio of warm to cold rates is 0.55 (not shown). Because of the suppression of warm rain with increasing CCN, highest precipitation amounts occur under maritime conditions and lowest under polluted conditions. In the following, the focus will be on the other two strong forcing days. On 11 September 2011 and 28 July 2013, large but shallower clouds with embedded deep convection are present. Thus, domain-averaged processes may not show processes that occur predominantly within the one or other part of the cloud/domain. However domain-averaged quantities represent in most cases the full domain averaged precipitation response well.

On 11 September 2011 and 28 July 2013, the domain-averaged vertical profiles for cloud hydrometeors show a decrease in condensate with increasing CCN at lower levels, but an increase in condensate aloft up to 6 km (Figure 4.37(e),(q)). Increasing CCN leads to more numerous but smaller droplets of cloud water (not shown) which results in increasing cloud water content with increasing CCN (Figure 4.37(a),(m)). Due to the suppression of warm rain with increasing CCN this results in smaller rain content (Figure 4.37(b),(n)), which is supported by the lower accretion and autoconversion rates with increasing CCN (Figure 4.37(g),(h),(s),(t)). Because of similar melting rates (Figure 4.37(k),(w)) between the four CCN setups, the differences in the total condensate at lower altitudes can be attributed to the suppression of warm rain only. On 11 September, the total condensate is thus highest in the maritime simulation below 3.8 km and below 4 km on 28 July 2013. This level represents the freezing level (not shown) and rain decreases sharply above. Here, cold-phase processes become more important. Riming and vapor deposition (Figure 4.37(i),(u)) lead to significant amounts of ice, snow and graupel

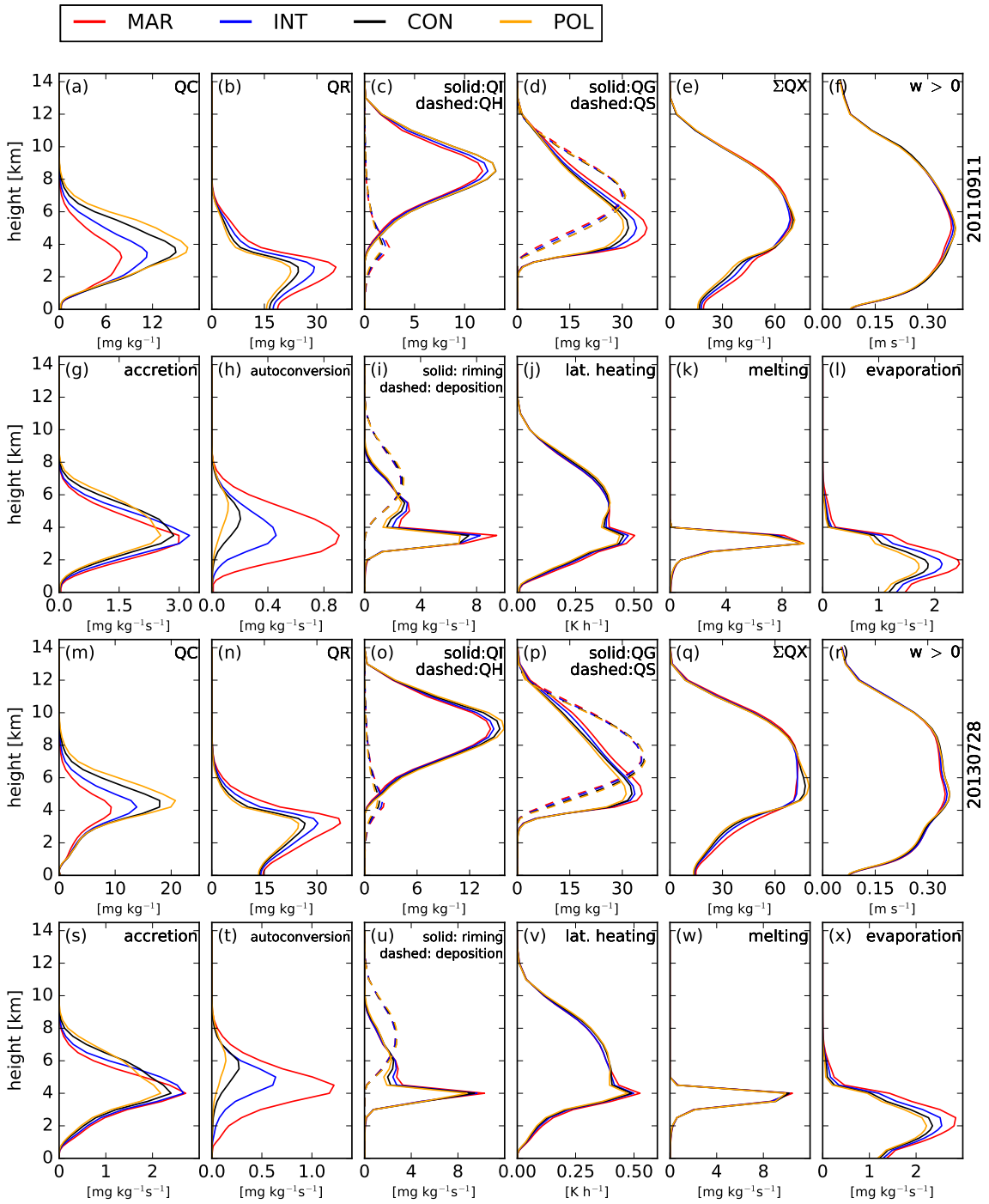

Fig. 4.37.: Time and domain-averaged profiles for cloud water (QC), rain (QR), ice (QI), hail (QH), snow (QS), graupel (QG), summed hydrometeors (ΣQX), and vertical velocity W at cloudy grid points ((a)–(f) for 11 September 2011 and (m)–(r) for 28 July 2013). Corresponding conversion and heating rates for accretion, autoconversion, riming, deposition, latent heating, melting and evaporation ((g)–(l) for 11 September 2011 and (s)–(x) for 28 July 2013).

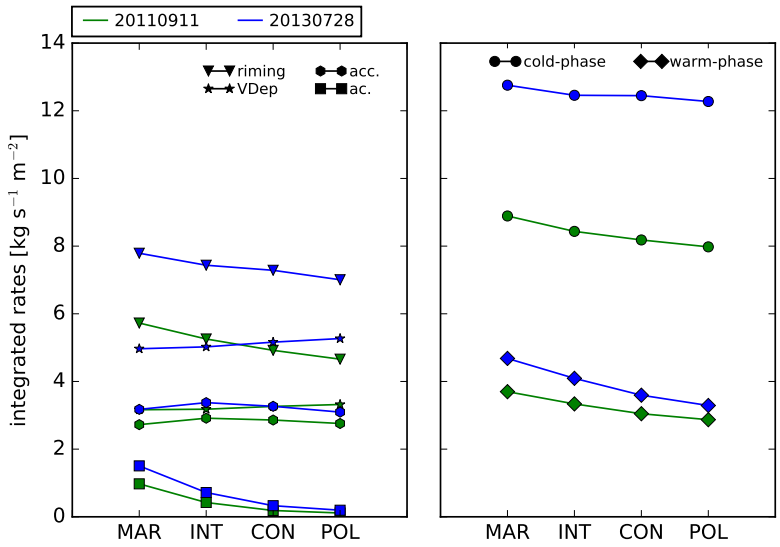

Fig. 4.38.: Integrated rates for autoconversion, accretion, riming and vapour deposition (left) and combined rates for warm (autoconversion and accretion) and cold (riming and vapour deposition) processes (right) on 11 September 2011 and 28 July 2013.

(Figure 4.37(c),(d),(o),(p)). While graupel is up to 25% higher in the maritime than the polluted run, ice and snow are highest in the polluted run. On 28 July 2013, the precipitation response is not as systematic (increase up to continental conditions with increasing CCN, Figure 4.31), which can be attributed to differences in evaporation and the presence of (comparably small) amounts of hail and graupel at the ground.

With increasing CCN, both cold and warm-phase processes decrease (Figure 4.38, right). This is mainly because of decreasing accretion and decreasing riming rates. The ratio between warm and cold-phase processes is 0.38 (11 September 2011) and 0.31 (28 July 2013), which highlights the importance of ice-phase processes. While both days have rather low values of CAPE (domain average below 300 J kg^{-1}), the vertical velocity is on average 0.25 m s^{-1}, and thereby higher than e. g. on 1 July 2009. This vertical exchange could explain enhanced cold-phase processes.

Comparing the results for the full domain and evaluation area A, the aerosol–precipitation feedback changes its sign on 11 September 2011 (Figure 4.31). The ratio between warm and cold-phase processes increases to 0.52 (compared to 0.38 within the full domain). The reason is that when the air approaches the mountain, it is forced to ascend or deviate around it. The wind field on 11 September 2011 shows that there is a strong component flowing over the mountain. While air rises and thus cools, cloud formation occurs. This leads to a significant contribution of warm-phase processes. Under these conditions, suppression of warm rain increases with increasing CCN and hence the maritime run shows the highest precipitation amounts.

Tab. 4.4.: Relative deviation (in %) of the total accumulated precipitation in the run with chess boards compared to the continental simulation.

20090701	20090630	20310723	20130911	20110911	20130728
+0.9	0	-2.5	+0.8	-1.1	-4.4

4.4.2. Heterogeneous CCN

Precipitation Characteristics

The VAR simulation, consisting of chess board patterns with either maritime, intermediate, continental or polluted conditions, has a very similar mean aerosol concentration as the run with homogeneous continental conditions. The total accumulated precipitation is similar on four out of six days between the VAR and the reference simulation (Table 4.4). Only on 23 July 2013 and 28 July 2018, the change in precipitation is higher and in the same order of magnitude as the deviations found for the homogeneous simulations. Despite similar precipitation amounts within the whole domain between the VAR and CON simulation, the precipitation amounts are locally variable. Comparing the mean precipitation in the CON run with the mean precipitation of the three other CCN patches, there is a similar response as between the four homogeneous simulations (MAR, INT, CON, POL) for weak forcing cases (Figure 4.39, middle). On 30 June and 1 July 2009, the mean precipitation decreases from maritime to continental conditions, while it increases on 23 July 2013 (Figure 4.39, middle). On strong forcing days, these deviations are consistent with the findings between the homogeneous runs only on 11 September 2013. Most likely on the other two strong forcing days, dominant advection of cells throughout the full domain lead to a less pronounced signal.

Knowing that differences in precipitation exist, the questions remains whether the local changes in precipitation are restricted to the area where the changes in CCN were made. For this, the mean from all maritime patches in the VAR run and the mean from the same patches in the MAR simulation is compared. Then the same is done for the other CCN. Figure 4.39(bottom) shows that changes are within -1 to +3.5% on weak forcing days, except the maritime patch on 23 July 2013. On this day, the deviation is -14% and this signal also determines the deviation of -2.5% for domain accumulated precipitation (Table 4.4). The higher precipitation in the homogeneous run can be found throughout almost all maritime patches and is not linked to a specific region (not shown). However, the maritime patches have, determined by the large-scale precipitation pattern and the random choice where they are placed, much less precipitation than the other patches (Figure 4.39, top). Therefore a small change precipitation amounts can already impose big changes in the relative differences, which could be one reason for these significant deviations. The strong forcing days show somewhat larger deviations between -3.8 to +3.5%, supporting the hypothesis that precipitation cells are transported across boundaries. Especially for the weak forcing conditions with only light horizontal winds, it could be that the change in precipitation is linked to

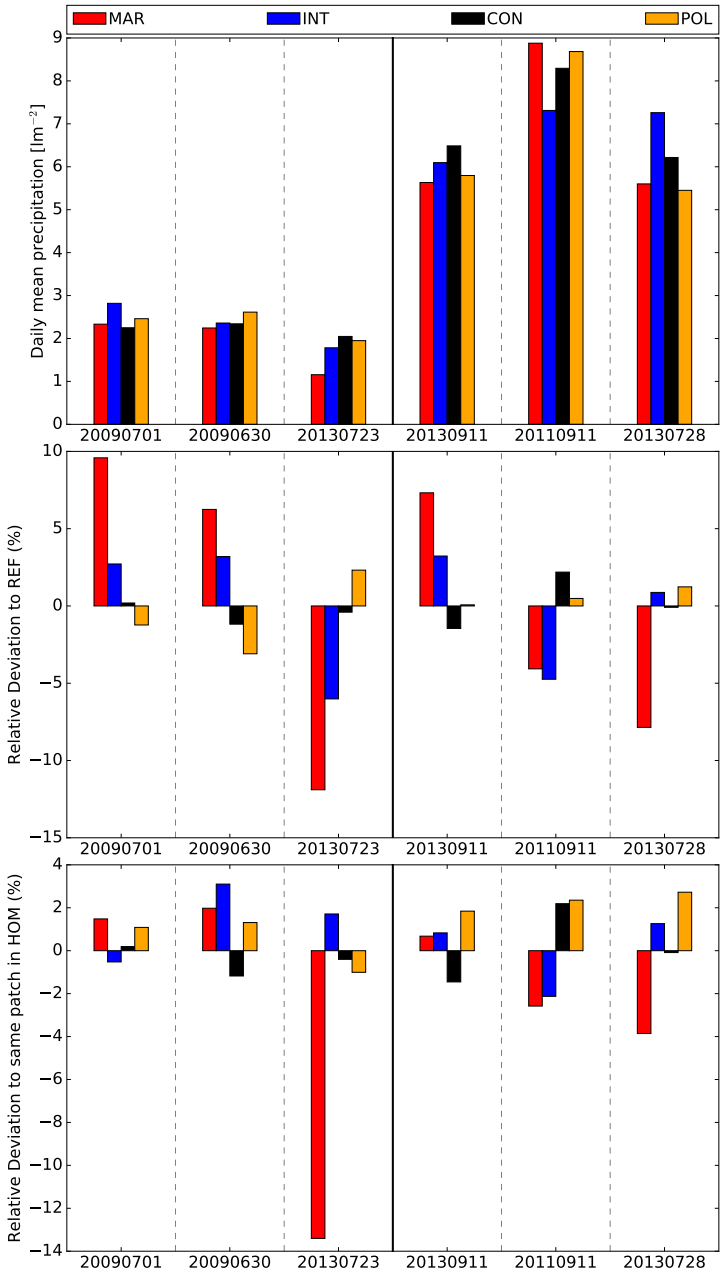

Fig. 4.39.: Top: 24-h mean precipitation for the cases with weak (left) and strong (right) synoptic forcing for the whole domain in the VAR simulation over the individual chess boards. Middle: Relative deviation of the mean precipitation for all maritime, intermediate, continental and polluted patches to the reference (homogeneous CON) simulation. Bottom: Relative deviation of the mean precipitation for all maritime, intermediate, continental and polluted patches to the same locations in the respective homogeneous simulation.

the patch boundaries, i.e. where strong gradients in CCN occur and/or to where cells from neighboring patches get advected. The composites of 24-hr accumulated precipitation, for example for the MAR patches on 1 July 2009, show similar patterns between all maritime patches in the VAR simulation (Fig-

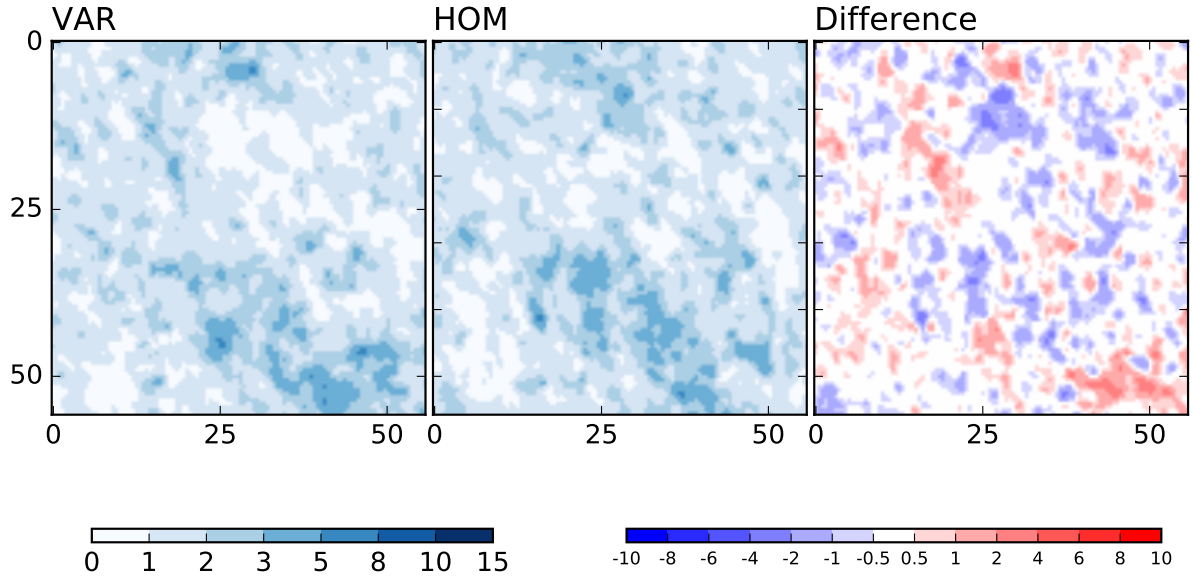

Fig. 4.40.: Rain composite of 24-hr accumulated precipitation [in mm]: Left: derived from all patches with maritime conditions in the VAR (heteorogeneous CCN) run. Middle: derived from the same patches in the MAR simulation. The left colorbar belongs to the two left figures. Right: differences between the two composites, shown by the right colorbar.

ure 4.40, left) and the mean precipitation over the same patches in the MAR simulation (Figure 4.40, middle). Also, the difference plot (Figure 4.40, right) suggests that the location is not affected much by CCN heterogeneities, but that small areas with positive or negative deviations are close to each other, which almost cancel out when looking at the whole area.

Cloud Microphysics

The mean precipitation shows substantial variations locally and also between the patches in the VAR and the corresponding patches in the homogeneous simulation. These signals are most likely governed by cloud microphysical processes as a result of different CCN. For simplicity, cloud microphysical processes are only analyzed for two days, one of each category respectively. The hydrometeor distribution and the rates vary between the four CCN (Figure 4.41) in a similar way as between the four homogeneous runs (Figure 4.35). More numerous but smaller cloud droplets lead to less rain water with increasing CCN. Rain and cloud water then freezes and undergoes riming and vapor deposition to graupel, snow and ice (Figure 4.41). The exact numbers, which are shown in the plots may depend on the location of the patches. Because the large-scale synoptic situation mainly influences where precipitation falls, cloud water in the polluted run can be close to the amount in the continental run simply because of the (random) choice where the polluted patches are placed. To fully confirm this hypothesis, it would be required to rerun simulations, in which the chess boards are swapped. However, the overall characteristic fits well to the previous observations for the homogeneous runs. For the intermediate, continental

and polluted patches, the differences between the homogeneous and the VAR simulation is very small. The difference between the hydrometeors simulated over the maritime patch in the VAR (solid lines) and the homogeneous MAR (dashed lines) show higher amounts of rain water in the homogeneous run even at the ground (Figure 4.41(b)), despite higher evaporation in the MAR than the VAR simulation (Figure 4.41(l)). This represents the -14% difference in mean precipitation (Figure 4.39 (bottom)). The higher amounts of rain water in the homogeneous run result from more cloud water produced within the saturation adjustment (Figure 4.41(g)) followed by higher accretion and autoconversion of that cloud water to rain (Figure 4.41(h)). More condensate is then converted to graupel (Figure 4.41(g)) via riming (Figure 4.41(i)). Especially the vertical velocity is lower over the maritime patches than over the other patches, which could explain the lower total condensate (Figure 4.41(e)) and hence lower precipitation sums (Figure 4.39 (top)).

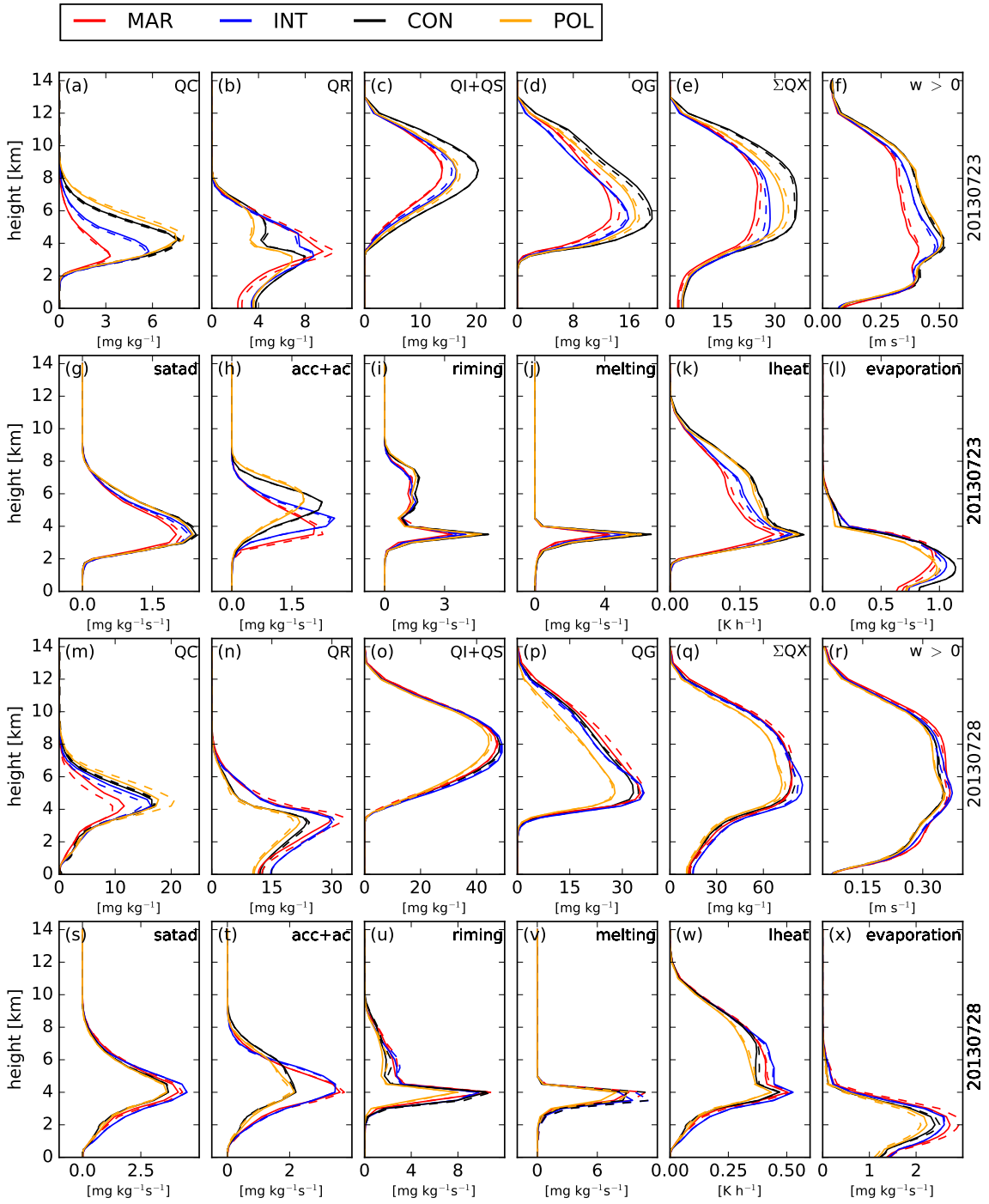

Fig. 4.41.: Time and domain-averaged profiles for cloud water (QC), rain (QR), ice (QI), hail (QH), snow (QS), graupel (QG), summed hydrometeors (∑QX), and vertical velocity W at cloudy grid points ((a)–(f) for 1 July 2009 and (m)–(r) for 11 September 2011) and corresponding conversion and heating rates for the saturation adjustment (satad), accretion (acc), autoconversion (ac), riming, melting, latent heating (lheat) and evaporation ((g)–(l) for 1 July 2009 and (s)–(x) for 11 September 2011). The solid lines are for the patches from the VAR simulation and the dashed lines for the same patches in the homogeneous simulation.

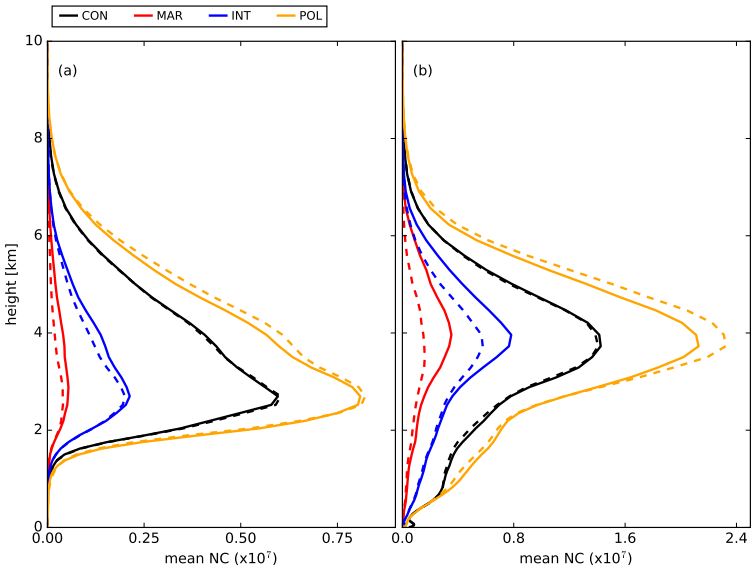

Fig. 4.42.: Domain average number concentration of cloud droplets for (a) 23 July 2013 and (b) 28 July 2013. The solid lines are for the patches from the VAR simulation and the dashed lines for the same patches in the homogeneous simulation.

During strong forcing conditions, mainly the amount of liquid condensates varies between the patch in the VAR and in the corresponding homogeneous simulation (Figure 4.41). Over maritime and intermediate patches, the concentrations of cloud water are higher in the VAR than in the homogeneous simulation, while the opposite holds true for the polluted patches (Figure 4.41(m)). The reason for this are differences in the number concentration, which follow the same trend as the profile of cloud water (Figure 4.42). In the heterogeneous case, when air is transported from a patch with high CCN to a patch with lower CCN conditions, it will take some time until the higher amount of cloud droplets has degraded. In the opposite case, a sharp increase in number concentration occurs. This transition zone spans about 10 km (not shown). As a consequence, the number concentration is higher over the maritime patches in the VAR simulation than over the same patches in the MAR simulation. Differences in the rates between the VAR patch and the corresponding homogeneous run occur in the melting (Figure 4.41(v)), as these rates are higher in the VAR simulation. Graupel profiles differ between 6–11 km, mainly in the maritime simulation (Figure 4.41(p)). Ice and snow profiles are not affected much by heterogeneous CCN patterns (Figure 4.41(o)). But different distributions in QC lead to different size distributions in QR (not shown), which leads to higher evaporation rates with increasing number but smaller rain drops (Figure 4.41(x)).

4.4.3. Summary and conclusions

The aim of this chapter was to investigate the impact of aerosols on clouds and precipitation over Germany in different weather regimes, to extend the analysis of how different processes influence convective precipitation. Therefore, numerical simulations are performed with the COSMO model at 500 m grid

scale for six different days. For each day, four cases with different, spatially homogeneous CCN conditions are simulated. In addition there is one simulation with spatially heterogeneous CCN conditions by means of chess board patterns. Within the following, answers to the research questions formulated in chapter 2 are given:

(1) The results for the homogeneous simulations show that different aerosol assumptions change absolute precipitation up to 15%, supporting the idea that aerosol assumptions matter for quantitative precipitation forecasting (e. g. Barthlott et al., 2017; Miltenberger et al., 2018). The change in precipitation with varying CCN is not consistent between the individual days, but shows an almost systematic behavior within each day individually. On two days an increase in CCN leads to a decrease in precipitation and on one day this decrease is only systematic from intermediate over continental to polluted conditions. Those days are characterized by a high number of individual clouds. On the other three days, increasing CCN leads to an increase in precipitation and the number of clouds is lower on these days. Within this context, the number of clouds could give an indication on the environmental conditions. The effect of aerosols on precipitation over complex terrain has a similar magnitude as within the whole domain, but shows on three days a less systematic or an opposite response, highlighting the complex effects that mountains impose on cloud structures. Precipitation differences up to 80 mm daily are simulated for distinct locations, which is especially important to predict properly over complex terrain, as the location of precipitation determines in which river catchment the water flows.

Despite these pronounced differences in precipitation amounts, the sensitivities of cloud hydrometeors look surprisingly similar. With increasing CCN, smaller but more numerous cloud droplets exist, leading to a reduction in rain production. Because of more cloud water at higher altitudes, snow and ice increase with increasing CCN, whereas at lower altitudes graupel is dominant in low CCN conditions. While the overall shape of the conversion rates also look similar, their relative contribution matters. The ratio between autoconversion plus accretion over riming plus vapour deposition is a good indicator to estimate the precipitation response within the full domain, independent of the synoptic situation. Despite only a limited number of days, mean daily ratios above 0.55 show decreasing precipitation amounts with increasing CCN. Here, the suppression of warm rain leads to a decrease in precipitation with increasing CCN. Days when the ratios are below 0.47 show increasing precipitation with increasing CCN. Here, cold-phase processes are more important which have a buffering function as their importance increases with increasing CCN (Stevens and Feingold, 2009). To further strengthen this argument more simulations for other days are required. In any case, the environmental conditions mainly determine the relative importance: Under weak synoptic conditions, the day with high instability, strong vertical velocity and low relative humidities show enhanced cold-phase processes. This is in accordance with findings from Noppel et al. (2010), who found changing precipitation responses with varying CAPE values and supports findings from Seifert et al. (2012), that depending on environmental conditions, the importance of microphysical pathways changes. Under strong synoptic conditions, when low instability exists, cold-

phase processes become important only on days when the vertical velocity is high. An increase in vertical velocity could possibly be due to enhanced secondary effects or thermally induced circulations.

Although there is a strong relationship between the dominant rates and the overall precipitation behavior within the full domain, it is not possible to fully explain absolute differences in precipitation. Possible reasons are the non-linear behavior of microphysics and the evaporation of raindrops at lower levels. Especially the latter has a strong effect on determining whether increasing CCN has a positive or negative feedback on precipitation (Tao et al., 2007; Barthlott et al., 2017). Also, the results over complex terrain cannot be fully explained by this ratio. In addition to the above named processes, it seems that the non-systematic precipitation response over complex terrain is due to an increased importance of cold-phase processes at individual locations.

(2) The simulations with heterogeneous CCN patterns reveal usually a smaller change in domain accumulated precipitation amounts compared to a simulation with similar domain averaged concentrations. However, within the individual patches the deviations can be substantial. Strong forcing days show the highest changes due to advection of precipitating cells and aerosol loads from fields with higher concentrations to those with low concentrations. The latter mainly influences the cloud number concentration, which determines the amount of rain droplets. Because of this advection, aerosols impose a remote effect on cloud structures and precipitation. Weak forcing days show smaller changes than strong forcing days on the full domain. However, the precipitation sums show the same systematic behavior between the four patterns as in the simulations with homogeneous CCN. These findings indicate that the local effect of aerosols is substantial and that cloud condensation nuclei influence the development of the clouds right at their source. Therefore it might be of interest to implement local aerosol sources into the numerical model, as it is possible with the framework of COSMO-ART (Vogel et al., 2009).

(3) There is no systematic difference between weak and strong forcing conditions. Instead, the environmental conditions mainly determine the precipitation response at the surface, which can either be an increase or decrease in precipitation with increasing CCN. The change in precipitation, induced by homogeneous CCN variations, is, averaged over a large domain, a little bit higher on weak than on strong forcing days. For the simulations with heterogeneous aerosol concentrations the differences are visible in an opposite way: strong forcing days show on average a higher precipitation difference than weak forcing days. The reason for both findings could be the nature of strong forcing days, in which the location and amount of precipitation is more determined by the large-scale synoptic pattern, than by local surface-triggered processes.

5. Synthesis and Outlook

There is still a large uncertainty by which mechanisms do surface and aerosol heterogeneities influence precipitation. Therefore, this study takes a very broad approach investigating the relative contributions of these components. Numerical simulations are performed with the COSMO model, using a 500-m grid, which spans Germany and eastern France. Subsequently, the orography, the soil moisture, and aerosols are perturbed. For this (i) the terrain is incrementally smoothed and flattened, (ii) the magnitude of the soil moisture field is changed and soil moisture is redistributed into chess board and random structures using two discrete values and (iii) four different homogeneous aerosol concentrations are used and chess board patterns with spatially variable concentrations are implemented. This study is unique as it is the first to investigate the contributions of surface and aerosol heterogeneities for the same days. The individual contributions and important pathways are studied in Chapter 4, while this synthesis provides an overview of the results and focuses on the relative importance in different weather regimes. Within the following, the focus will be on the full model domain. This is important to note as the runs with flattened orography only impose changes on a small part of this large domain. In contrast, all other perturbations affect the whole domain. With the help of this study it will be possible to derive the importance of different perturbations for numerical weather prediction ensembles. These ensembles have received a lot of attention in recent years as they provide a valuable tool for predicting precipitation at longer forecast ranges (Raynaud and Bouttier, 2017).

The most important findings, obtained in the individual chapters, are listed below and are summarized in Figure 5.1:

- *Orography* changes the domain accumulated precipitation by -8 to +11%. There is no consistent feedback sign, but it can be said that the low-level wind convergence strongly influences the initiation of deep convection, both regarding location and timing. In the absence of mountains, precipitation is delayed by about two hours, but triggering of convection can still be reached by the formation of low-level wind convergence zones as a result of thermal differences, cold-pool outflow or due to the formation of boundary-layer rolls. Also, changes in the atmospheric humidity due to delayed or weaker precipitation can affect precipitation intensities further downstream. Smoothing of individual valleys has a smaller impact on the total precipitation totals (usually between -4 to +2%, except on one day), but does influence precipitation amounts locally by small shifts in the location. These results are published in Schneider et al. (2018).

- *Soil Moisture* perturbations impose changes between -15 and +17% (one day +40%) on the precipitation amount. The soil moisture affects the surface energy balance by changing the partitioning of available energy into latent and sensible heat. For this the amount of evapotranspiration is crucial, which itself depends on the initial soil moisture content. In cases with high soil moisture, radiation determines the amount of latent heat, while in conditions with low soil moisture content, the latent heat flux is limited by the amount of moisture in the soil. As a result, the imposed changes can lead to a positive or negative soil moisture – precipitation feedback in cases with altered heterogeneous soil moisture fields. The implementation of artificial soil moisture fields, that consist of two discrete values (e. g. chess boards or random shapes), lead to the formation of convergence zones at the boundaries between the regions, where thermal near-surface gradients exist. These convergence zones initiate precipitation primarily over the drier regions, which results in a negative soil moisture – precipitation feedback of -5 to +6%. By changing the moisture and energy budget within the boundary layer, the cloud structure changes with usually higher cloud base over the dry than the wet patch.

- *Aerosols* change precipitation amounts by -11 to +7%. While each individual day usually shows a systematic trend with varying aerosol concentrations in itself, the days can behave very differently between each other. On days with weak and short lived convection, more aerosols result in less precipitation because of the suppression of warm rain. In deeper, more organized convection, interactions with mixed-phase microphysics results in increased precipitation with increasing aerosols, and precipitation changes are with +3% lower than in weak convection situations.

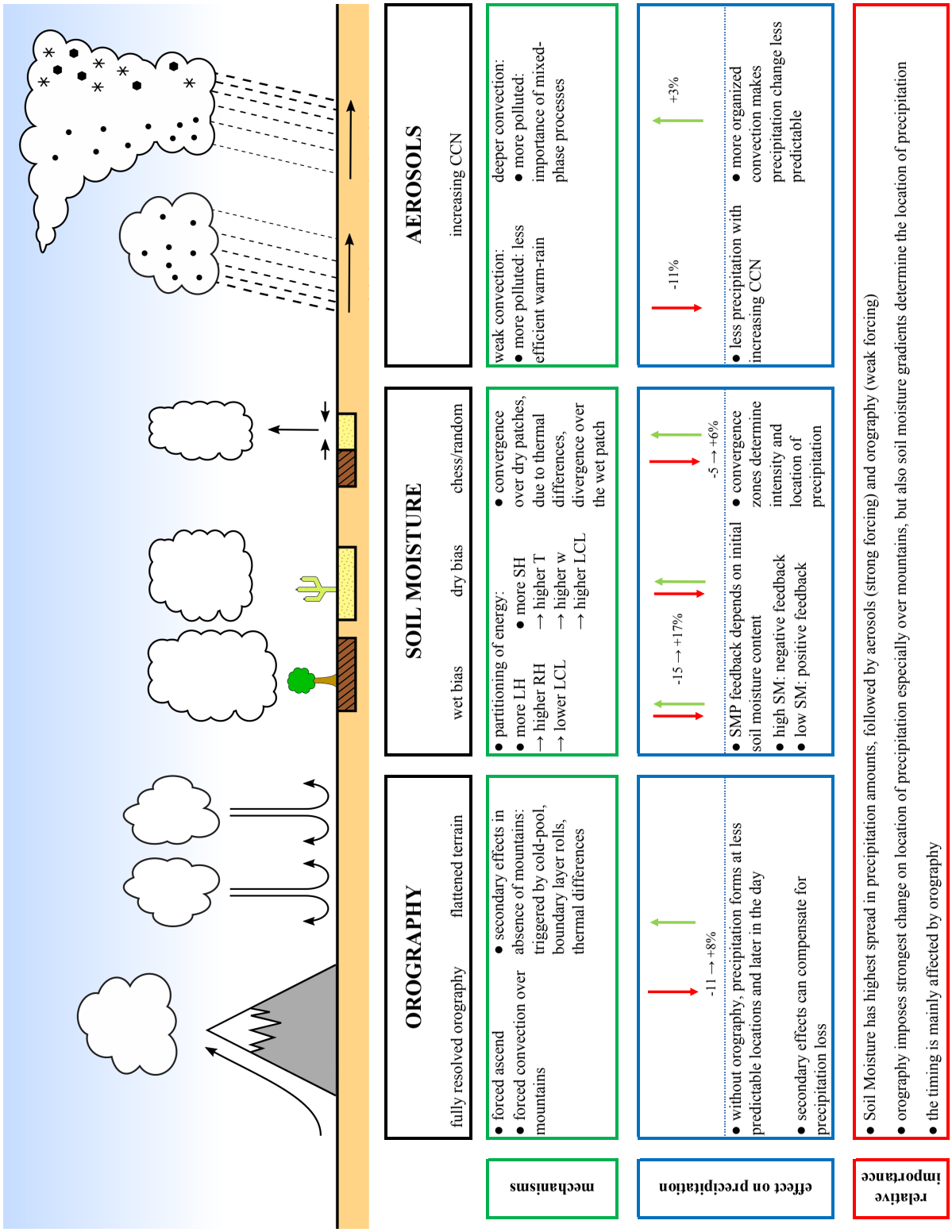

Fig. 5.1.: Summary of the most important results from this thesis including the simulations, mechanisms found, effect on precipitation and the relative importance.

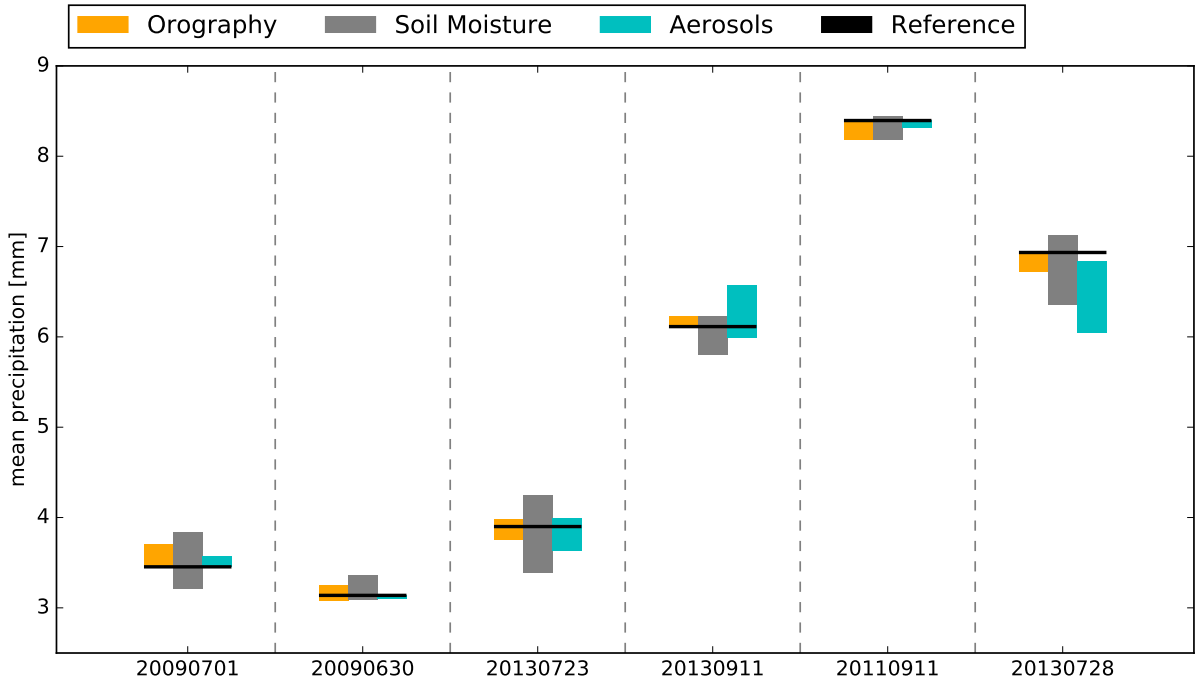

Fig. 5.2.: The bars show the spread between the upper and lower values for mean precipitation from each set of perturbations for orography, soil moisture and aerosols.

In a next step, all simulations with perturbed orography, soil moisture or aerosols are treated in groups, i.e. all orography simulations are considered together. For all weak forcing days, the soil moisture perturbations show the largest differences between the simulations, as the minimum and maximum mean values lay farthest apart (Figure 5.2). Soil moisture affects the surface energy balance, the boundary layer structure and even the atmospheric stability. It therefore shows a strong impact on the amount of precipitation. For two of the three days, orography has the second largest impact. Especially under fair weather conditions with light background winds, the formation of low-level convergence zones induced by mountainous terrain becomes more important. For strong forcing days, soil moisture and aerosols show the largest difference between the simulations. Here, the impact on cloud processes by changes in the environments (e. g. temperature and humidity) as well as microphysics becomes more important.

The timing of precipitation is of great interest when predicting precipitation events. By modifying atmospheric conditions, like stability, the onset of convection can be changed. The results of this study, however, show only very small responses regarding the initiation of precipitation (Figure 5.3). It needs to be said that all precipitation data is given on 30-min intervals, and hence smaller differences in timing cannot be resolved with these data sets. The simulations with flattened mountains show a delay in timing of precipitation over the perturbed area due to reduced low-level wind convergence. However, this effect is not visible when precipitation within the full domain is analyzed. Because the flattening of a full mountain range imposes a rather dramatic impact to the simulations, it can be concluded that problems in the correct timing of precipitation for numerical weather prediction cannot be attributed to incorrectly

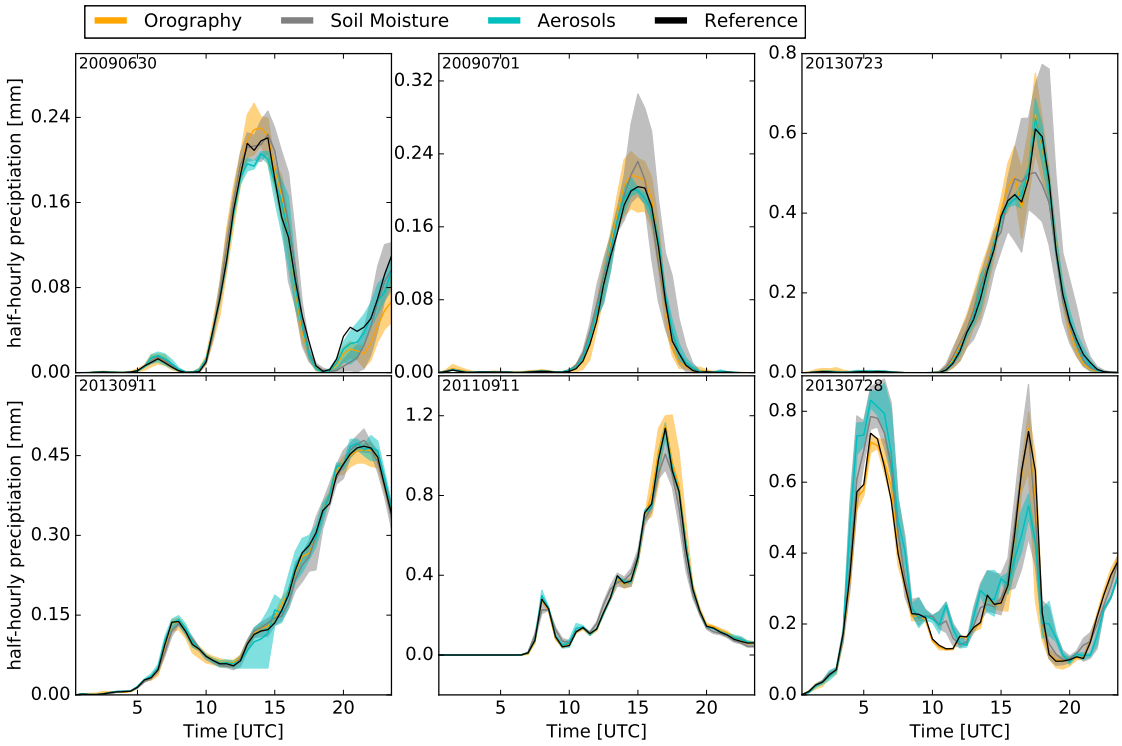

Fig. 5.3.: Timing of precipitation showing minimum and maximum of mean precipitation for each set of perturbations.

represented orography, soil moisture and aerosols. Still, on a local scale, the timing of precipitation could be influenced by improvements in the representation of orography, which has even lead to a better prediction of precipitation in previous studies (Kühnlein et al., 2014).

In addition to the amount and timing of precipitation, it is desired to forecast the correct location of precipitation. This study does not focus on the quantitative model evaluation with observations, but it allows an investigation into the effect that different model setups have on the location of precipitation compared to a reference simulation. For this, the difference between each two-dimension daily accumulated precipitation field of the perturbed run and the reference run on that day is calculated and one boxplot derived for all difference fields of the orography, soil moisture and aerosol perturbations (Figure 5.4). The means are around zero, which indicates that the perturbations do not, on average, change the precipitation totals much within the domain. However, the distributions differ depending on the chosen day and the type of perturbation. For all days, the soil moisture simulations show the largest spread between the 5–95% percentile. On weak forcing days, aerosol perturbations give the smallest spread, while on strong forcing days, perturbations in orography give the smallest (similar) spread on two (three) days. The larger interquantile range on strong forcing than on weak forcing days can be explained by the larger precipitation totals. A small shift in location of precipitation can result in a large difference regarding the amount of precipitation at a particular grid point. This analysis does not give any indication how large the spatial shift is, whether it is in the range of a few kilometers or a few hundred. From the

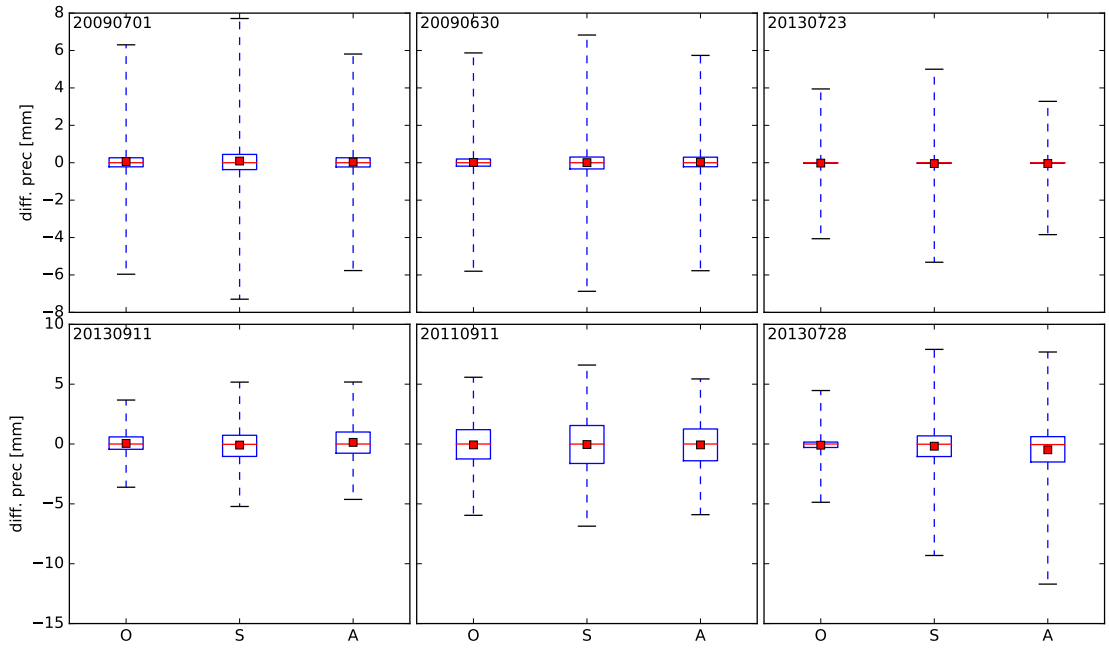

Fig. 5.4.: Boxplot showing the difference in precipitation between the reference and all runs with orography (O), soil moisture (S) and aerosol (A) perturbations. Red lines denote the median, red squares the mean. Upper and lower whiskers show the 95% and 5% percentile and the interquartile range is between 25–75%.

previous analysis in the individual chapters, it was evident that systematic shifts in precipitation were visible e. g. from wet to dry patches in the soil moisture simulations or further downstream in simulations with flattened mountains. For these and all other simulations, it would be worth investigating the spatial effects in more detail to appoint a dominant scale.

In order to understand the spread within each group of perturbations, the individual data sets are now considered. The mean amount, the distribution and the area of precipitation are displayed in Figure 5.5 for all simulations. This plot highlights again the complexity of the dataset, as it is not possible to deduce a clear systematic behavior between the days. The dominant effect that soil moisture has on the mean precipitation (Figure 5.2) is mainly due to the effects imposed by the SM_075, SM_125 and sometimes SM_UNI simulation and the effect is stronger on weak than on strong forcing days. The two first simulations, in which the original soil moisture field has been increased or decreased by 25% represent reasonable uncertainties, as simulations and observations of soil moisture differ up to 30% in reality (Hauck et al., 2011). The strong forcing days show a prominent effect on the area with precipitation, as all simulations with chess boards or random structures show less area with precipitation than the reference simulation. The dominant effect on precipitation imposed by changes in initial soil moisture strengthens the important role that soil moisture has on precipitation. It highlights that initial soil moisture fields have to be treated with caution, i. e. always asking how good they are or how well they have been assimilated into the model. It also encourages and suggests to further study the effect of realistic

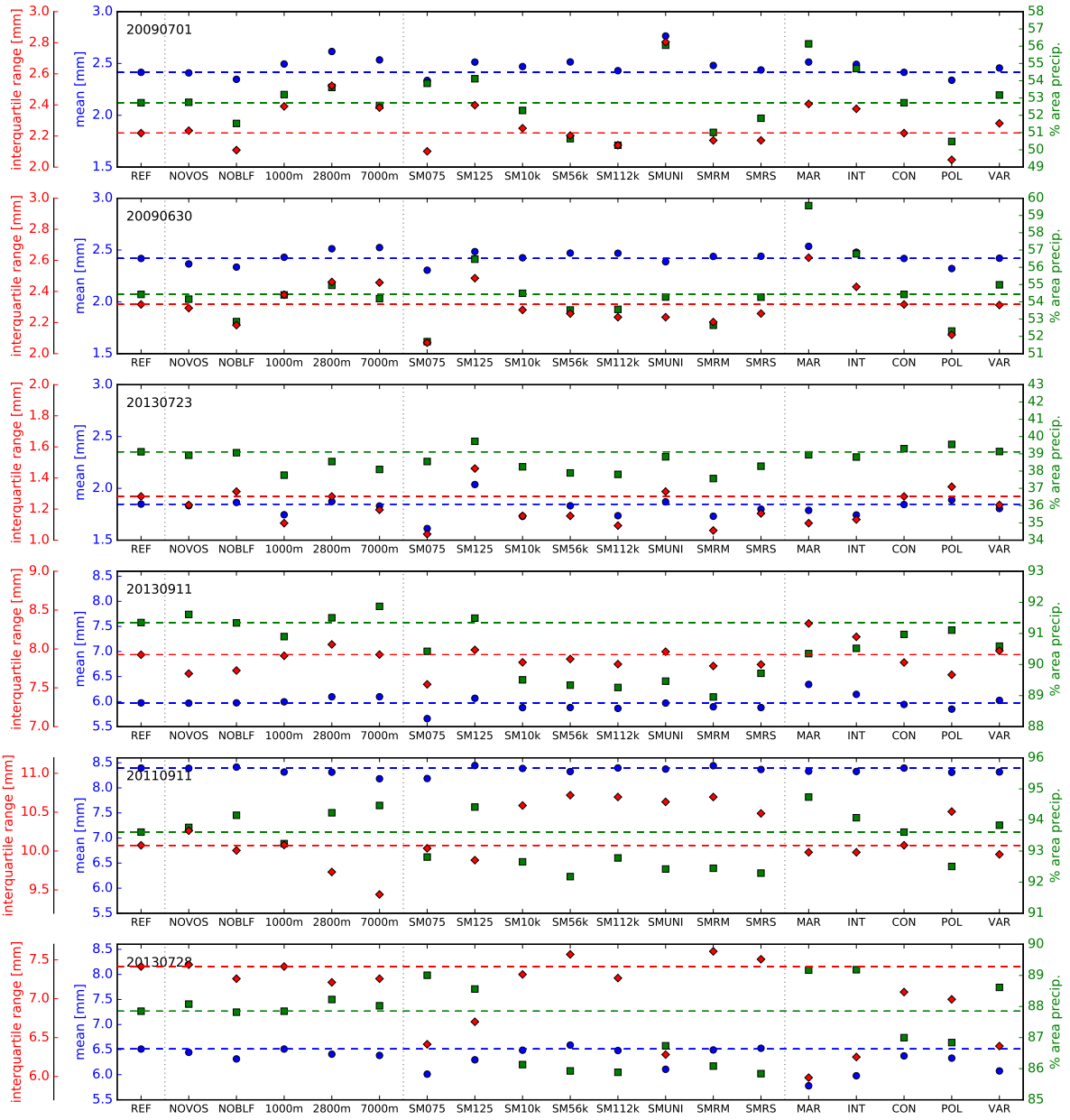

Fig. 5.5.: Mean Precipitation (circles, blue), interquartile distance (diamonds, red) and area with precipitation (squares, green) for the six investigated days. Horizontal lines are visible for better comparison and show the number that is given for the reference simulation.

soil moisture perturbations on convection and further improve the representation in models. Concluded from Figure 5.2, aerosols can impose a similar effect on precipitation as soil moisture, and Figure 5.5 shows that the maritime and the polluted simulations span the whole range of mean precipitation. This raises the question of what the combined effect of soil moisture and aerosol perturbations is, which cannot be answered here but is certainly interesting for future studies. Despite the effect of orography on mean precipitation being usually smaller than for soil moisture (Figure 5.2), the detailed analysis in

Figure 5.5 reveals that the runs with smoothed terrain (1000 m, 2800 m, 7000 m) contribute most to the uncertainty in precipitation. The reason is that within these simulations, the whole domain is perturbed, whereas the other orography perturbations only affect a small part of the domain. The interquartile range of precipitation varies between the individual simulations, but the trend follows the means surprisingly well. Thus higher mean precipitation originates in almost all cases from a broader distribution of precipitation, which is concluded from a higher interquartile range. As said earlier, the area with precipitation is influenced by soil moisture perturbations, especially under strong forcing conditions. However, also the aerosol simulations show a strong susceptibility to the area with precipitation, both under weak and strong forcing conditions, respectively. In contrast, the orography perturbations show very little effect on the area with precipitation, when analyzing the whole domain.

Changes in precipitation usually originate from changes in cloud structure. Throughout all simulations, the liquid water path changes similarly to the ice water path (Figure 5.6). Similar to the precipitation, the strongest effect can be found on the simulations with changed aerosols and soil moisture. The changes in the aerosol simulations come with no surprise as aerosols modify the amount of hydrometeors directly. New insights were found in the previous chapter regarding the importance of warm-phase or cold-phase processes in weak convective or more organized convective situations. Soil moisture simulations can change the liquid and ice water path in similar amounts as aerosols can. Unfortunately, there are no conversion rates for the soil moisture simulations available. But, it would be interesting to add the process rates and rerunning the simulations in order to gain more information about the effect of soil moisture on warm and cold phase processes. Orography influences the ice water path under weak synoptic conditions, while the liquid water path is less affected. During strong forcing conditions, orography only imposes a very small effect on the liquid and ice water path. The change in liquid or ice water path can result from an increase in the number of points where there is a cloud or because of a higher water load at the individual grid points. The liquid water path per grid point thus explains well the origin of variations in cloud water and rain. The variation in liquid water path per grid point is very small for the orography cases. For weak forcing conditions, this indicates that mostly the area with clouds is affected within these simulations. For strong forcing conditions, the change in absolute liquid water path is small in general. In runs with perturbed aerosols and soil moisture, the change in liquid water path per pixel is somewhat higher. In the aerosol simulations the amount of CCN influences the amount of hydrometeors at each grid point. In the soil moisture simulations, changes in specific humidity and/or temperatures promote different cloud growth in the vertical. In general, the change in liquid and ice water path does not always correspond to the change in precipitation. It has been found in the aerosol chapter that one reason is the evaporation of rain droplets below cloud base. This is most likely also crucial in simulations with orography and soil moisture perturbations.

These findings now allow the quantification of the relative importance of orography, soil moisture and aerosols regarding timing, amount and location of precipitation:

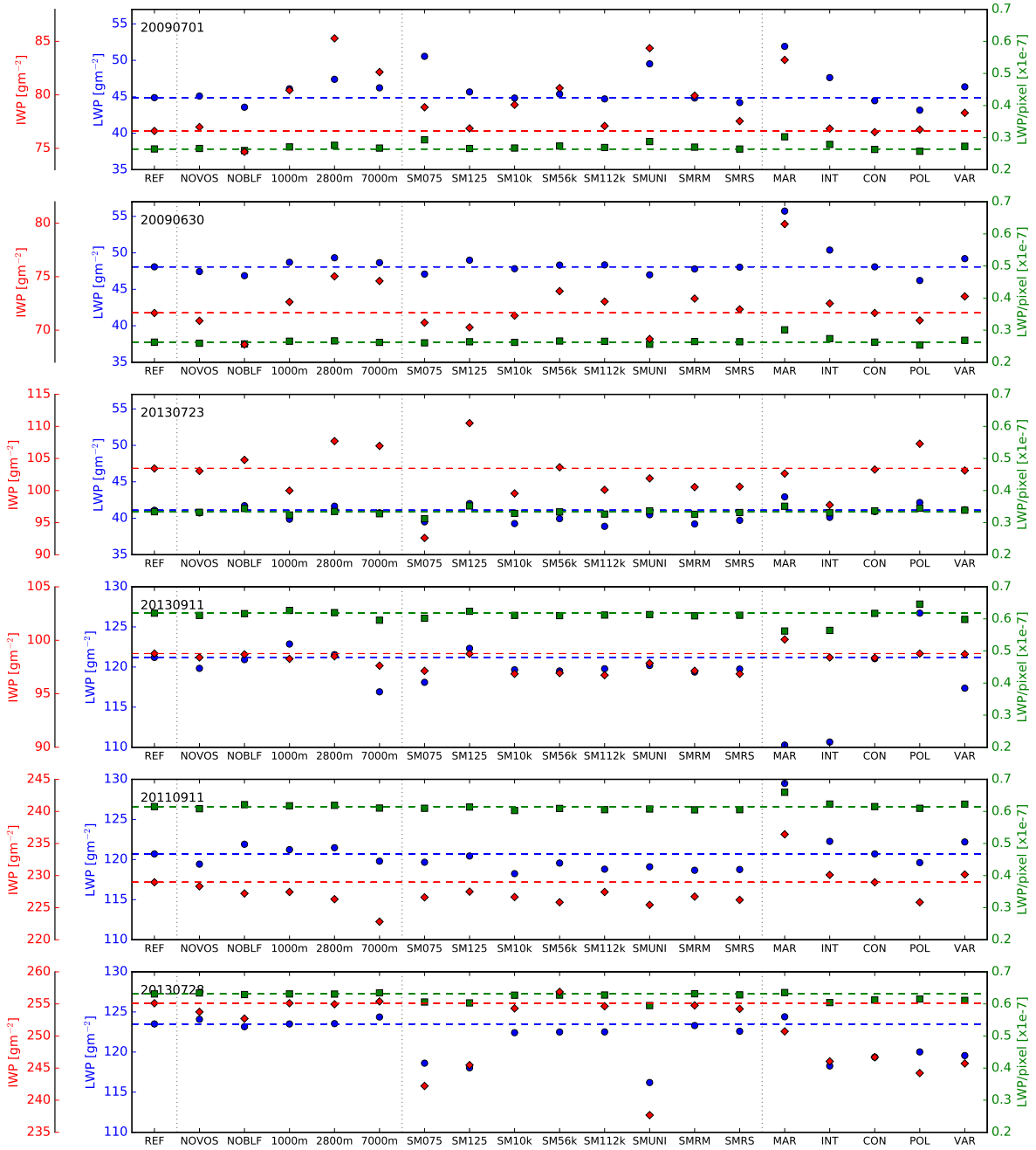

Fig. 5.6.: Mean liquid water path (circles, blue), mean ice water path (diamonds, red) and liquid water path per grid point (squares, green) for the six investigated days. Horizontal lines are visible for better comparison and show the number that is given for the reference simulation.

- The greatest variability in *precipitation amounts* is introduced by modifications in soil moisture, especially from those in which the original, heterogeneous soil moisture pattern is increased or decreased by 25%. Changes in aerosols have a similar effect on precipitation under strong synoptic forcing. Here, mostly the sensitivity to precipitation is altered due to the presence of cloud

condensation nuclei. Under weak forcing conditions, orography perturbation show on two days a greater impact than the aerosol simulations.

- The *timing of convection initiation* is not affected much by the model perturbations. Whereas soil moisture and aerosol perturbations do not impact the onset of precipitation, flattening the orography would locally delay the onset by up to two hours.

- The *location of precipitation* is modified for all perturbations. Looking at the domain average, this shift is small and almost cancels out but the distributions of precipitation difference fields show that local shifts occur in all simulations. This is most pronounced in simulations with changed orography, where locally strong differences are initiated because of missing trigger mechanisms. The location of near-surface convergence zones strongly determines where precipitation is initiated. Whether or not convergence zones establish depends on the underlying terrain and thermal differences close to the surface. Here, mountains play a crucial role as they naturally modify the near-surface wind field and mainly influence when and were convection forms. Also pronounced gradients in soil moisture can establish local convergence zones due to thermal differences at the surface.

The results of this study provide suggestion for improvements in current weather forecasting systems. Ensembles provide a valuable tool for quantitative precipitation forecast. While increasing model resolution is more beneficial at very short ranges, increasing the ensemble size has a larger impact at longer forecast ranges, as predictability decreases and more members are required to better sample the larger uncertainty (Raynaud and Bouttier, 2017). The coming years are likely to see a further increase in the use of ensemble methods in forecasts and assimilation which will put increasing demands on the methods used to perturb the model (Leutbecher et al., 2016). Usually, these ensembles consist of members with different initial conditions, different boundary conditions and various physical parameters, like soil moisture. Ensemble members should show a broad spread to cover a variety of situations but the strength of perturbation should -if possible- also be comparable to observations. From this analysis, two set of simulations could be used as ensemble members. First, the runs with incrementally smoothed terrain, as they represent conditions when increasing model resolution does not go along with increasing resolution of external data. Second, the simulations with soil moisture biases, as they are in the order of measurement uncertainties. The results show that flattening the orography has a small, but locally important effect on precipitation and that these perturbations could very well be added to existing ensembles as a new set of members. Soil moisture perturbations within the order of 15% are already part of the COSMO-EPS ensemble (Schraff et al., 2016) used operationally. This study emphasizes the important uncertainty that is introduced by soil moisture perturbations into the model and suggests to keep or even extend existing soil moisture perturbations in ensembles. The simulations with homogeneous aerosol concentrations represent a simplification but are very common to use in most numerical weather prediction models. The results from these study show that the spatial heterogeneity is important and can change precipitation

amounts locally. Despite seeing a pronounced local but weak effect with heterogeneous aerosol fields, which would support the idea of an ensemble member, it is suggested to further investigate the effect of spatially variable aerosol fields.

Despite the comprehensive analysis and the extensive dataset gathered in this study, open questions still remain. Below are propositions, listed in decreasing order of importance, how this work could be continued to further work on the uncertainties that model perturbations have on precipitation.

- Because this study did not show consistent results for all of the six days studied, it can be assumed that the sample size of six days is not sufficiently large. But because of the high-resolution that was used and hence the high computational costs, the number of days was restricted to six. It is desired to run more simulations and then apply statistical analysis methods. This would allow statistically significant results to be found and to find more specific trends, i.e. whether a particular weather situation leads to a specific precipitation response. For example, in the simulations with perturbed aerosols it would be good to find an updraft velocity that determines whether warm-phase or cold-phase processes dominate. Similarly, in the runs with soil moisture perturbations it would be worth investigating how the soil moisture – precipitation feedback changes with small changes in the initial soil moisture content. Ideally, the number of days is increased 20 or more. This allows the separation of the days according to their environmental conditions and still maintain a sufficient sample size. From the findings of this study, it is suggested to focus on weak forcing days, as the interaction between land and atmosphere is more pronounced, while on strong forcing days, the large-scale synoptic situation strongly controls the precipitation pattern. When increasing the number of days of investigation, then this requires either a reduction in the domain size or a coarser model resolution. The results of this study suggest that high-resolution numerical simulations allow to better resolve small-scale features, like convergence zones. Hence the suggestion would be to use at least a resolution of 1 km and then adjust the domain size such that computational costs are reasonable.

- Until now individual days have been investigated. Since forecast errors often amplify with increasing forecast hours and after periods of convective weather (Rodwell et al., 2013), it is of interest to increase the simulated time period. This would allow the quantification of the short- and longterm effects and forecast error of perturbations.

- The results show that soil moisture and aerosols can have a similar effect on the mean precipitation. It remains totally open how these two contributors interact together and hence it is proposed to performed combined sensitivities. Therefore, the individual effects need to be analyzed first and then in a second step they can be varied both at the same time. With such an analysis it could be answered whether the two convection-influencing parameters amplify or compete, e. g. aerosol simulations showed increasing precipitation amounts with increasing CCN on days with strong

vertical exchange and dry atmosphere, whereas these environmental conditions lead in case of soil moisture perturbations to a reduction in precipitation.

- It was evident from these results that environmental conditions impact the response of orography, soil moisture and aerosol perturbations on precipitation. Therefore the days of investigation often showed different results. As already mentioned earlier, increasing the amount of simulated days would allow to better characterize the effect of different environmental conditions. In addition, a study with explicitly changed environmental conditions would be very helpful. For the case of soil moisture perturbations, one suggestion would be to incrementally change the initial soil moisture content in smaller steps, as this strongly affects the evapotranspiration and boundary layer development. For further studying the effect of different aerosols under various environmental conditions, it is suggested to change the updraft velocity, e. g. by changing the stability of the atmosphere.

- One aspect in the characterization of precipitation that could be extended is the spatial distribution of precipitation. It is suggested to further investigate precipitation structures on half-hourly intervals, for example by means of SAL-diagrams (Wernli et al., 2008). This would allow the quantification of the dominant spatial scales at which orography, soil moisture and aerosols impact precipitation.

- For the orography perturbations, individual valleys were flattened and two mountain ranges smoothed locally. This work could be extended by incrementally flattening the terrain within the whole domain, e. g. reduction by 10%, but keeping a detailed terrain structure. This allows for a more comprehensive view of orographic effects on cloud formation and precipitation in various regions and, most importantly, allows a better intercomparison regarding other sources of uncertainty also applied to the entire model domain (soil moisture and microphysical uncertainties).

A. List of Figures

B. List of Tables

C. Bibliography

Albrecht, B. A., 1989: Aerosols, cloud microphysics, and fractional cloudiness. *Science*, **245 (4923)**, 1227–1230.

Altaratz, O., I. Koren, T. Reisin, A. Kostinski, G. Feingold, Z. Levin, and Y. Yin, 2008: Aerosols' influence on the interplay between condensation, evaporation and rain in warm cumulus cloud. *Atmos. Chem. Phys.*, **8 (1)**, 15–24.

Altaratz, O., I. Koren, L. Remer, and E. Hirsch, 2014: Review: Cloud invigoration by aerosols: Coupling between microphysics and dynamics. *Atmos. Res.*, **140-141**, 38 – 60.

Baldauf, M., A. Seifert, J. Förstner, D. Majewski, and M. Raschendorfer, 2011: Operational convective-scale numerical weather prediction with the COSMO model: description and sensitivities. *Mon. Wea. Rev.*, **139**, 3887–3905.

Bangert, M., C. Kottmeier, B. Vogel, and H. Vogel, 2011: Regional scale effects of the aerosol cloud interaction simulated with an online coupled comprehensive chemistry model. *Atmos. Chem. Phys.*, **11 (9)**, 4411–4423.

Barrett, A. I., S. L. Gray, D. J. Kirshbaum, N. M. Roberts, D. M. Schultz, and J. G. Fairman, 2015: Synoptic versus orographic control on stationary convective banding. *Q. J. R. Meteorol. Soc.*, **141 (689)**, 1101–1113.

Barthlott, C., B. Adler, N. Kalthoff, J. Handwerker, M. Kohler, and A. Wieser, 2016: The role of Corsica in initiating nocturnal offshore convection. *Q. J. R. Meteorol. Soc.*, **142**, 222–237.

Barthlott, C., R. Burton, D. Kirshbaum, K. Hanley, E. Richard, J.-P. Chaboureau, J. Trentmann, B. Kern, H.-S. Bauer, T. Schwitalla, C. Keil, Y. Seity, A. Gadian, A. Blyth, S. Mobbs, C. Flamant, and J. Handwerker, 2011a: Initiation of deep convection at marginal instability in an ensemble of mesoscale models: a case-study from COPS. *Q. J. R. Meteorol. Soc.*, **137 (S1)**, 118–136.

Barthlott, C., C. Hauck, G. Schädler, N. Kalthoff, and C. Kottmeier, 2011b: Soil moisture impacts on convective indices and precipitation over complex terrain. *Meteorol. Z.*, **20 (2)**, 185–197.

Barthlott, C. and C. Hoose, 2015: Spatial and temporal variability of clouds and precipitation over Germany: multiscale simulations across the "gray zone". *Atmos. Chem. Phys.*, **15 (21)**, 12 361–12 384.

———, 2018: Aerosol effects on clouds and precipitation over central Europe in different weather regimes. *J. Atmos. Sci.*, doi: 10.1175/JAS–D–18–0110.1.

Barthlott, C., B. Mühr, and C. Hoose, 2017: Sensitivity of the 2014 Pentecost storms over Germany to different model grids and microphysics schemes. *Q. J. R. Meteorol. Soc.*, **143 (704)**, 1485–1503.

Baur, F., C. Keil, and G. Craig, 2018: Soil Moisture - Precipitation Coupling over Central Europe: Interactions between surface anomalies at different scales and its dynamical implication. *Q. J. R. Meteorol. Soc.*, doi:10.1002/qj.3415.

Behrendt, A., S. Pal, F. Aoshima, M. Bender, A. Blyth, U. Corsmeier, J. Cuesta, G. Dick, M. Dorninger, C. Flamant, P. Di Girolamo, T. Gorgas, Y. Huang, N. Kalthoff, S. Khodayar, H. Mannstein, K. Träumner, A. Wieser, and V. Wulfmeyer, 2011: Observation of convection initiation processes with a suite of state-of-the-art research instruments during COPS IOP8b. *Q. J. R. Meteorol. Soc.*, **137 (S1)**, 81–100.

Bennett, L. J., A. M. Blyth, R. R. Burton, A. M. Gadian, T. M. Weckwerth, A. Behrendt, P. Di Girolamo, M. Dorninger, S.-J. Lock, V. H. Smith, and S. D. Mobbs, 2011: Initiation of convection over the Black Forest mountains during COPS IOP15a. *Q. J. R. Meteorol. Soc.*, **137 (S1)**, 176–189.

Bennett, L. J., K. A. Browning, A. M. Blyth, D. J. Parker, and P. A. Clark, 2006: A review of the initiation of precipitating convection in the United Kingdom. *Q. J. R. Meteorol. Soc.*, **132**, 1001–1020.

Bontemps, S., P. Defourny, E. V. Bogaert, O. Arino, V. Kalogirou, and J. R. Perez, 2011: GLOBCOVER 2009 - Products description and validation report. Tech. rep., Université catholique de Louvain (UCL) and European Space Agency (ESA).

Brocca, L., S. Hasenauer, T. Lacava, F. Melone, T. Moramarco, W. Wagner, W. Dorigo, P. Matgen, J. Martínez-Fernández, P. Llorens, J. Latron, C. Martin, and M. Bittelli, 2011: Soil moisture estimation through ASCAT and AMSR-E sensors: An intercomparison and validation study across Europe. *Remote Sensing of Environment*, **115 (12)**, 3390 – 3408.

Bryan, G. H. and J. M. Fritsch, 2000: Moist absolute instability: The sixth static stability state. *Bull. Amer. Meteor. Soc.*, **81 (6)**, 1207–1230.

Burt, S., 2005: Cloudburst upon Hendraburnick Down: The Boscastle storm of 16 August 2004. *Weather*, **60 (8)**, 219–227.

Burton, R. R., A. Gadian, A. M. Blyth, and S. D. Mobbs, 2013: Modelling isolated deep convection: A case study from COPS. *Meteorol. Z.*, **22**, 433–443.

Buzzi, A., N. Tartaglione, and P. Malguzzi, 1998: Numerical simulations of the 1994 Piedmont flood: Role of orography and moist processes. *Mon. Wea. Rev.*, **126**, 2369–2383.

Carbone, R. E., J. Tuttle, D. Ahijevych, and S. Trier, 2002: Inferences of Predictability associated with Warm Season Precipitation Episodes. *J. Atmos. Sci.*, **59**, 2033–2056.

Cheng, W. Y. Y. and W. R. Cotton, 2004: Sensitivity of a Cloud-Resolving Simulation of the Genesis of a Mesoscale Convective System to Horizontal Heterogeneities in Soil Moisture Initialization. *J. Hydrometeor.*, **5 (5)**, 934–958.

Cioni, G. and C. Hohenegger, 2017: Effect of soil moisture on diurnal convection and precipitation in large-eddy simulations. *J. Hydrometeor.*, **18 (7)**, 1885–1903.

Clark, P., N. Roberts, H. Lean, S. P. Ballard, and C. Charlton-Perez, 2016: Convection-permitting models: a step-change in rainfall forecasting. *Meteorological Applications*, **23 (2)**, 165–181.

Doms, G., J. Förstner, E. Heise, H.-J. Herzog, D. Mironov, M. Raschendorfer, T. Reinhardt, B. Ritter, R. Schrodin, J.-P. Schulz, and G. Vogel, 2011: A description of the nonhydrostatic regional COSMO model, Part II: Physical Parameterization.

Dorigo, W., A. Gruber, R. D. Jeu, W. Wagner, T. Stacke, A. Loew, C. Albergel, L. Brocca, D. Chung, R. Parinussa, and R. Kidd, 2015: Evaluation of the ESA CCI soil moisture product using ground-based observations. *Remote Sensing of Environment*, **162**, 380 – 395.

Ehmele, F., C. Barthlott, and U. Corsmeier, 2015: The influence of Sardinia on Corsican rainfall in the western Mediterranean Sea: A numerical sensitivity study. *Atmos. Res.*, **153**, 451–464.

Etling, D. and R. A. Brown, 1993: Roll vortices in the planetary boundary layer: A review. *Boundary-Layer Meteorol.*, **65 (3)**, 215–248.

Fan, J., L. R. Leung, D. Rosenfeld, Q. Chen, Z. Li, J. Zhang, and H. Yan, 2013: Microphysical effects determine macrophysical response for aerosol impacts on deep convective clouds. *Proc. Nat. Academy Sci.*, **110 (48)**, E4581–E4590.

Fan, J., Y. Wang, D. Rosenfeld, and X. Liu, 2016: Review of Aerosol–Cloud Interactions: Mechanisms, Significance, and Challenges. *J. Atmos. Sci.*, **73 (11)**, 4221–4252.

Feingold, G., W. L. Eberhard, D. E. Veron, and M. Previdi, 2003: First measurements of the Twomey indirect effect using ground-based remote sensors. *Geophys. Res. Lett.*, **30 (6)**.

Findell, K. L. and E. A. B. Eltahir, 2003: Atmospheric controls on soil moisture-boundary layer interactions. {P}art {I}: {F}ramework development. *J. Hydrometeor.*, **4**, 552–569.

Fletcher, H., 1962: *The physics of rainclouds*. Cambridge University Press.

Friedlander, S. K., 2000: *Smoke, Dust and Hail. Fundamentals of Aerosol Dynamics, second Edition*. Oxford University Press.

Fritsch, J. M. and R. E. Carbone, 2004: Improving quantitative precipitation forecasts in the warm season: A USWRP research and development strategy. *Bull. Amer. Meteor. Soc*, **85 (7)**, 955–965.

Froidevaux, P., L. Schlemmer, J. Schmidli, W. Langhans, and C. Schär, 2014: Influence of the background wind on the local soil moisture–precipitation feedback. *J. Atmos. Sci.*, **71 (2)**, 782–799.

Gilgen, H., M. Wild, and A. Ohmura, 1998: Means and Trends of Shortwave Irradiance at the Surface Estimated from Global Energy Balance Archive Data. *J. Climate*, **11 (8)**, 2042–2061.

Groenemeijer, P., C. Barthlott, A. Behrendt, U. Corsmeier, J. Handwerker, M. Kohler, C. Kottmeier, H. Mahlke, S. Pal, M. Radlach, J. Trentmann, A. Wieser, and V. Wulfmeyer, 2009: Observations of kinematics and thermodynamic structure surrounding a convective storm cluster over a low mountain range. *Mon. Wea. Rev.*, **137**, 585–602.

Guillod, B. P., B. Orlowsky, D. Miralles, A. J. Teuling, P. D. Blanken, N. Buchmann, P. Ciais, M. Ek, K. L. Findell, P. Gentine, B. R. Lintner, R. L. Scott, B. Van den Hurk, and S. I. Seneviratne, 2014: Land-surface controls on afternoon precipitation diagnosed from observational data: uncertainties and confounding factors. *Atmos. Chem. Phys.*, **14 (16)**, 8343–8367.

Hande, L. B., C. Engler, C. Hoose, and I. Tegen, 2016: Parameterising Cloud Condensation Nuclei concentrations during HOPE. *Atmos. Chem. Phys.*

Hansen, J., M. Sato, and R. Ruedy, 1997: Radiative forcing and climate response. *J. Geophys. Res.: Atmospheres*, **102 (D6)**, 6831–6864.

Hauck, C., C. Barthlott, L. Krauss, and N. Kalthoff, 2011: Soil moisture variability and its influence on convective precipitation over complex terrain. *Q. J. R. Meteorol. Soc.*, **137 (S1)**, 42–56.

Haywood, J. and O. Boucher, 2000: Estimates of the direct and indirect radiative forcing due to tropospheric aerosols: A review. *Rev. Geophys.*, **38 (4)**, 513–543.

Heinze, R., A. Dipankar, C. C. Henken, C. Moseley, O. Sourdeval, S. Trömel, X. Xie, P. Adamidis, F. Ament, H. Baars, C. Barthlott, A. Behrendt, U. Blahak, S. Bley, S. Brdar, M. Brueck, S. Crewell, H. Deneke, P. Di Girolamo, R. Evaristo, J. Fischer, C. Frank, P. Friederichs, T. Göcke, K. Gorges, L. Hande, M. Hanke, A. Hansen, H.-C. Hege, C. Hoose, T. Jahns, N. Kalthoff, D. Klocke, S. Kneifel, P. Knippertz, A. Kuhn, T. van Laar, A. Macke, V. Maurer, B. Mayer, C. I. Meyer, S. K. Muppa, R. A. J. Neggers, E. Orlandi, F. Pantillon, B. Pospichal, N. Röber, L. Scheck, A. Seifert, P. Seifert, F. Senf, P. Siligam, C. Simmer, S. Steinke, B. Stevens, K. Wapler, M. Weniger, V. Wulfmeyer, G. Zängl, D. Zhang, and J. Quaas, 2017: Large-eddy simulations over germany using icon: a comprehensive evaluation. *Q. J. R. Meteorol. Soc.*, **143 (702)**, 69–100.

Hohenegger, C., P. Brockhaus, C. S. Bretherton, and C. Schär, 2009: The soil moisture-precipitation feedback in simulations with explicit and parameterized convection. *J. Climate*, **22 (19)**, 5003–5020.

Hohenegger, C. and C. Schär, 2007: Predictability and Error Growth Dynamics in Cloud-Resolving Models. *J. Atmos. Sci.*, **64 (12)**, 4467–4478.

Hoose, C. and O. Möhler, 2012: Heterogeneous ice nucleation on atmospheric aerosols: a review of results from laboratory experiments. *Atmos. Chem. Phys.*, **12 (20)**, 9817–9854.

Igel, A. L., M. R. Igel, and S. C. van den Heever, 2015: Make It a Double? Sobering Results from Simulations Using Single-Moment Microphysics Scheme. *J. Atmos. Sci.*, **72**, 910–925.

Imamovic, A., L. Schlemmer, and C. Schär, 2017: Collective impacts of orography and soil moisture on the soil moisture–precipitation feedback. *Geophys. Res. Lett.*, **44 (22)**, 11,682–11,691.

IPCC, 2007: Forster, P., V. Ramaswamy, P. Artaxo, T. Berntsen, R. Betts, D. Fahey, J. Haywood, J. Lean, D. Lowe, G. Myhre, J. Nganga, R. Prinn, G. Raga, M. Schulz, and R. Van Dorland, 2007: Climate Change 2007: The Physical Science Basis. Contribution of Working Group I to the Fourth Assessment Report of the Intergovernmental Panel on Climate Change. [Solomon, S. and Qin, D. and Manning, M. and Chen, Z. and Marquis, M. and Averyt, K.B. and Tignor, M. and Miller, H.L. (eds.)], Cambridge, United Kingdom and New York, NY, USA.

IPCC, 2013: Stocker, T., D. Qin, G.-K. Plattner, L. Alexander, S. S.K. Allen, N. N.L. Bindoff, F.-M. F.-M. Bréon, U. J.A. Church, J.A.and Cubasch, S. Emori, P. Forster, P. Friedlingstein, N. Gillett, J. Gregory, D. Hartmann, E. Jansen, B. Kirtman, R. Knutti, K. Krishna Kumar, P. Lemke, J. Marotzke, V. Masson-Delmotte, G. Meehl, I. Mokhov, S. Piao, V. Ramaswamy, D. Randall, M. Rhein, M. Rojas, C. Sabine, D. Shindell, L. Talley, V. D. G., and S.-P. Xie, 2013: Technical summary. [Stocker, T.F. and Qin, D. and Plattner, G.-K. and Alexander, L.V. and Allen, S.K. and Boschung, J. and Nauels, A. and Xia, Y. and Bex, V. and Midgley, P.M. (eds.)], Cambridge, United Kingdom and New York, NY, USA, 33–115 pp.

Jahn, M., 2015: Economics of extreme weather events: Terminology and regional impact models. *Wea. and Clim. Extremes*, **10**, 29 – 39.

Kalthoff, N., B. Adler, C. Barthlott, U. Corsmeier, S. Mobbs, S. Crewell, K. Träumner, C. Kottmeier, A. Wieser, and V. Smith, 2009: The impact of convergence zones on the initiation of deep convection: A case study from COPS. *Atmos. Res.*, **93**, 680–694.

Kang, S.-L. and G. H. Bryan, 2011: A large-eddy simulation study of moist convection initiation over heterogeneous surface fluxes. *Mon. Wea. Rev.*, **139 (9)**, 2901–2917.

Keil, C. and G. C. Craig, 2011: Regime-dependent forecast uncertainty of convective precipitation. *Meteorol. Z.*, **20 (2)**, 145–151.

Khain, A. P., N. BenMoshe, and A. Pokrovsky, 2008: Factors Determining the Impact of Aerosols on Surface Precipitation from Clouds: An Attempt at Classification. *J. Atmos. Sci.*, **65**, 1721–1748.

Khain, A. P. and A. Pokrovsky, 2004: Simulation of effects of atmospheric aerosols on deep turbulent convective clouds using a spectral microphysics mixed-phase cumulus cloud model. *J. Atmos. Sci.*, **61**, 2983–3001.

Kirshbaum, D. J., B. Adler, N. Kalthoff, C. Barthlott, and S. Serafin, 2018: Moist orographic convection: Physical mechanisms and links to surface-exchange processes. *Atmosphere*, **9 (3)**.

Kirshbaum, D. J., G. H. Bryan, R. Rotunno, and D. R. Durran, 2007: The triggering of orographic rainbands by small-scale topography. *J. Atmos. Sci.*, **64**, 1530–1549.

Kirshbaum, D. J. and D. R. Durran, 2005: Observations and Modeling of Banded Orographic Convection. *J. Atmos. Sci.*, **62 (5)**, 1463–1479.

Köhler, H., 1936: The nucleus in and the growth of hygroscopic droplets. *Trans. Faraday Soc.*, **32**, 1152–1161.

Kottmeier, C., N. Kalthoff, C. Barthlott, U. Corsmeier, J. Van Baelen, A. Behrendt, R. Behrendt, A. Blyth, R. Coulter, S. Crewell, P. Di Girolamo, M. Dorninger, C. Flamant, T. Foken, M. Hagen, C. Hauck, H. Höller, H. Konow, M. Kunz, H. Mahlke, S. Mobbs, E. Richard, R. Steinacker, T. Weckwerth, A. Wieser, and V. Wulfmeyer, 2008: Mechanisms initiating deep convection over complex terrain during COPS. *Meteorol. Z.*, **17**, 931–948.

Krauss, L., C. Hauck, and C. Kottmeier, 2010: Spatio-temporal soil moisture variability in southwest germany observed with a new monitoring network within the cops domain. *Meteorol. Z.*, **19 (6)**, 523–537.

Kühnlein, C., C. Keil, G. C. Craig, and C. Gebhardt, 2014: The impact of downscaled initial condition perturbations on convective-scale ensemble forecasts of precipitation. *Q. J. R. Meteorol. Soc.*, **140**, 1552–1562.

Lamb, D. and J. Verlinde, 2011: *Cloud microphysics*, 275–276. Cambridge University Press.

Langhans, W., A. Gohm, and G. Zängl, 2011: The orographic impact on patterns of embedded convection during the August 2005 Alpine flood. *Q. J. R. Meteorol. Soc.*, **137 (661)**, 2092–2105.

Lebo, Z. J., H. Morrison, and J. H. Seinfeld, 2012: Are simulated aerosol-induced effects on deep convective clouds strongly dependent on saturation adjustment? *Atmos. Chem. Phys.*, **12 (20)**, 9941–9964.

Leutbecher, M., S.-J. Lock, P. Ollinaho, S. T. K. Lang, and al et, 2016: Stochastic representations of model uncertainties at ecmwf: State of the art and future vision. *ECMWF Technical Memorandum*, **143 (785)**.

Lohmann, U. and J. Feichter, 2005: Global indirect aerosol effects: a review. *Atmos. Chem. Phys.*, **5 (3)**, 715–737.

Meißner, C., N. Kalthoff, M. Kunz, and G. Adrian, 2007: Initiation of shallow convection in the Black Forest mountains. *Atmos. Res.*, **86 (1)**, 42 – 60.

Mellor, G. L. and T. Yamada, 1974: A hierarchy of turbulence closure models for planetary boundary layers. *J. Atmos. Sci.*, **31**, 1791–1806.

Miltenberger, A. K., P. R. Field, A. A. Hill, P. Rosenberg, B. J. Shipway, and J. M. Wilkinson, 2018: Aerosol–cloud interactions in mixed-phase convective clouds – Part 1: Meteorological ensemble. *Atmos. Chem. Phys.*, **18 (14)**, 10 593–10 613.

Mittermaier, M. P., 2014: A strategy for verifying near-convection-resolving model forecasts at observing sites. *Wea. and Forec.*, **29 (2)**, 185–204.

Muhlbauer, A. and U. Lohmann, 2008: Sensitivity studies of the role of aerosols in warm-phase orographic precipitation in different dynamical flow regimes. *J. Atmos. Sci.*, **65 (8)**, 2522–2542.

Neggers, R. A. J., H. J. J. Jonker, and A. P. Siebesma, 2003: Size statistics of cumulus cloud populations in large-eddy simulations. *J. Atmos. Sci.*, **60 (8)**, 1060–1074.

Noppel, H., U. Blahak, A. Seifert, and K. D. Beheng, 2010: Simulations of a hailstorm and the impact of CCN using an advanced two-moment cloud microphysical scheme. *Atmos. Res.*, **96**, 286–301.

Pan, Z., E. Takle, M. Segal, and R. Turner, 1996: Influences of model parameterization schemes on the response of rainfall to soil moisture in the central United States. *Mon. Wea. Rev.*, **124**, 1786–1802.

Penner, J. E., X. Dong, and Y. Chen, 2004: Observational evidence of a change in radiative forcing due to the indirect aerosol effect. *Nature*, **427**, 231–234.

Piper, D. and M. Kunz, 2017: Spatiotemporal variability of lightning activity in europe and the relation to the north atlantic oscillation teleconnection pattern. *Nat. Hazards Earth Syst. Sci.*, **17 (8)**, 1319–1336.

Planche, C., G. W. Mann, K. S. Carslaw, M. Dalvi, J. H. Marsham, and P. R. Field, 2017: Spatial and temporal ccn variations in convection-permitting aerosol microphysics simulations in an idealised marine tropical domain. *Atmos. Chem. Phys.*, **17 (5)**, 3371–3384.

Raymond, D. and W. Marvin, 1980: Mountain-Induced Convection under Fair Weather Conditions. *J. Atmos. Sci.*, **37**, 2693–2700.

Raynaud, L. and F. Bouttier, 2017: The impact of horizontal resolution and ensemble size for convective-scale probabilistic forecasts. *Q. J. R. Meteorol. Soc.*, **143 (709)**, 3037–3047.

Rieck, M., C. Hohenegger, and C. C. van Heerwaarden, 2014: The influence of land surface heterogeneities on cloud size development. *Mon. Wea. Rev.*, **142 (10)**, 3830–3846.

Rihani, J. F., F. K. Chow, and R. M. Maxwell, 2015: Isolating effects of terrain and soil moisture heterogeneity on the atmospheric boundary layer: Idealized simulations to diagnose land-atmosphere feedbacks. *J. of Adv. in Modeling Earth Sys.*, **7 (2)**, 915–937.

Rochetin, N., F. Couvreux, and F. Guichard, 2017: Morphology of breeze circulations induced by surface flux heterogeneities and their impact on convection initiation. *Q. J. R. Meteorol. Soc.*, **143 (702)**, 463–478.

Rodwell, M. J., L. Magnusson, P. Bauer, P. Bechtold, M. Bonavita, C. Cardinali, M. Diamantakis, P. Earnshaw, A. Garcia-Mendez, L. Isaksen, E. Källén, D. Klocke, P. Lopez, T. McNally, A. Persson, F. Prates, and N. Wedi, 2013: Characteristics of occasional poor medium-range weather forecasts for europe. *Bull. Amer. Meteor. Soc.*, **94 (9)**, 1393–1405.

Rogers, R. R. and M. K. Yau, 1989: *Short Course in Cloud Physics*. Pergamon, Tarrytown, N. Y.

Rosenfeld, D., U. Lohmann, G. B. Raga, C. D. O'Dowd, M. Kulmala, S. Fuzzi, A. Reissell, and M. O. Andreae, 2008: Flood or Drought: How Do Aerosols Affect Precipitation? *Science*, **321**, 1309–1313.

Rossa, A., M. Bruen, D. Frühwald, B. Macpherson, I. Holleman, D. Michelson, and S. Michaelides, 2005: Use of Radar Observations in Hydrological and NWP Models.

Rotunno, R. and R. Ferretti, 2001: Mechanisms of intense alpine rainfall. *J. Atmos. Sci.*, **58**, 1732–1749.

Rotunno, R. and R. A. Houze, 2007: Lessons on orographic precipitation from the Mesoscale Alpine Programme. *Q. J. R. Meteorol. Soc.*, **133 (625)**, 811–830.

Santanello, J. A., P. A. Dirmeyer, C. R. Ferguson, K. L. Findell, A. B. Tawfik, A. Berg, M. Ek, P. Gentine, B. P. Guillod, C. van Heerwaarden, J. Roundy, and V. Wulfmeyer, 2018: Land-atmosphere interactions: The loco perspective. *Bull. Amer. Meteor. Soc.*, **99 (6)**, 1253–1272.

Saucier, W. J., 1955: *Principles of Meteorological Analysis*. University of Chicago Press: Chicago, IL, USA.

Schättler, U., 2016: A description of the nonhydrostatic regional COSMO-model, Part V: Preprocessing: Initial and Boundary Data for the COSMO-Model.

Schättler, U., G. Doms, and C. Schraff, 2016: A description of the nonhydrostatic regional COSMO-model, Part VII: User's Guide.

Schneider, L., C. Barthlott, A. I. Barrett, and C. Hoose, 2018: The precipitation response to variable terrain forcing over low mountain ranges in different weather regimes. *Q. J. R. Meteorol. Soc.*, **144 (713)**, 970–989.

Schraff, C., H. Reich, A. Rhodin, A. Schomburg, K. Stephan, A. Periáñez, and R. Potthast, 2016: Kilometre-scale ensemble data assimilation for the cosmo model (kenda). *Q. J. R. Meteorol. Soc.*, **142 (696)**, 1453–1472.

Schumacher, R. S., D. M. Schultz, and J. A. Knox, 2015: Influence of Terrain Resolution on Banded Convection in the Lee of the Rocky Mountains. *Mon. Wea. Rev.*, **143 (4)**, 1399–1416.

Schwitalla, T., H.-S. Bauer, V. Wulfmeyer, and G. Zängl, 2008: Systematic errors of QPF in low-mountain regions as revealed by MM5 simulations. *Meteorol. Z.*, **17**, 903–919.

Segal, Y. and A. Khain, 2006: Dependence of droplet concentration on aerosol conditions in different cloud types: application to droplet concentration parameterization of aerosol conditions. *J. Geophy. Res.*, **111**, D15 240.

Seifert, A. and K. D. Beheng, 2006: A two-moment cloud microphysics parameterization for mixed-phase clouds. Part I: Model description. *Meteorol. Atmos. Phys.*, **92**, 45–66.

Seifert, A., C. Köhler, and K. D. Beheng, 2012: Aerosol-cloud-precipitation effects over Germany as simulated by a convective-scale numerical weather prediction model. *Atmos. Chem. Phys.*, **12**, 709–725.

Selz, T. and G. C. Craig, 2015: Upscale error growth in a high-resolution simulation of a summertime weather event over europe. *Mon. Wea. Rev.*, **143 (3)**, 813–827.

Seneviratne, S., D. Lüthi, M. Litschi, and C. Schär, 2006: Land-atmosphere coupling and climate change in Europe. *Nature*, **443**, 205–209.

Sheffield, J., E. Wood, and R. M, 2012: Little change in global drought over the past 60 years. *Nature*, **491**, 435–438.

Shrestha, R. K., P. J. Connolly, and M. W. Gallagher, 2017: Sensitivity of Precipitation to Aerosol and Temperature Perturbation over the Foothills of the Nepal Himalayas. *Proceedings*, **1 (5)**, 144.

Smith, V., S. Mobbs, R. Burton, M. Hobby, F. Aoshma, V. Wulfmeyer, and P. Girolamo, 2015: The role of orography in the regeneration of convection: A case study from the convective and orographically-induced precipitation study. *Meteorol. Z.*, **24 (1)**, 83–97.

Spreafico, M., 2006: Flash floods in mountain areas. *IAHS-AISH Publication*, **308**, 232–238.

Stevens, B. and G. Feingold, 2009: Untangling aerosol effects on clouds and precipitation in a buffered system. *Nature*, **461**, 607–613.

Storer, R. L. and S. C. van den Heever, 2013: Microphysical processes evident in aerosol forcing of tropical deep convective clouds. *J. Atmos. Sci.*, **70 (2)**, 430–446.

Storer, R. L., S. C. van den Heever, and G. L. Stephens, 2010: Modeling aerosol impacts on convective storms in different environments. *J. Atmos. Sci.*, **67 (12)**, 3904–3915.

Tao, W.-K., J.-P. Chen, Z. Li, C. Wang, and C. Zhang, 2012: Impact of aerosols on convective clouds and precipitation. *Rev. Geophys*, **50**.

Tao, W.-K. and X. Li, 2016: The relationship between latent heating, vertical velocity, and precipitation processes: The impact of aerosols on precipitation in organized deep convective systems. *J. Geophys. Res.: Atmospheres*, **121 (11)**, 6299–6320.

Tao, W.-K., X. Li, A. Khain, T. Matsui, S. Lang, and J. Simpson, 2007: Role of atmospheric aerosol concentration on deep convective precipitation: Cloud–resolving model simulations. *J. Geophys. Res.: Atmospheres*, **112 (D24)**.

Taylor, C. M., C. E. Birch, D. J. Parker, N. Dixon, F. Guichard, G. Nikulin, and G. M. S. Lister, 2013: Modeling soil moisture-precipitation feedback in the Sahel: Importance of spatial scale versus convective parameterization. *Geophys. Res. Lett.*, **40 (23)**, 6213–6218.

Taylor, C. M. and R. J. Ellis, 2006: Satellite detection of soil moisture impacts on convection at the mesoscale. *Geophys. Res. Lett.*, **33 (3)**.

Taylor, C. M., A. Gounou, F. Guichard, P. P. Harris, R. J. Ellis, F. Couvreux, and M. De Kauwe, 2011: Frequency of sahelian storm initiation enhanced over mesoscale soil-moisture patterns. *Nature Geosciences*, **4**, 430–433.

Taylor, C. M., D. J. Parker, and P. P. Harris, 2007: An observational case study of mesoscale atmospheric circulations induced by soil moisture. *Geophys. Res. Lett.*, **34 (15)**.

Thurston, W., R. J. B. Fawcett, K. J. Tory, and J. D. Kepert, 2016: Simulating boundary-layer rolls with a numerical weather prediction model. *Q. J. R. Meteorol. Soc.*, **142 (694)**, 211–223.

Tiedtke, M., 1989: A comprehensive mass flux scheme for cumulus parameterization in large-scale models. *Mon. Wea. Rev.*, **117**, 1779–1800.

Trentmann, J., C. Keil, M. Salzmann, C. Barthlott, H.-S. Bauer, M. Lawrence, D. Leuenberger, H. Wernli, V. Wulfmeyer, U. Corsmeier, and C. Kottmeier, 2009: Multi-model simulations of a convective situation in low-mountain terrain in central Europe. *Meteorol. Atmos. Phys.*, **103**, 95–103.

Trier, S. B., 2003: Convective storms - convective initiation. In: Encyclopedia of atmospheric sciences, Vol 2. [Holton JR, Curry JA, Pyle JA (eds)], Academic Press, London.

Tuttle, S. and G. Salvucci, 2016: Empirical evidence of contrasting soil moisture-precipitation feedbacks across the united states. *Science*, **352**, 825–828.

Twomey, S., 1977: The influence of pollution on the shortwave albedo of clouds. *J. Atmos. Sci.*, **34 (7)**, 1149–1152.

van den Heever, S. C., G. L. Stephens, and N. B. Wood, 2011: Aerosol indirect effects on tropical convection characteristics under conditions of radiative-convective equilibrium. *J. Atmos. Sci.*, **68**, 699–718.

Van Reken, T. M., T. A. Rissman, G. C. Roberts, V. Varutbangkul, H. H. Jonsson, R. C. Flagan, and J. H. Seinfeld, 2003: Toward aerosol/cloud condensation nuclei (CCN) closure during CRYSTAL–FACE. *J. Geophys. Res.: Atmospheres*, **108 (D20)**.

Van Weverberg, K., N. P. M. van Lipzig, L. Delobbe, and D. Lauwaet, 2010: Sensitivity of quantitative precipitation forecast to soil moisture initialization and microphysics parametrization. *Q. J. R. Meteorol. Soc.*, **136 (649)**, 978–996.

Vereecken, H., J. Huisman, Y. Pachepsky, C. Montzka, J. van der Kruk, H. Bogena, L. Weihermüller, M. Herbst, G. Martinez, and J. Vanderborght, 2014: On the spatio-temporal dynamics of soil moisture at the field scale. *Journal of Hydrology*, **516**, 76 – 96, determination of soil moisture: Measurements and theoretical approaches.

Vereecken, H., J. A. Huisman, H. Bogena, J. Vanderborght, J. A. Vrugt, and J. W. Hopmans, 2008: On the value of soil moisture measurements in vadose zone hydrology: A review. *Water Resources Research*, **44 (4)**.

Vogel, B., H. Vogel, D. Bäumer, M. Bangert, K. Lundgren, R. Rinke, and T. Stanelle, 2009: The comprehensive model system cosmo-art - radiative impact of aerosol on the state of the atmosphere on the regional scale. *Atmos. Chem. Phys.*, **9 (22)**, 8661–8680.

Wapler, K., F. Harnisch, T. Pardowitz, and F. Senf, 2015: Characterisation and predictability of a strong and a weak forcing severe convective event? a multi-data approach. *Meteorol. Z.*, **24 (4)**, 393–410.

Weckwerth, T. M., J. W. Wilson, M. Hagen, T. J. Emerson, J. O. Pinto, D. L. Rife, and L. Grebe, 2011: Radar climatology of the cops region. *Q. J. R. Meteorol. Soc.*, **137 (S1)**, 31–41.

Wernli, H., M. Paulat, M. Hagen, and C. Frei, 2008: Sal-a novel quality measure for the verification of quantitative precipitation forecasts. *Monthly Weather Review*, **136 (11)**, 4470–4487.

Western, A., R. Grayson, and G. Blöschl, 2002: Scaling of soil moisture: A hydrologic perspective. *Annual Rev. of Earth and Planetary Sci.*, **30**, 149–180.

White, B., E. Gryspeerdt, P. Stier, H. Morrison, G. Thompson, and Z. Kipling, 2017: Uncertainty from the choice of microphysics scheme in convection-permitting models significantly exceeds aerosol effects. *Atmos. Chem. Phys.*, **17 (19)**, 12 145–12 175.

Wicker, L. J. and W. C. Skamarock, 2002: Time-splitting methods for elastic models using forward time schemes. *Mon. Wea. Rev.*, **130**, 2088–2097.

Winterrath, T., W. Rosenow, and E. Weigel, 2012: On the DWD quantitative precipitation analysis and nowcasting system for real-time application in the German flood risk management. *Weath. Radar and Hydrology, IAHS Publ.*, **351**.

Zhang, F. Q., A. M. Odins, and J. W. Nielsen-Gammon, 2006: Mesoscale Predictability of an Extreme Warm-Season Precipitation Event. *Wea. Forecasting*, **21**, 149–166.

D. Acknowledgements

I very much thank Prof. Dr. Corinna Hoose for her supervision and help! Corinna, you raised my interest in the beauty of cloud microphysics, you have always been there when I needed your advice and you cared about small and large concerns. Thank you for offering me the opportunity working with you and your group, I have had a great time!

I thank Prof. Dr. Christoph Kottmeier for accepting as examiner for this thesis and for asking questions and giving comments during the time of this thesis.

Dr. Christian Barthlott has accompanied me through this thesis in a very special way. Christian, thanks for your help with all kinds of questions, for you door which is always open, for the discussions we had and for sharing your endless knowledge with me.

Thank you to the cloud physics group: We had great discussions, you helped me a lot settling into the topic, I got lots of advice on my work and I appreciated listening to all of your comments and ideas. Especially I would like to thank Andrew Barrett: For your great help throughout the whole thesis, in particular your help in writing my first paper, for chatting about aerosols, finalizing everything and for reading through large parts of this thesis. I learned a lot from your feedback and you always helped and encouraged me to find my own way. Also, I thank Hassan Beydoun for bringing up new ideas, for never stopping discussing, for being creative and enthusiastic! I thank Constanze Wellmann for all the moments we shared, all the traveling we did together and for answering lots of meteorology questions.

I thank all people within SFB TR-165 "Waves to Weather". I benefited from all the exchange and meetings we had during the last years. I want to thank my B3 colleagues Florian Baur and Christian Keil from Munich, for a nice and very pleasant collaboration.

I want to thank Doris Stenschke, Friederike Schönbein and Gerhard Brückel for all help in administrative and organizational belongings. I also thank the people from the 13th floor at Campus South for always being very helpful and I also thank my office mates for making every day worth coming to work. A sportive thank you goes to all my colleagues who joined for swimming, running and exercise sessions during lunch time. I always appreciated going back to work relaxed and with a fresh mind, and sometimes even with new scientific ideas.

To friends and family: I am grateful for everything by which you helped me during the time of this thesis. You have taken breaks with me, helped me seeing this work from different perspectives and you cheered with me in moments of joy! Thank you.